Technical University of Denmark

DTU

Linear and Nonlinear Impairment Compensation in Coherent Optical Transmission with Digital Signal Processing

Porto da Silva, Edson; Zibar, Darko; Larsen, Knud J.; Tafur Monroy, Idelfonso

[Link back to DTU Orbit](#)

DTU Library
Technical Information Center of Denmark

Linear and Nonlinear Impairment Compensation in Coherent Optical Transmission with Digital Signal Processing

Ph.D. Thesis
Edson Porto da Silva

February 14th, 2017

DTU Fotonik
Department of Photonics Engineering

Preface

The work presented in this Thesis was carried out as a part of my Ph.D. project in the period February 14th, 2014 to February 14th, 2017. The work took place at DTU Fotonik (Technical University of Denmark, Department of Photonics Engineering), with a visiting stay of five months at the Institute for Communications Engineering (LNT) of the Technical University of Munich (TUM).

- Darko Zibar (main supervisor), Associate Professor, DTU Fotonik, Technical University of Denmark, Kgs. Lyngby, Denmark

- Knud J. Larsen (co-supervisor), Associate Professor, DTU Fotonik, Technical University of Denmark, Kgs. Lyngby, Denmark

- Idelfonso T. Monroy (co-supervisor), Associate Professor, DTU Fotonik, Technical University of Denmark, Kgs. Lyngby, Denmark

Abstract

Digital signal processing (DSP) has become one of the main enabling technologies for the physical layer of coherent optical communication networks. The DSP subsystems are used to implement several functionalities in the digital domain, from synchronization to channel equalization. Flexibility and effectiveness of DSP contribute to reducing costs and increase reliability of optical communications systems. The work presented in this thesis focuses on DSP subsystems for coherent optical communication systems.

In particular, the contributions presented in this thesis relate to the following topics: (I) Kerr nonlinearity compensation, (II) spectral shaping, and (III) adaptive equalization. For (I), original contributions are presented to the study of the nonlinearity compensation (NLC) with digital backpropagation (DBP). Numerical and experimental performance investigations are shown for different application scenarios. Concerning (II), it is demonstrated how optical and electrical (digital) pulse shaping can be allied to improve the spectral confinement of a particular class of optical time-division multiplexing (OTDM) signals that can be used as a building block for fast signaling single-carrier transceivers. Finally, regarding (III), original contributions to equalization in coherent optical receivers are proposed, consisting of a new approach to analyzing and design equalizers for systems where receivers or transmitters may be subject to front-end imperfections. Numerical and experimental validations are performed to evaluate the proposed methods.

In conclusion, the results presented in this thesis contribute to the state-of-the-art of DSP for coherent optical communication over single-mode fibers (SMFs). The techniques investigated have the potential to improve performance and reliability of such systems, ultimately enabling throughput and transmission reach improvements for the next generations of coherent systems.

Resumé

Digital signalbehandling (DSP) er blevet en af de centrale teknologier i det fysiske lag af kohærente optiske kommunikationsnetværk. DSP systemerne benyttes til at implementere adskillige funktionaliteter i det digitale domæne lige fra synkronisering til kanaljustering. Fleksibiliteten of effektiviteten af DSP bidrager til reduceret pris og forbedret pålidelighed i optiske kommunikationssystemer. Det arbejde der præsenteres i denne afhandling fokuserer på DSP subsystemer til kohærente optiske kommunikationssystemer.

De bidrag der præsenteres i denne afhandling er relaterede til følgende emner: (I) kompensering af Kerr ikkelinearitet, (II) formning af spektret og (III) adaptiv signaljustering. Vedrørende (I) præsenteres originale bidrag til studiet af ikkelinearitets-kompensering (NLC) ved brug af digital tilbage-propagering (DBP). Numeriske og eksperimentelle undersøgelser er vist for forskellige anvendelsesscenarier. Vedrørende (II) er det demonstreret hvorledes optiske og elektrisk (digital) pulsformning kan anvendes til at forbedre den spektral afgrænsning af bestemte klasser af optiske tids-multiplexede (OTDM) signaler, der kan benyttes som element til realisering af hurtige enkelt-carrier transceivere. Endelig vedrørende (III) er der foreslået originale bidrag til signaljustering i kohærente optiske modtagere, bestående af en ny tilgang til analysering og design af equalizere til systemer hvor modtager eller sender lider under imperfektioner på indgangs-/udganstrin. Numeriske og eksperimentelle undersøgelser bekræfter de foreslåede metoder.

De resultater der præsenteres i denne afhandling bidrager til state-of-the-art indenfor digital signalbehandling (DSP) til kohærent optisk kommunikation over standard single mode fiber (SMF). De undersøgte teknikker har potentiale til at forbedre ydeevnen og pålideligheden i disse systemer og følgelig muliggøre forbedringer af kapacitet og transmissionsdistance i næste generation af kohærente systemer.

Acknowledgments

First of all, I would like to thank my parents and family for all support they gave me over all my life. I would like to thank Darko for his guidance during the three years of this Ph.D. project. I would like to thank my friend Robert Borkowski, who was the first person encouraging me to applying for a Ph.D. position at DTU Fotonik. Thanks to Francesco Da Ros and Metodi Yankov for all I have learned and the help I got from them, and for a productive cooperation, which also includes many Friday bars.

Moreover, I would like to thank the High Speed Optical Communications (HSOC) group. It was my pleasure to be part of this really nice, diverse, and motivating work environment.

I am grateful to Prof. Gerhard Kramer and all people from the Institute for Communications Engineering of the Technical University of Munich, who kindly received me as visiting Ph.D. student during my external stay. I really enjoyed the discussions on Information Theory and the opportunity to learn new ways to approach research problems. Furthermore, the Bavarian summer time is something that I am going to miss.

Thanks to my colleges and friends from the "DSP team": Xema, Simone, Júlio, and Rasmus. Special thanks to Molly Piels, who kindly help me in clarifying many ideas during this Ph.D. project, and also for being a great trip companion.

I would like to thank all my friends in Brazil that, even with a long separating distance, were always supportive to me, and made my vacations back home better than ever.

Finally, I would like to thank my grandfather Genaro, who sadly passed away in 2016. I will be ever grateful for his assistance in many difficult

times of my life, and I am sorry that he has not lived to see me finishing this journey.

Ph.D. Publications

The following publications have resulted from this Ph.D. project.

Articles in international peer-reviewed journals: (9)

J1 (Invited) M. P. Yankov, F. Da Ros, **E. P. da Silva**, T. Fehenberger, L. Barletta, D. Zibar, L. K. Oxenløwe, M. Galili, S. Forchhammer, "Nonlinear phase noise compensation in experimental WDM systems with 256QAM", accepted for publication in *Journal of Lightwave Technology*.

J2 F. Da Ros, **E. P. da Silva**, D. Zibar, S. Chu, B. Little, R. Morandotti, M. Galili, D. Moss, L. K. Oxenløwe, "Wavelength conversion of QAM signals in a low loss CMOS compatible spiral waveguide", submitted to *APL Photonics*.

J3 **E. P. da Silva**, D. Zibar, "Widely linear equalization for IQ imbalance and skew compensation in optical coherent receivers", *Journal of Lightwave Technology*, vol.34, No. 15, pp. 3577-3586, 2016.

J4 M. P. Yankov, F. Da Ros, **E. P. da Silva**, S. Forchhammer, K. J. Larsen, L. K. Oxenløwe, M. Galili, D. Zibar, "Constellation shaping for WDM systems using 256QAM/1024QAM with probabilistic optimization", *Journal of Lightwave Technology*, vol. 34, no. 22, pp. 5146-5156, 2016.

J5 **E. P. da Silva**, R. Borkowski, S. Preussler, F. Schwartau, S. Gaiarin, M. I. Olmedo, A. Vedadi, M. Piels, M. Galili, P. Guan, S. Popov, C.-S. Brès, T. Schneider, L. Oxenløwe, D. Zibar, "Combined optical and electrical spectrum shaping for high baud rate Nyquist-WDM transceivers," *IEEE Photonics Journal*, vol. 8, no. 1., 2016.

J6   **E. P. da Silva**, K. J. Larsen, D. Zibar, "Impairment mitigation in superchannels with digital backpropagation and MLSD," *Optics Express*, vol. 23, no. 23, pp. 29493-2950, 2015.

J7   S. S. Cercós, M. Piels, J. M. Estarán, M. Usuga, **E. P. da Silva**, A. M. Fagertun, I. T. Monroy, "100 Gbps IM/DD links using quad-polarization: performance, complexity, and power dissipation," *Optics Express*, vol. 23, No. 15, pp. 19954-19968, 2015. .

J8   J. M. Estarán, M. A. Usuga, **E. P. da Silva**, M. Piels, M. I. Olmedo, D. Zibar, I. T. Monroy, "Quaternary polarization-multiplexed sub-system for high-capacity IM/DD optical data links," *Journal of Lightwave Technology*, vol. 33, no. 7, pp. 1408-1416, 2015.

J9   M. Piels, **E. P. da Silva**, J. M. Estaran, R. Borkowski, I. T. Monroy, D. Zibar, "Focusing over optical fiber using time reversal," *IEEE Photonics Technology Letters*, vol. 27, no. 6, pp. 631-634, 2015.

Contributions to international peer-reviewed conferences: (16)

C1   M. P. Yankov, **E. P. da Silva**, F. Da Ros, D. Zibar, "Experimental analysis of pilot-based equalization for probabilistically shaped WDM systems with 256QAM/1024QAM," *Proc. of the Optical Fiber Communication Conference (OFC)*, paper W2A.48, 2017.

C2   S. Gaiarin, X. Pang, O. Ozolins, R. T. Jones, **E. P. da Silva**, R. Schatz, U. Westergren, S. Popov, G. Jacobsen, D. Zibar, "High speed PAM-8 optical interconnects with digital equalization based on neural network," *Proc. of the Asia Communications and Photonics Conference (ACP)*, paper AS1C.1, 2016.

C3   **E. P. da Silva**, M. P. Yankov, F. Da Ros, S. Forchhammer, M. Galili, L. K. Oxenløwe, D. Zibar, "Experimental comparison of gains in achievable information rates from probabilistic shaping and digital backpropagation for DP-256QAM/1024QAM WDM systems," *Proc. of the European Conference on Optical Communication (ECOC)*, paper M.1.D.1, 2016.

C4   **E. P. da Silva**, D. Zibar, "Widely linear blind adaptive equalization for transmitter IQ-imbalance/skew compensation in multicarrier systems," *Proc. of the European Conference on Optical Communication (ECOC)*, paper M.1.B.5, 2016.

C5   M. P. Yankov, F. Da Ros, **E. P. da Silva**, T. Fehenberger, L. Barletta, D. Zibar, L. K. Oxenløwe, M. Galili, S. Forchhammer, "Experimental study of nonlinear phase noise and its impact on WDM systems with DP-256QAM," *Proc. of the European Conference on Optical Communication (ECOC)*, paper W.1.D.1., 2016.

C6   F. Da Ros, M. P. Yankov, **E. P. da Silva**, M. Pu, L. Ottaviano, H. Hu, E.Semenova, S. Forchhammer, D. Zibar, M. Galili, K. Yvind, L. K. Oxenløwe "Characterization of a wavelength converter for 256-QAM signals based on an AlGaAs-on-insulator nanowaveguide," *Proc. of the European Conference on Optical Communication (ECOC)*, paper W.3.C.3., 2016.

C7   H. Hu, F. Da Ros, F. Ye, M. Pu, K. Ingerslev, **E. P. da Silva**, M. Nooruzzaman, Y. Amma, Y. Sasaki, T. Mizuno, Y. Miyamoto, L. Ottaviano, E. Semenova, P. Guan, D. Zibar, M. Galili, K. Yvind, L. K. Oxenløwe, T. Morioka, "Single-source AlGaAs frequency comb transmitter for 661 Tbit/s data transmission in a 30-core fiber," *Proc. of the Conference on Lasers and Electro-Optics (CLEO)*, postdeadline paper JTh4C.1, 2016.

C8   F. Da Ros, **E. P. da Silva**, D. Zibar, S. T. Chu, B. Little, R. Morandotti, M. Galili, D. J. Moss, L. K. Oxenløwe, "Wavelength conversion of QPSK and 16-QAM coherent signals in a CMOS compatible spiral waveguide," *Proc. of the Integrated Photonics Research, Silicon, and Nanophotonics (IPR)*, paper IM3A.4, 2016.

C9   J. C. M. Diniz, **E. P. da Silva**, M. Piels, D. Zibar, "Joint IQ skew and chromatic dispersion estimation for coherent optical communication receivers," *Proc. of the Signal Processing in Photonic Communications (SPPCom)*, paper SpTu2F.2, 2016.

C10   M. Piels, **E. P. da Silva**, R. Borkowski, D. Zibar, "Performance emulation and parameter estimation for nonlinear fibre-optic links," *Proc. of the European Conference on Network and Optical Communications (NOC)* (Invited), 2016.

C11   F. Da Ros, **E. P. da Silva**, D. Zibar, S. Chu, B. little, R. Morandotti, M. Galili, D. Moss, L. Oxenløwe, "Low-penalty up to 16-QAM wavelength conversion in a low loss CMOS compatible spiral waveguide," *Proc. of the Optical Fiber Communication Conference (OFC)*, paper Tu2K. 5, 2016.

C12   **E. P. da Silva**, F. Da Ros, D. Zibar, "Performance of multi-channel

DBP with long-haul frequency-referenced transmission," *Proc. of the Optical Fiber Communication Conference (OFC)*, paper Th2A.32, 2016.

C13 **E. P. da Silva**, K. J. Larsen, D. Zibar, "Mitigation of linear and nonlinear impairments in spectrally efficient superchannels," *Proc. of the Signal Processing in Photonic Communications (SPPCom)*, paper SpS2C.3, 2015.

C14 **E. P. da Silva**, K. J. Larsen, D. Zibar, "Nonlinear compensation with modified adaptive digital dackpropagation in flexigrid networks," *Proc. of the Conference on Lasers and Electro-Optics (CLEO)*, paper SM2M, 2015.

C15 M. Piels, **E. P. da Silva**, J. M. Estaran, R. Borkowski, D. Zibar, I. T. Monroy, "DSP-based focusing over optical fiber using time reversal," *Proc. of the European Conference on Optical Communication (ECOC)*, paper P.7.8, 2014.

C16 J. M. Estaran, M. Usuga, **E. P. da Silva**, M. Piels, I. T. Monroy, "Quad-polarization transmission for high-capacity IM/DD links," *Proc. of the European Conference on Optical Communication (ECOC)*, postdeadline paper PD.4.3, 2014.

Contents

Chapter 1

Introduction

In the past few decades, information has become one of the main pillars that sustain and shape modern society and economy. From social networks, passing through video streaming services, to electronic commerce, more and more attention has been given to how information is produced, transferred and stored. Therefore, the importance of information technologies has never been so ubiquitous as it is in this era.

The development of telecommunications is one of the remarkable achievements of the human kind and direct consequence of advances in science and engineering. Nowadays, a virtual real-time communication between individuals placed on the opposite sides of the globe it is possible thanks to a vast physical network able to move information at the speed of light. The core of this infrastructure is composed of the fiber-optic networks, which assume the task of managing the gross amount of data traffic over distances up to thousands of kilometers.

In a historical perspective, the expansion of fiber-optic communication started with the invention of the first laser in 1960. That was followed by the development of the first silica fibers with low attenuation (the 1970s to the 1980s) and the first optical amplifiers (end of the 1980s), which became the core of the deployed wavelength-division multiplexing (WDM) systems operating in the present days [1]. Current single-mode fibers have minimum attenuation varying from 0.16 to 0.2 dB/km in an interval of the infrared spectrum around 1550 nm. Within this spectral window, optical amplification is possible with Erbium-doped fiber amplifier (EDFA), typically over the full C-band (1530 nm to 1565 nm). It corresponds to approximately 5 THz of bandwidth available for communication. Currently, transmission rates as high as 65 Tb/s per single-mode fiber (SMF) have been demon-

strated over transoceanic distances [2], which corresponds to an increase of 65 times compared to the systems available in the early 2000s.

Despite the enormous growth in the capabilities of fiber-optic communication technology to handling data traffic, the optical networks face several challenges posed by the ever-increasing demand for bandwidth and telecommunication services worldwide [3].

New generations of optical communication systems are expected to keep the pace in attending the service demand, while maintaining low cost and high energy efficiency [4–6]. The path towards of such stringent goals requires an number of interdisciplinary tasks to be solved. On one side, highly integrated, low power consumption optical devices are necessary. On the other side, intelligent signal processing tools are needed to optimize the use of resources available in the network. In the physical layer of the optical networks, those guidelines resulted in the significant development of coherent communications. Remarkably, the recent advances in digital signal processing (DSP), advanced modulation formats [7] and channel coding have pushed the state-of-the-art towards the limits of information transmission over standard single-mode fiber (SSMF).

The ultimate limits for reliable communication over fiber-optic channels are still unknown. So far, the complicated interplay between linear and nonlinear interactions of the electric field with the dielectric medium due to the Kerr effect [8] and its dependence on the signal power have prevented the optical fiber to be resolved in a tractable channel model for information-theoretic analysis. Nevertheless, lower bounds on the fiber capacity have been derived in the past ten years [9–12], estimating the relation between achievable information rate (AIR) and the launched power at the fiber input. Kerr nonlinear distortions are also known as nonlinear interference (NLI) [11]. The NLI manifests itself as data-dependent additive-multiplicative distortions that are a function of the physical characteristics of the fiber channel, the noise added by optical amplifiers, and the co-propagating WDM signals. One part of the NLI is the result of signal-signal nonlinear interactions and has a deterministic nature, whereas the second part, originating from signal-noise and noise-noise interactions, is stochastic.

Since the power of the NLI grows proportionally to the cubic of the signal power [10], the bounds on AIR as a function of the launch power are characterized by an inflection point, known as optimum launch power, as illustrated in Fig. 1.1. After this point, increments in input power will not result in an increase of the AIR. This behavior has become widespread
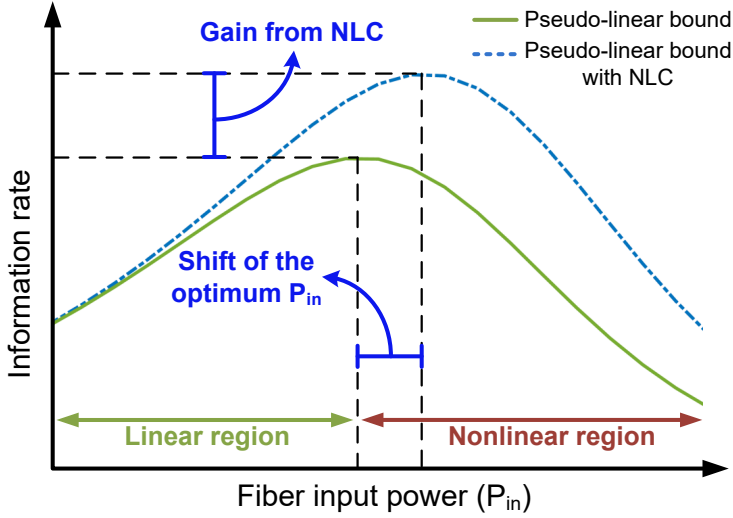
Figure 1.1 Illustration of a typical AIR lower bound for the nonlinear fiber-optic channel with and without Kerr nonlinearity compensation.

in the literature as the "nonlinear Shannon limit" of the optical fiber [13]. Since such bounds are derived based on simplified approximated physical models of the nonlinear fiber channel, their consequences always require careful interpretation [14]. However, NLI is considered the main limitation to the AIR for single-mode fiber transmission.

The AIR bounds for the fiber channel have motivated the research of nonlinearity compensation (NLC) techniques. The fractions of the NLI that are deterministic functions of on the transmitted signals, or exhibit a stochastic behavior sufficiently slow to be tracked, can be compensated with DSP. The NLC can be performed with DSP at the transmitter or the receiver. As shown in Fig. 1.1, the result of NLC is a reduction in the non-linear characteristic of the channel, allowing the transmitters to achieve higher rates by increasing the input power to a new optimum value.

Several DSP-based NLC techniques were proposed in the literature [15]. The most popular are based on nonlinear channel models for the optical fiber. In particular, digital backpropagation (DBP) based on the split-step Fourier method (SSFM) [16], perturbation [17] and Volterra [18] models for the NLI have been extensively numerically and experimentally investigated.

High computational complexity allied with limited benefits remain a challenge for practical implementation of efficient DSP-based NLC tech-

niques.

The Kerr nonlinearities can also be compensated or mitigated with the aid of nonlinear optical signal processing (OSP). In this direction, optical phase conjugation (OPC) employing the mid-link spectral inversion technique [19–22], phase-conjugated twin-waves transmission [23, 24] and phase-sensitive amplification [25] have been investigated. The broadband characteristics of nonlinear OSP-based techniques are an advantage over DSP-based ones. It allows, for example, simultaneous compensation of inter-channel NLI within several WDM channels in scenarios where the complexity of the DSP-based approaches is prohibitive, even for laboratory experiments. However, several issues make it difficult to implement OSP-based NLC in real networks, since they usually demand specific modifications or configurations for the fiber links, which are not requirements for most of the DSP-based NLC techniques.

Instead of attempting to eliminate the distortions caused by the Kerr effect, an alternative solution could be finding another domain for information multiplexing where the nonlinear nature of the fiber does not appear as an obstacle. This idea has motivated the recent studies on the nonlinear Fourier transform (NFT) [26–28]. Under some conditions, the NFT can be used to define a domain of signals whose evolution through the nonlinear fiber channel is defined by a linear operation. Put differently, the Kerr effect itself is included in the choice of the orthogonal basis for data transmission. The NFT could then be used to define a nonlinear frequency-division multiplexing (NFDM) system which, ultimately, would be the alternative to a WDM system. So far, implementations of the NFT have been shown to be challenging, due to the complexity of the DSP algorithms and modeling restrictions that do not match practical scenarios in optical networks. Nevertheless, NFT is considered as a promising field for new DSP applications in optical communications.

With all available multiplexing dimensions in SMF fibers (time, frequency, polarization) being exhaustively explored and the challenges to overcoming the Kerr effect limitations imposed to the transmission rates, the spatial-division multiplexing (SDM) has appeared as a technological option to keep increasing the throughput rates in optical networks [29–33]. In the last decade, the developments in multimode and multicore fibers followed by SDM optical amplifiers and switching devices have paved the path for the latest records in optical transmission experiments [34]. Systems based on SDM are soon expected to become the next frontier of optical communications technology.

1.1   Motivation and outline of contributions

A considerable share of the coherent optical communication progress can be attributed to the development of DSP subsystems. Because essential functionalities, such as time synchronization and channel equalization, are efficiently performed with DSP, its importance is expanding to several kinds of optical transmission systems.

The primary focus of the work presented in this thesis is on DSP subsystems for coherent optical communication systems. In particular, the contributions presented relate to the following topics.

Kerr nonlinearity compensation

Chapters 3, 4 and 5 present original contributions to the study of numerical and experimental performances of NLC with digital backpropagation (DBP). Each chapter addresses a different scenario of DBP application.

Spectral shaping

The contributions of Chapter 6 are related to the spectral shaping of high baud rate single-carrier transceivers based on optical time-division multiplexing (OTDM). Particularly, it is demonstrated how optical and electrical (DSP-based) pulse shaping can be allied to improve the spectral confinement of Nyquist-OTDM signals.

Adaptive equalization

Original contributions to equalization in coherent optical receivers are summarized in chapters 7 and 8. There, a new approach to analyzing and design equalizers for systems where receivers or transmitters subject to front-end imperfections is proposed, with subsequent numerical and experimental validation.

1.2   Organization of the thesis

This thesis interpolates material from three journal papers ([J6], [J3], and [J5]) and four conference papers ([C3], [C4], [C12], and [C13]) published by the author within the duration of the Ph.D. project.

Since the main subjects of different chapters may not necessarily overlap, the state-of-the-art review is distributed within the introduction of each chapter for better contextualization of the contributions.

The chapters containing the contributions from this Ph.D. project are divided into three parts. Part I is composed by chapters 3, 4 and 5, with main subjects related to Kerr nonlinearity compensation. Part II has only Chapter 6, whose content relates to spectral shaping. Finally, Chapter 7 and Chapter 8 compose Part III, where adaptive equalization is the principal subject.

The organization of the chapters is detailed as follows.

In Chapter 2, fundamentals in digital communications and coherent optical communication systems are briefly reviewed with a focus on the most important concepts that will be touched upon in the discussions after that.

In Chapter 3, a numerical analysis of the performance gains provided by DBP and maximum likelihood sequence detection (MLSD) in superchannels when the carriers are generated by different spectral shaping techniques. The simulations assumed transmission over uncompensated dispersion links.

Chapters 4 and 5 present two experimental investigations regarding NLC with DBP. In Chapter 4, the impact of a frequency-referenced source on the performance of dual polarization multicarrier digital backpropagation (MC-DBP) performed at the receiver-side is experimentally investigated for up to 4000 km of transmission. In Chapter 5, a study carried out to establish a comparison between gains in AIR obtained by using probabilistic optimization of high-order quadrature amplitude modulation (QAM) formats and by performing NLC with DBP, in WDM transmissions up to 1700 km of reach.

In Chapter 6, the problem of how to approach the Nyquist's bandwidth limits for the power spectrum density (PSD) of OTDM signals generated by periodic trains of optical sinc pulses is considered. The benefits of the proposed combination of optical and electrical (digital) pulse shaping are discussed in the light of analytical results. A further experimental study is carried out to evaluate the feasibility of the proposed solution.

In Chapter 7 and Chapter 8, the use of widely linear complex-valued transformations is proposed to model in-phase/quadrature (IQ) defects in coherent optical transceivers. The connection between IQ-mixing and channel equalization is analyzed and adaptive equalization structures to compensate for such effects are proposed and validated by numerical simulations and experiments. Chapter 7 presents a detailed analysis of the consequences

of IQ-mixing happening at a single-carrier receiver, whereas Chapter 8 focuses on IQ-mixing happening in a multicarrier transmitter.

Chapter 2

Fundamentals of coherent optical communication

In this chapter, a very brief introduction to the fundamentals of coherent optical systems is presented. The concepts highlighted here are connected to the main topics that the reader will find in the following chapters of this thesis. Detailed discussion on the subject can be consulted in the references [8, 9, 35, 36].

The remaining of the chapter is organized as follows. In Section 2.1 a canonical description of a coherent optical communication system is given. Section 2.2 presents relevant concepts related to transmitters. In Section 2.3, the fiber-optic channel model is shown, and its properties are discussed. Finally, Section 2.4 details the optical front-end and digital signal processing (DSP) functions present in conventional coherent optical receivers.

2.1 Coherent optical systems

In contrast with the traditional intensity modulated direct detection (IM/DD) systems, coherent systems use not only the amplitude but also the carrier frequency and phase to encode information at the transmitter side. In such systems, to decide which signals were transmitted, the receiver must be able to access the frequency and the phase of the transmitted carrier synchronously. For that propose, the use of a local oscillator and a coherent front-end is required.

A block diagram of a simplified optical coherent transmission system is depicted in Fig. 2.1. The blocks on the left side of Fig. 2.1 are related
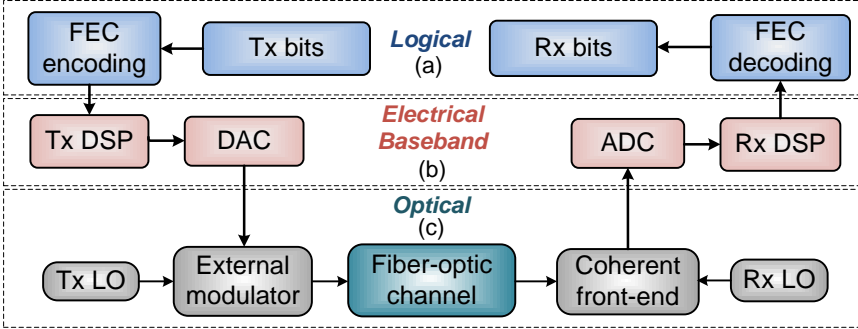
Figure 2.1 Block diagram of a typical coherent optical communication system. (a) Logical level, FEC encoding and decoding. (b) Baseband signal level, DAC, ADC and DSP blocks for synchronization and equalization. (c) Optical signal level.

to the transmitter structure, whereas the blocks on the right side detail the receiver. In Fig. 2.1(a), the logical level of the system is shown where the forward error correction (FEC) functions are implemented, and the information is purely binary. In Fig. 2.1(b), the baseband signal level is shown. This level groups the DSP and digital-to-analog converter (DAC) at the transmitter side, and the analog-to-digital converter (ADC) and DSP at the receiver. The last level is the optical level, composed by the optical modulator at the transmitter and the coherent front-end at the receiver, each with the respective local oscillator (LO), and finally the fiber-optic channel.

There are two main advantages of coherent detection over IM/DD systems. Firstly, coherent detection enables one to explore all available orthogonal dimensions to encode, multiplex and transmit data over the optical fiber, allowing the use of sophisticated modulation and coding schemes to increase the rates or the reliability of the transmission. Secondly, the full knowledge of the electrical field obtained after coherent detection allows the receiver to efficiently compensate for a number of channel impairments by applying DSP techniques. Both advantages translate in improvements of transmission reach or system throughput.

2.2   Transmitters

In a coherent optical communication system, the transmitter is responsible for encoding the information bits, performing the mapping of bits to sym-

bols of a given modulation format and modulate the optical carrier which will be transmitted through the fiber channel.

The following definitions are relevant in the discussions to appear in the remaining chapters of this thesis.

2.2.1 Modulation formats

Modulation format is finite set S of symbols (complex numbers). Here, $S = \{s_m\}_{m=1}^M$, with $M = 2^b$, where b is the number of bits mapped to each symbol of S.

In this thesis, only linear memoryless modulation formats are addressed [35]. In particular, M-ary quadrature amplitude modulation (QAM) and quadrature phase-shift keying (QPSK). Except in Chapter 5, all modulation formats considered have a uniform probability distribution over the set of symbols.

2.2.2 Baseband signals

Let $g(t)$ be a complex-valued baseband signal, it can be represented by

$$g(t) = \sum_{k=-\infty}^{\infty} s_k p(t - kT_s), \tag{2.1}$$

where s_k is the symbol transmitted at the instant $t = kT_s$, $p(t)$ is the pulse shape and T_s is the symbol period. Unless stated otherwise, the elements in the sequence of symbols $(s_k)_{k=-\infty}^{\infty}$ are assumed to be independent and identically distributed (i.i.d.).

Due to the random nature of the sequence of transmitted symbols, $g(t)$ also expresses a realization of a cyclostationary stochastic process with period T_s [35].

2.2.3 Power spectrum density of linearly modulated signals

Let $g(t)$ be a complex-valued baseband signal, its autocorrelation function $R_{gg}(\tau)$ can be defined as

$$R_{gg}(\tau) = \frac{1}{T_s} \sum_{n=-\infty}^{\infty} R_{ss}(n) R_{pp}(\tau - nT_s), \tag{2.2}$$

where $R_{ss}(n) = (1/2)E[s_k^* s_{k+n}]$ is the autocorrelation function of the symbol sequence (assumed to be a stationary process), $E[.]$ denotes expected

value, and $R_{pp}(\tau) = \int_{-\infty}^{\infty} p^*(t)p(t+\tau)dt$ is the time autocorrelation function of the pulse shape [35].

By taking the Fourier transform of $R_{gg}(\tau)$, the average power spectrum density (PSD) of $g(t)$ is obtained as

$$G(f) = \frac{1}{T_s}|P(f)|^2 S(f), \tag{2.3}$$

where

$$P(f) = \int_{-\infty}^{\infty} p(t)e^{-j2\pi ft}dt, \tag{2.4}$$

and

$$S(f) = \sum_{n=-\infty}^{\infty} R_{ss}(n)e^{-j2\pi fnT_s}. \tag{2.5}$$

Notice that, if the i.i.d. sequence of symbols has zero mean and it is uncorrelated, $R_{ss}(n)$ is a delta function centered at $n = 0$, so that $S(f)$ is a constant over the interval $[-1/2T_s, 1/2T_s]$. Therefore, under these conditions, the shape of the spectrum in Eq. (2.3) will only depend on pulse shape of the baseband signal.

2.2.4 Spectral efficiency

The spectral efficiency (SE) is a figure of merit used to evaluate how efficiently the information is been transferred through a given bandwidth of the channel. The SE is defined as

$$SE = \frac{bR_s}{B}, \tag{2.6}$$

where R_s is the transmission symbol rate (baud rate), b is the number of *information* bits per symbol and B is the bandwidth utilized in Hz.

In the literature of optical communications, the SE is usually defined for a given wavelength-division multiplexing (WDM) system. In this case, the calculation in Eq. (2.6) has B as the spacing of the WDM frequency grid, and R_b corresponds to the information rate per WDM channel.

Hence, the SE depends on how close in frequency the WDM channels can be placed, which directly relates to how much spectrum their PSDs occupy. In the Nyquist limit for intersymbol interference (ISI) free transmission, $R_s = B$ [35]. For real WDM systems, $R_s < B$, since guard bands are necessary to avoid interference between neighbor channels. It is still possible to have $R_s \geq B$, if the receiver can tolerate ISI and inter-channel interference.

2.2.5   External optical modulators

Optical modulation is the process of varying one or more properties of an optical carrier as a function of a modulating baseband electrical signal containing information to be transmitted. In coherent optical transmitters, external optical in-phase/quadrature (IQ) modulators are the components responsible for performing optical modulation.

Optical modulators can be fabricated by creating optical waveguide in an electro-optical substrate. Due to its fast linear electro-optic response characteristics, Lithium niobate (LiNbO$_3$) is the most common material used as substrate for optical modulators in coherent WDM systems.
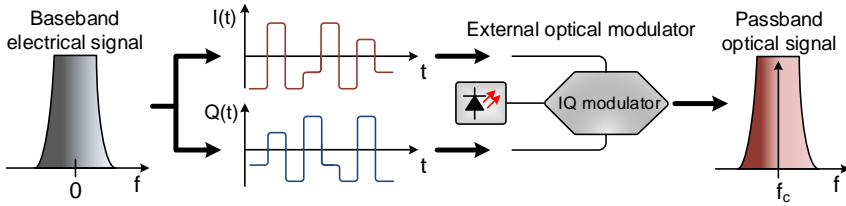
Figure 2.2 Schematic of optical IQ modulation.

External optical IQ modulators are built with combinations of basic external optical modulator structures, such as the phase modulator and the Mach-Zehnder modulator (MZM) [36]. The modulation bandwidth, carrier extinction ratio, and the linearity are the most important properties to characterize the performance of optical IQ modulators.

High-order modulation formats require external modulation with a linear response, such that the relative distance between constellation symbols in the baseband signal is maintained in the optical domain. Since MZMs have a nonlinear (sinusoidal) response characteristic, in practice, linear operation is achieved by restricting the driving signals to a linear interval of the MZMs response, or by using nonlinear pre-distortion as a linearization method.

All the external optical IQ modulators used in the experiments reported in this thesis were Lithium niobate-type modulators.

2.2.6   Superchannels

The bandwidth limitation of components, such as DACs and optical modulators, brings challenges to build single-carrier transmitters with high SE

over typical WDM channel bandwidths. As an alternative, parallel lower bandwidth transmitters can be arranged such that the total rate over the WDM channel bandwidth is divided among multiple modulated carriers. A set of closely packed carriers that travel from the same origin to the same destination in a WDM system is the definition of a superchannel. An example of a superchannel spectrum is shown in Fig. 2.3.
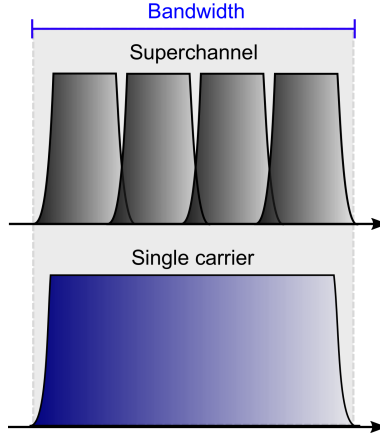
Figure 2.3 Example of a superchannel PSD compared with a single-carrier PSD occupying the same bandwidth.

2.3 The fiber-optic channel

The single-mode fiber (SMF) is a dielectric cylindrical waveguide, made out of silica (SiO$_2$) glass, whose guiding properties are based on the total internal reflection principle. Propagation of light inside an SMF is subjected to linear and nonlinear effects that have to be considered together to define an accurate fiber channel model.

The slow-varying complex-valued envelope of an optical carrier propagating in an SMF is represented by the Jones vector of the electrical field $\mathbf{E}(z,t) = [E_x, E_y]^T$, where the indexes (x,y) refer to two orthogonal polarization modes. Its evolution through the fiber is well known to be described by the coupled nonlinear Schrödinger equation (NLSE) [8]

$$\frac{\partial \mathbf{E}}{\partial z} + \frac{\boldsymbol{\alpha}}{2}\mathbf{E} + \boldsymbol{\beta_1}\frac{\partial \mathbf{E}}{\partial t} + j\frac{\boldsymbol{\beta_2}}{2}\frac{\partial^2 \mathbf{E}}{\partial t^2} = j\boldsymbol{\gamma}\left[|\mathbf{E}|^2\boldsymbol{\sigma_0} - \frac{1}{3}(\mathbf{E}^H\boldsymbol{\sigma_2}\mathbf{E})\boldsymbol{\sigma_2}\right]\mathbf{E}, \quad (2.7)$$

where the matrices $\boldsymbol{\alpha}$, $\boldsymbol{\beta_n}$, $\boldsymbol{\gamma}$ describing the fiber parameters for attenuation, chromatic dispersion and Kerr nonlinearity, respectively, are given by

$$
\boldsymbol{\alpha} = \begin{bmatrix} \alpha_x & 0 \\ 0 & \alpha_y \end{bmatrix}, \boldsymbol{\beta_n} = \begin{bmatrix} \beta_{nx} & 0 \\ 0 & \beta_{ny} \end{bmatrix}, \boldsymbol{\gamma} = \begin{bmatrix} \gamma_x & 0 \\ 0 & \gamma_y \end{bmatrix},
$$

and $\boldsymbol{\sigma_2}$ is one of the Pauli spin matrices[1]

$$
\boldsymbol{\sigma_0} = \begin{bmatrix} 1 & 0 \\ 0 & 1 \end{bmatrix}, \boldsymbol{\sigma_1} = \begin{bmatrix} 0 & 1 \\ 1 & 0 \end{bmatrix}, \boldsymbol{\sigma_2} = \begin{bmatrix} 0 & -j \\ j & 0 \end{bmatrix}, \boldsymbol{\sigma_3} = \begin{bmatrix} 1 & 0 \\ 0 & -1 \end{bmatrix}.
$$

The indexes (x, y) refer to the two orthogonal polarization modes. One should emphasize that Eq. (2.7) does not include all linear and nonlinear phenomena happening within the fiber, but it includes those that are more important from the system perspective. In this thesis, only SMF systems are addressed.

For most of the practical cases, the attenuation, second order dispersion and nonlinear coefficients are the same for both polarizations, i.e., $\alpha_x = \alpha_y = \alpha$, $\beta_{2x} = \beta_{2y} = \beta_2$, and $\gamma_x = \gamma_y = \gamma$, respectively. Moreover, if only the combination of those effects is object of analysis, Eq. (2.7) can be further simplified to the following pair of coupled scalar NLSEs

$$
\frac{\partial E_x}{\partial z} + \frac{\alpha}{2} E_x + j \frac{\beta_2}{2} \frac{\partial^2 E_x}{\partial t^2} = j\gamma \left(|E_x|^2 + \frac{2}{3} |E_y|^2 \right) E_x, \tag{2.8}
$$

$$
\frac{\partial E_y}{\partial z} + \frac{\alpha}{2} E_y + j \frac{\beta_2}{2} \frac{\partial^2 E_y}{\partial t^2} = j\gamma \left(|E_y|^2 + \frac{2}{3} |E_x|^2 \right) E_y. \tag{2.9}
$$

The last variable to be considered is the amplified spontaneous emission (ASE) noise originated in the optical amplification stages. The ASE and the nonlinear interference (NLI) are the dominant noise sources in the coherent WDM systems.

The following subsections will present short descriptions of each effect modeled in Eq. (2.7) and the amplification noise.

2.3.1 Attenuation

An optical pulse guided through an optical fiber is attenuated. Such power losses have many causes but are dominated by material absorption and

---

[1]The convention used in the notation of the Pauli spin matrices vary in the literature. Here the notation used in [40] is assumed.

Rayleigh scattering [8]. The linear effect of power loss is included in equations (2.8) and (2.9) by the loss coefficient α.

Let $P(z)$ be the signal power at the propagation distance z, then

$$P(L) = P(0)\exp(-\alpha L). \qquad (2.10)$$

The loss coefficient is usually given in dB/km, where $\alpha_{dB/km} = 4.343\alpha$. A standard single-mode fiber (SSMF) has an average attenuation coefficient of $0.2\ dB/km$ over the C-band frequency spectrum.

The losses in WDM systems are compensated with optical amplifiers placed at the end of each fiber span, whose length vary depending on the network. An example of a span configuration with SMF and Erbium-doped fiber amplifier (EDFA) is illustrated in Fig. 2.4.
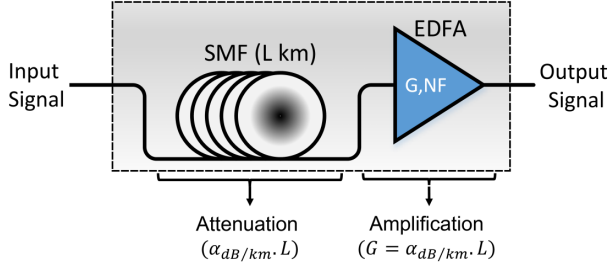
Figure 2.4 Illustration of an fiber span with an optical amplifier.

The stimulated Raman scattering can also be used to transfer energy from a pump laser to WDM signals, providing distributed amplification along the fiber span [8].

In the experimental studies presented in this thesis, both EDFA and distributed Raman amplification were considered.

2.3.2 Amplification noise

Optical amplifiers are sources of additive noise. During the amplification process, ASE is added to the optical signal such that the optical signal-to-noise ratio (OSNR) of the amplified signal is degraded with respect to the to the OSNR of the input signal. The ASE is modeled as additive white Gaussian noise (AWGN) with PSD N_{ASE} [9], and the OSNR is defined by

$$OSNR = \frac{P_{sig}}{2B_{ref}N_{ASE}} = \frac{P_{sig}}{\sigma_{ASE}^2}, \qquad (2.11)$$

where P_{sig} is the average signal power over the two state of polarization (SOP) and B_{ref} is an arbitrary reference bandwidth, usually chosen to be 12.5 GHz (0.1 nm).

Typical noise figure (NF) values for an EDFA are in the range of 4 to 6 dB, whereas distributed Raman amplifiers may achieve remarkably lower values [37].

2.3.3   Chromatic dispersion

Distinct frequency components of a signal traveling through the fiber will experience different group velocities due to the linear effect known as chromatic dispersion (CD), also referred to in the literature as group-velocity dispersion (GVD) or simply as "dispersion". The CD induces a relative delay among frequency components of a pulse propagating into the fiber, causing it to spread in time. By solving analytically the NLSE with only the GVD term, one will find that CD is accurately modeled as an all-pass linear filter whose frequency response is given by

$$H_{cd}(\omega, z) = \exp\left(-j\frac{\beta_2}{2}\omega^2 z\right),\tag{2.12}$$

where ω is the angular frequency, $\beta_2 = \beta_2(\omega_c)$ is the GVD parameter at the carrier angular frequency ω_c, and z is the propagated distance. Note that Eq. (2.12) includes only the second-order dispersion parameter β_2, which describes the dominant effect. High order dispersion terms can also be considered but are not relevant for the scenarios investigated in this thesis.

For telecom fibers, the dispersion parameter D at a given wavelength is often specified instead of β_2. The relation between both is given by

$$D = -\frac{2\pi c}{\lambda^2}\beta_2,\tag{2.13}$$

where c is the speed of light in vacuum and λ is the wavelength. The parameter D is usually given in $ps/(km \cdot nm)$.

In optical communication systems, the temporal broadening of the pulses caused by CD translates in ISI, which will degrade the system performance if not compensated.

Regarding CD management, fiber links are divided into the following two categories. The dispersion compensated (managed) links, where the CD is compensated inline with dispersion compensating fiber (DCF) modules, and dispersion uncompensated links where the CD compensation task is performed at the receiver side.

In coherent optical systems operating over dispersion uncompensated links, the accumulated CD is let to be compensated with DSP.

2.3.4 Polarization mode dispersion

An ideal SMF with perfect cylindrical symmetry over its full length will support two degenerated orthogonal polarization modes, i.e., both modes will have equal refractive indices ($n_x = n_y$). In real fibers, however, small imperfections during the production process or variations of the core shape due to bending or other external agents will result in a break of the waveguide symmetry, causing the appearance of modal birefringence.

Birefringence is characterized by a difference between the refractive indices of the polarization modes ($n_x > n_y$, or $n_x < n_y$). As a consequence, polarized light will propagate at different speeds, when aligned to different polarization axes. The degree of modal birefringence (B_m) is defined as

$$B_m = |n_x - n_y| = \Delta n, \tag{2.14}$$

which results in a difference of the propagation constants of the two polarization modes $\Delta\beta = |\beta_x - \beta_y| = (\omega/c)\Delta n$.

A fiber with constant modal birefringence has two principal axes along which the state of linear polarization of the incident light is maintained during propagation. These orientations are named slow and fast axes based on the traveling speed of light polarized along them inside the fiber. When a low-power continuous wave (CW) beam is launched with its polarization direction not oriented with neither the slow or fast axes, the SOP of the light will change along the fiber in a periodic fashion. The distance of one revolution period of the SOP is known as beat length (L_B) and defined as $L_B = 2\pi/\Delta\beta$.

A direct consequence of birefringence is that light components propagating in each polarization mode will experience distinct group delays. The relative difference in modal group delay ($\Delta\tau$) is known as differential group delay (DGD), defined as

$$\Delta\tau = |\beta_{1x} - \beta_{1y}|L, \tag{2.15}$$

where L is the propagation length.

Moreover, B_m and the orientation of x and y axes tends to shift randomly over considerably short length scales ($10 - 100\ m$) when compared to the average reach of the transmission in optical communication systems. Since for a given link these conditions vary in time, $\Delta\tau$ shows a stochastic

behavior. The expected value of the DGD ($E[\Delta\tau]$) is known as the first order polarization mode dispersion (PMD). If the DGD does not have a flat frequency response over the bandwidth of interest, higher-order PMD terms have to be considered to capture the dynamic evolution of the polarization.

The statistical modeling of PMD can be quite complicated and is out of the scope of this thesis. However, the average effect of modal birefringence can be included in the nonlinear fiber model by using the Manakov equation [38–40], which corresponds to Eq. (2.7) with its right-hand side replaced by $j(8/9)\gamma|\mathbf{E}|^2\mathbf{E}$. Applying the same assumptions used to obtain Eq. (2.8) and (2.9), the result is the following pair of coupled equations

$$\frac{\partial E_x}{\partial z} + \frac{\alpha}{2}E_x + j\frac{\beta_2}{2}\frac{\partial^2 E_x}{\partial t^2} = j\frac{8\gamma}{9}(|E_x|^2 + |E_y|^2)E_x, \qquad (2.16)$$

$$\frac{\partial E_y}{\partial z} + \frac{\alpha}{2}E_y + j\frac{\beta_2}{2}\frac{\partial^2 E_y}{\partial t^2} = j\frac{8\gamma}{9}(|E_y|^2 + |E_x|^2)E_y. \qquad (2.17)$$

Note that Eq. (2.16) and (2.17) model the *average effect* of birefringence in the Kerr nonlinearity, but they do not model PMD.

The time-varying effects of PMD are sources of ISI, hence impacting the performance of optical communication systems.

2.3.5 Kerr nonlinearities

Within silica fibers, as in any other dielectric medium, the presence of an electric field will induce a displacement of the electric charges within the material, creating a dielectric polarization field. The induced field will have an orientation such that the equivalent field within the dielectric is reduced.

Therefore, the interaction between the electrical field and dielectric will produce a modulation of the equivalent field within the medium. Such modulation is a nonlinear function of the input field. This phenomenon is the cause of the Kerr effect [41], which is present in silica fibers and responsible for the NLI in optical communication systems [9, 11].

The Kerr effect can be just understood as a change in the refractive index of the material proportional to the square of the incident electrical field.

In the NLSE propagation models, the Kerr nonlinearities are included by the terms proportional to the fiber nonlinear parameter γ, defined as

$$\gamma = \frac{n_2\omega_c}{cA_{eff}}, \qquad (2.18)$$

where n_2 is the fiber nonlinear refractive index [8], $\omega_c = 2\pi f_c$ is the angular frequency of the optical carrier, A_{eff} is the fiber effective area and c is the speed of light in vacuum. The parameter γ is usually specified in $1/(W.km)$.

In the absence of loss and dispersion effects, the Manakov system in Eq. (2.16) and (2.17) will have the following exact solution

$$\mathbf{E}(L,t) = \mathbf{E}(0,t)e^{j\phi_{nl}(L,t)}, \tag{2.19}$$

where $\phi_{nl}(L,t)$ is the integrated nonlinear phase over the propagation length $[0, L]$, defined by

$$\phi_{nl}(L,t) = \frac{8\gamma}{9} \int_0^L P(z,t)dz, \tag{2.20}$$

where $P(z,t) = |\mathbf{E}(z,t)|^2$ is the instantaneous power of the electrical field as a function of the distance z. Hence, the Kerr effect results in a power-dependent nonlinear phase modulation of the electrical field.

In the presence of dispersion and nonlinear effects, exact solutions for the NLSE are unknown, in general. Numerical solutions can be obtained with the split-step Fourier method (SSFM), which will be discussed later.

Since WDM systems have multiple modulated optical carriers simultaneously propagating within the fiber, the NLI caused by the combination of the Kerr effect and the CD will be a function of all co-propagating carriers. As mentioned in the introductory chapter, the nonlinear characteristic of the fiber channel is currently the principal limitation of the transmission rates over SMF.

In coherent optical WDM systems transmitting over long, uncompensated CD links, the accumulation of the NLI can be modeled as an additional source of AWGN at the receiver [13, 42, 43]. In this case, the effective signal-to-noise ratio (SNR) perceived by the received is given by

$$SNR_{RX} = \frac{P_{sig}}{\sigma_{ASE}^2 + \sigma_{NLI}^2}, \tag{2.21}$$

where σ_{ASE}^2 and $\sigma_{NLI}^2 \propto P_{sig}^3$ are the AWGN power contributions from the ASE and the NLI, respectively, and P_{sig} is the signal power. The Kerr effect establishes a cubic relation between the signal power and the power of the NLI, i.e, $\sigma_{NLI}^2 \propto P_{sig}^3$.

In Fig. 2.5, the signal interactions that sum up producing the NLI are classified according to its deterministic or stochastic characteristics. Distortions generated by the nonlinear coupling of signal frequency components inside the bandwidth of a WDM channel are known as intrachannel
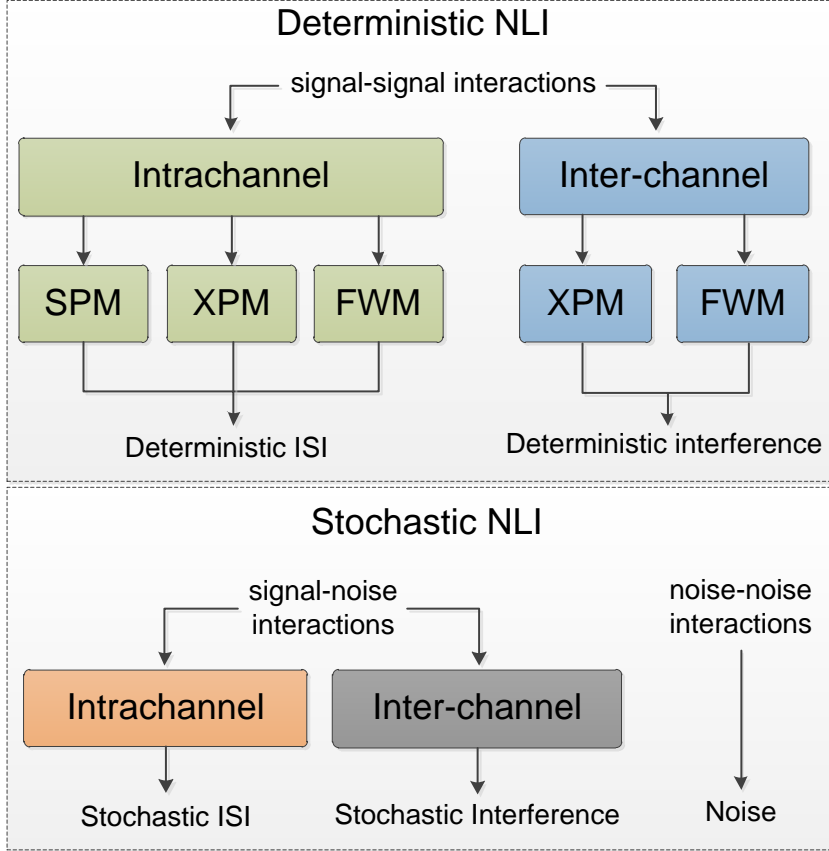
Figure 2.5 Qualitative classification of the NLI in WDM systems according to origin, deterministic/stochastic characteristics and equivalent effect from the receiver point of view.

nonlinear effects. They comprise self-phase modulation (SPM), cross-phase modulation (XPM) and four-wave mixing (FWM) [8]. If frequency components interacting are from different WDM channels inter-channel nonlinear effects take place (XPM, FWM).

Signal-signal interactions are deterministic, i.e., given full knowledge of the channel and interacting signals, there is no fundamental uncertainty in determining the NLI. This property is the basis for derivation of most

of the DSP-based nonlinearity compensation (NLC) techniques. However, in practice, there may be uncertainty in the parameters describing the channel (e.g. due to PMD), and transmitters/receivers usually have access to a limited bandwidth within the full WDM spectrum. Therefore, practical constraints also impose a degree of randomness to the NLI produced by signal-signal interactions.

On the other hand, the distortions created when the nonlinear interactions include noise are naturally stochastic. Nonlinear phase noise is the typical example of stochastic NLI caused by signal-noise interactions. The compensation of such effects in coherent receivers will then depend on the statistical properties of the stochastic processes associated with them [J1], especially how fast they change over time.

2.4   Coherent optical receivers

In this section, a succinct description of a dual polarization (DP) coherent optical receiver is given, followed by a description of the basic DSP blocks required for most of the application scenarios.

2.4.1   Coherent optical front-end

Since the frequency locking of lasers at transmitters and receivers is a difficult task in typical optical networks, coherent optical receivers are designed to perform intradyne detection [44]. This detection scheme allows the local oscillators at transmitters and receivers to being mismatched (i.e., unlocked in frequency/phase) by a small, but arbitrary, relative shift. The coherence of the transmission is completed in with carrier phase recovery in DSP.

A schematic of a standard coherent optical front-end with polarization diversity is shown in Fig. 2.6. After passing through polarization beam-splitters, the optical carrier, and the local oscillator are directed to two optical 90° hybrids, whose outputs are connected to balanced photo-detectors. This scheme allows downconversion of the signal to baseband and separation of the IQ components of each polarization.

For the x-polarization the sequence of operations performed at the front-end is described by the following equations (2.22) and (2.23). Equa-
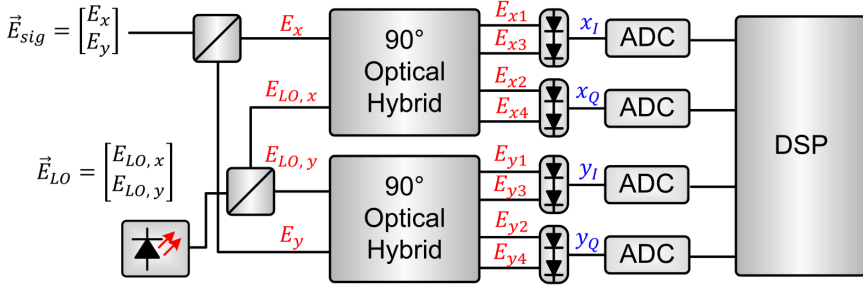
Figure 2.6 Schematic of a standard coherent optical front-end.

tion (2.22) describes the input-output relation of the 90° optical hybrid

$$
\begin{bmatrix} E_{x1} \\ E_{x2} \\ E_{x3} \\ E_{x4} \end{bmatrix} = \frac{1}{2} \begin{bmatrix} 1 & 1 \\ 1 & j \\ 1 & -1 \\ 1 & -j \end{bmatrix} \begin{bmatrix} E_x \\ E_{LO,x} \end{bmatrix}, \tag{2.22}
$$

where E_x and $E_{LO,x}$ are the complex envelopes of the signal and local oscillator, respectively. Note that in each output the phase of the LO component is rotated by a multiple of 90°.

Using the balanced photodetectors to detect pairs of the outputs whose phase difference between the LO components is 180°, we have

$$
\begin{bmatrix} x_I \\ x_Q \end{bmatrix} \propto \begin{bmatrix} |E_{x1}|^2 - |E_{x3}|^2 \\ |E_{x2}|^2 - |E_{x4}|^2 \end{bmatrix} = \begin{bmatrix} Re\left\{E_x E_{LO,x}^*\right\} \\ Im\left\{E_x E_{LO,x}^*\right\} \end{bmatrix}, \tag{2.23}
$$

where the linear relation between the balanced photocurrents (x_I, x_Q) and the IQ components of the downconverted signal is detailed. The same expressions are valid for *y*-polarization only by replacing the corresponding indexes.

The baseband signal at the output of the photodetectors is then sampled and converted to the digital domain by a bank of ADCs.

2.4.2 Digital signal processing

After analog-to-digital conversion, coherent optical receivers have to perform a sequence of DSP tasks in the attempt to finally recover the transmitted symbols, as shown in Fig. 2.7.
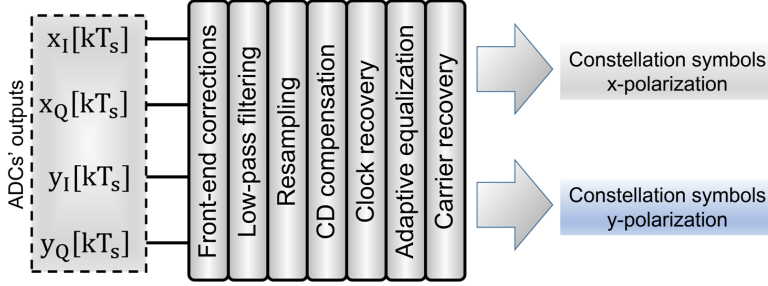
Figure 2.7 Schematic of a standard flow of DSP functions in an coherent optical receiver.

The tasks assigned to DSP can be divided into three sets: synchronization, channel equalization, and carrier phase recovery.

Synchronization

Because there is no direct synchronization between transmitters and receivers, the transmission clock has to be recovered from the detected signal at the coherent receiver. Usually, the ADCs' sampling rates are enough to provide the DSP blocks with a discrete version of the detected signal sampled at 2 samples/symbol. Clock recovery is then implemented by re-interpolating the signal according to a time basis provided by some timing error detection algorithm, such as Gardner's algorithm [45] and its variants.

For the simulation studies presented in this thesis, synchronization algorithms were not necessary, whereas, for the experimental investigations, resampling and interpolation were applied with Gardner's algorithm to adjust the signal samples coming from the ADCs for the correct sampling instants.

Channel equalization

Optical coherent receivers require channel equalization to counteract the ISI that results from the linear fiber effects, such as CD and PMD, and from the frequency responses of the electric and optical devices building transmitters and receivers. The ISI that has a time-invariant source, such as CD, is commonly compensated by static equalizers, whereas time-varying ISI, e.g. due to SOP rotation and PMD, is let to be handled by an adaptive equalizer.

The basic DSP chain of a coherent optical receiver will have a static zero-forcing CD equalizer and an adaptive equalizer in sequence. Usually, both equalizers process the signals at two samples/symbol. Moreover, the adaptive equalizer is the block responsible for demultiplexing the polarizations and approximating the matched filter response of the transmitter, if needed.

Linear equalization in coherent optical receivers will be discussed in Chapter 7 and Chapter 8.

When linear and nonlinear effects are considered, the definition of channel equalization for the fiber channel can be extended by the concept of digital backpropagation (DBP).

Digital backpropagation

The NLSE in Eq. (2.7) can be rewritten in the following form

$$\frac{\partial \mathbf{E}}{\partial z} = (\hat{\mathbf{D}} + \hat{\mathbf{N}})\mathbf{E}, \tag{2.24}$$

where $[\hat{\mathbf{D}}, \hat{\mathbf{N}}]$ is a pair of linear and a nonlinear operators respectively, given by

$$\hat{\mathbf{D}} = \left[-\frac{\boldsymbol{\alpha}}{2} - \boldsymbol{\beta_1}\frac{\partial}{\partial t} - j\frac{\boldsymbol{\beta_2}}{2}\frac{\partial^2}{\partial t^2} \right] \mathbf{E}, \tag{2.25}$$

$$\hat{\mathbf{N}} = j\boldsymbol{\gamma} \left[|\mathbf{E}|^2 \boldsymbol{\sigma_0} - \frac{1}{3}(\mathbf{E}^H \boldsymbol{\sigma_2}\mathbf{E})\boldsymbol{\sigma_2} \right] \mathbf{E}. \tag{2.26}$$

One way to solve Eq. (2.24) numerically is by assuming that, for small discrete steps of the spatial coordinate (Δz), the complex envelope of the optical carrier has an evolution slow enough such that the actions of linear and nonlinear operators can be considered as independent. Under this condition, the full evolution of the field can be approximated by a concatenation of linear and nonlinear steps, where each step is the solution of Eq. (2.24) for the corresponding operator. The numerical algorithm based on this strategy is the well known split-step Fourier method (SSFM) [8].

The SSFM is an accurate tool to simulate the propagation of WDM signals through the optical fiber [47,48]. In the SSFM, the action of $\hat{\mathbf{D}}$ is resolved in the frequency domain, whereas the action of $\hat{\mathbf{N}}$ results in a nonlinear phase shift in the time domain. Therefore, the method relies upon the application of the discrete Fourier transform to alternate the domains where linear and nonlinear steps are performed.
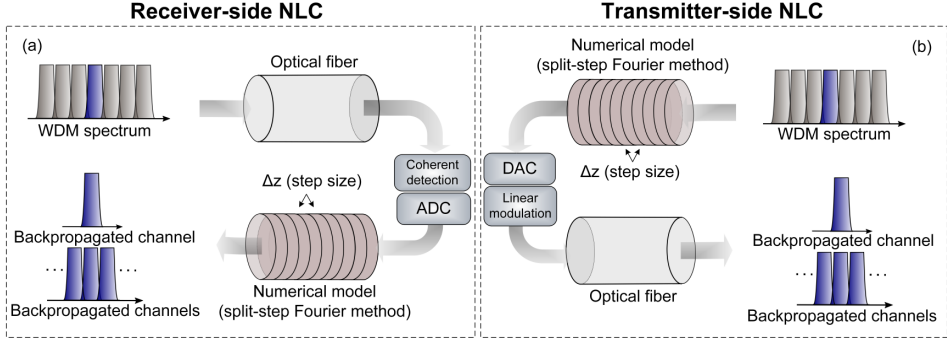
Figure 2.8 DBP-based Kerr nonlinearity compensation schemes. (a) DBP is performed with the SSFM at the receiver, after coherent detection and analog-to-digital conversion. (b) DBP is performed with the SSFM at the transmitter, before the ADC stage.

Interestingly, the concatenation of operators $[\hat{\mathbf{D}}, \hat{\mathbf{N}}]$ is also invertible. In particular, for each $[\hat{\mathbf{D}}, \hat{\mathbf{N}}]$ pair defining a *forward step* of field propagation, one can also define $[-\hat{\mathbf{N}}, -\hat{\mathbf{D}}]$ as a *backward step* such that the combination of both is the identity operator. This property is the basis for the concept of DBP.

The goal of DBP is to compensate the dispersion and Kerr nonlinearities of a given fiber channel jointly, by processing its input or output signals with the SSFM and the backward operators $[-\hat{\mathbf{N}}, -\hat{\mathbf{D}}]$.

Figure 2.8 shows the two ways DBP can be implemented. The most popular practice is to process the coherently detected signals at the receiver (Fig. 2.8(a)). Alternatively, DBP can be used to pre-distort the waveforms before digital-to-analog conversion at the transmitter (Fig. 2.8(b)). The NLC can also be split between transmitter and receiver. Single or multiple WDM channels can be backpropagated depending on the analog bandwidth available for signal processing at transmitters or receivers.

The DBP algorithm is an effective method to compensate the deterministic NLI (see Fig. 2.5). The accuracy of DBP based on the SSFM will depend on the knowledge of the fiber parameters for CD, PMD and Kerr nonlinearity. Because this information may not be available or carry a degree of uncertainty, parameter adaptation or system identification procedures are often necessary to maximize the performance of the DBP-based NLC. Several variants of DBP algorithms have been proposed. However, the biggest obstacle for practical DBP implementation is the computational complexity of the SSFM. By increasing the optical bandwidth being processed, the discretization requirements of time (sampling rate) and space

(step size) become progressively stringent, resulting in quick growth of the memory and number of Fast Fourier Transforms (FFTs) required to process the data of a given fiber channel.

Further discussion on DBP will be conducted in the chapters 3, 4, and 5.

Carrier phase recovery

Since coherent optical receivers use intradyne detection, carrier phase recovery has to be later performed to track frequency offsets (FOs) and phase variations between transmitter and receiver LOs.

Unlike ideal CW carriers, real lasers are not perfectly coherent light sources. Instead, optical carriers are subject to random variations of phase and central frequency. The level of spectral coherence of a laser is commonly defined by its linewidth Δf. Most of the lasers used in optical coherent transceivers can be characterized by a normalized Lorentzian-shaped PSD $L_{cw}(f)$ given by

$$L_{cw}(f) = \frac{2}{\pi} \frac{\Delta f}{[(\Delta f)^2 + 4(f - f_c)^2]}, \tag{2.27}$$

where fc is the laser central frequency. The linewidth Δf is then defined as the full-width at half-maximum (FWHM) bandwidth of $L_{cw}(f)$.

In the time domain, the evolution of the carrier phase can be modeled as a Wiener process, where the random phase shifts $\Delta\phi$ are Gaussian distributed with zero mean and variance σ_ϕ^2, i.e., $\Delta\phi \backsim \mathcal{N}(0, \sigma_\phi^2)$. Assuming that the phase noise process is uniformly sampled at intervals spaced by T_s, we have that

$$\sigma_\phi^2 = 2\pi \Delta f T_s. \tag{2.28}$$

In the coherent detection process, both transmitter and receiver LOs contribute to the overall phase noise present in the downconverted signal, such that the equivalent variance of the phase noise will be proportional to the sum of each LOs' linewidth.

Phase recovery DSP algorithms are implemented in coherent optical receivers to track and compensate for the laser phase noise [46]. Since the performance of these algorithms is bounded by σ_ϕ^2, Eq. (2.28) is widely used to specify the tolerance to laser linewidths for a given baud rate and modulation format.

In this thesis, when necessary, carrier recovery was performed with a digital phase-locked loop (PLL) [49] or an extended Kalman filter [50]. Exceptionally, in Chapter 5, the trellis-based phase recovery method of [51] was used.

2.5 Summary

The purpose of this chapter has been to provide a short review of fundamental concepts of coherent optical communication systems. The topics discussed include transmitters, the fiber channel model, the structure of a coherent receiver and the standard DSP blocks involved in the estimation of the transmitted data. Especially, the instantaneous Kerr nonlinear distortions in SMF fiber were discussed, and the principle of DBP presented. This framework of concepts constitutes a support for most of the discussions placed in the remaining chapters of this thesis.

Part I

Kerr nonlinearity compensation

Chapter 3

On the impairment mitigation in superchannels with DBP and MLSD

The use of superchannels in coherent optical communications has been proposed as an option to reduce the bandwidth requirements of optoelectronic components in transceivers that aggregate large transmission rates, such as Tb/s or multi-Tb/s [52, 53]. The concept of superchannel is defined in [54] as a set of closely packed carriers that travel from the same origin to the same destination in a wavelength-division multiplexing (WDM) system. Superchannels are also an enabling technology for elastic networks [55], which are networks tailored to approach the optimal use of the physical layer resources and, in particular, the spectrum available for transmission. Moreover, superchannel-based variable-rate transceivers have been proposed [56, 57] to maximize throughput given a targeted reach.

Superchannel transmitters can be projected in several configurations concerning the number of subcarriers and how the information is distributed among them [54]. The same applies to the receivers. In this sense, the digital signal processing (DSP) architectures in superchannel receivers may have different requirements depending on how the transmitter is conceived, how each subcarrier is detected and which impairments should be compensated. Specifically, the effectiveness of Kerr nonlinear distortion compensation may imply in distinct requirements for different receiver structures [58–61]. Therefore, the development of DSP for superchannel receivers is a topic that has attracted the attention of researchers and industry, and that is the motivation behind the work reported in this chapter.

This chapter is based on the author's original publications [C13] and [J6].

3.1   Introduction

Multicarrier transmission techniques allied with advanced modulation formats and pulse shaping [62] have been extensively assessed in optical communication systems. The parallelism concept of superchannel architectures has become attractive due to lower requirements on the speed of electronics necessary to increase the transponders' throughput, although its feasibility also demands highly integrated photonic devices [63,64]. However, because the transmitted subcarriers are tightly allocated within the superchannel bandwidth, impairments originated from linear crosstalk [53], nonlinear Kerr effects and combinations of both may impose significant penalties to the transmission performance. From this perspective, in order to maximize the performance, the receiver's DSP should be robust to both kinds of impairments.

Pulse shaping techniques to constraint modulated bandwidth, such as digital Nyquist filtering [65] and optical pre-filtering [66–68], have been explored to minimize linear crosstalk penalties in multicarrier communications. The benefits of those techniques have been experimentally assessed in long-haul optical transmission systems. However, for superchannels close to the Nyquist limit, crosstalk can not be eliminated due to the practical limitations to obtaining zero roll-off modulated spectra.

Although it is well known that linear crosstalk can be compensated using multiple-input multiple-output (MIMO) based equalizers, for high bandwidth superchannels, joint carrier MIMO equalization techniques may require the receiver to operate with non-realistic sampling rates. Concurrently, nonlinearity compensation (NLC) methods based on DSP have been extensively investigated to improve the robustness of the receivers against fiber nonlinear impairments. In particular, digital backpropagation (DBP) [16], perturbation equalizers [17] and maximum likelihood sequence detection (MLSD) [69] have been explored.

Previous works have investigated optimum performance bounds of DSP strategies, and transmitter/receiver architectures for different scenarios. In [70], perturbation based nonlinearity mitigation is numerically evaluated in WDM transmissions, with different pulse shaping and transmitter/receiver bandwidths, however, not targeting superchannel scenarios. In [58], the optimum bandwidth for superchannel NLC using DBP was assessed, but

without detailed analysis on the impact of the linear impairments. MLSD strategies have been considered in [69] for intrachannel NLC, without taking into account multicarrier or superchannel scenarios.

In this chapter, the first contribution of this thesis is presented. Here an extensive numerical investigation is reported regarding the combined performance of NLC with single-carrier digital backpropagation (SC-DBP) and MLSD in a quasi-Nyquist superchannel transmission over standard dispersion uncompensated fiber links. Three distinct cases of carrier spectral shaping are investigated: small roll-off raised cosine and two optically pre-filtered transmitters.

The rest of the chapter is divided as follows. In Section 3.2, the numerical model considered for the analysis is detailed. In Section 3.4, the numerical results obtained are discussed. In particular, a comparison between dual polarization quadrature phase-shift keying (DP-QPSK) and dual polarization 16QAM (DP-16QAM) quasi-Nyquist superchannels is carried out, to evaluate the influence of the modulation format on the gains achieved by the studied algorithms. It is assumed that the receiver uses independent parallel processing for each subcarrier, without any MIMO processing or multicarrier NLC.

3.2 Numerical simulation model

The numerical simulation model illustrated in Fig. 3.1 was used to investigate the performance of SC-DBP and MLSD for different superchannel configurations. The transmitted spectrum was composed of five phase-locked carriers modulated at 32 GBd. The transmission was simulated for various carriers frequency separation, varying from 45 to 32.5 GHz, with 2.5 GHz granularity, to quantify the impact of crosstalk as a function of the pulse shaping. The transmitter was configured to generate three different scenarios of narrow spectrally modulated carriers: pre-filtered non-return-to-zero (NRZ) (Fig. 3.1(b.1)), pre-filtered return-to-zero (RZ) with 50% duty cycle (Fig. 3.1(b.2)) and raised cosine (RC) with 1% of roll-off factor (Fig. 3.1(b.3)). NRZ pulses were generated with ideal rectangular shape, while RZ 50% pulse shape corresponds to the one described in [71].

The bit sequences used are decorrelated sections of a pseudo-random binary sequence (PRBS) with length $2^{23} - 1$. The sections had a fixed length of 2^{19} bits per carrier. The symbol sequences of different carriers were arbitrarily decorrelated randomly by at least 173 symbols. For all tested cases, the carriers were synchronized in time. After constellation
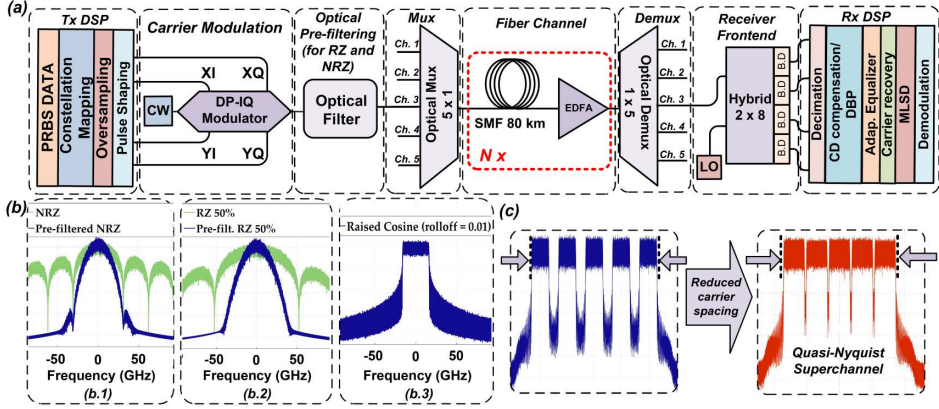
Figure 3.1 Schematic of the simulation setup. (a) Block diagram of the transmitter, fiber channel and coherent receiver. (b) Spectra used for comparison: (b.1) PF-NRZ, (b.2) PF-RZ 50%, (b.3) RC (roll-off = 0.01). (c) Modulated carriers' spectrum (RC pulse shaping).

mapping, the data was oversampled to 16 samples per symbol. Following pulse shaping and optical modulation, narrow pre-filtering of RZ and NRZ spectra was performed by a passband optical filter modeled with a Gaussian attenuation profile (according to the WaveShaper filter models [72]) and 3 dB bandwidth of 25 GHz, located after the dual polarization in-phase/quadrature (IQ) modulator. This filter was bypassed in the RC pulse shaping configuration. The optical multiplexing stage (MUX) was considered ideal, imposing no extra filtering to the carriers. The signal was transmitted over 3600 km (45×80 km) for the DP-QPSK modulation, and the over 800 km (10×80 km) when modulated with DP-16QAM. Both cases simulated uncompensated dispersion links with lumped amplification based on Erbium-doped fiber amplifiers (EDFAs).

The fiber spans were modelled with the following typical parameters: $\gamma = 1.3\ W^{-1}\text{km}^{-1}$ (nonlinear coefficient), $\alpha = 0.2$ dB/km (fiber attenuation), $D = 16.6$ ps/nm/km (chromatic dispersion (CD) parameter), $L = 80$ km (span length), $G_{EDFA} = 16$ dB (EDFA gain), $NF_{EDFA} = 4.5$ dB (EDFA noise figure). All results presented refer to the central carrier performance. The optical field propagation within the fiber was simulated applying symmetric split-step Fourier method (SSFM) to solve the vectorial coupled mode form of the nonlinear Schrödinger equation (NLSE) numerically, as it is described in [8]. The polarization mode dispersion (PMD) effects were disregarded. SC-DBP was performed with a fixed step size of

$\Delta z = 20$ km (4 steps/span). The equivalent lowpass frequency response of the optical demultiplexer (DEMUX) and optical coherent receiver front-end was simulated with Gaussian-shaped frequency response with a 3 dB bandwidth of 24 GHz, for all cases. This value was chosen to match the specifications of standard commercial devices.

A set of DSP algorithms [73] was applied to compensate for channel impairments and estimate the transmitted data: decimation to 2 samples/symbol, frequency domain chromatic dispersion equalization or DBP, adaptive equalization with the constant modulus algorithm (CMA) (21 taps) for DP-QPSK, and multimodulus algorithm (MMA) (21 taps) for DP-16QAM, carrier recovery with digital phase-locked loop (PLL), MLSD, digital demodulation and error counting.

3.3 MLSD algorithm

Assume that the channel memory causes intersymbol interference (ISI) over an interval limited to N consecutive symbols. Given a vector $\mathbf{r}_k$ with a sequence of N consecutive received signal samples $\mathbf{r}_k = [r_k...r_{k-(N-1)}]$ at the k-th symbol period, the MLSD algorithm should decide on the corresponding transmitted constellation symbol x_k for which the conditional probability $p(x_k|\mathbf{r}_k)$ is maximized. This problem is equivalent to the problem of finding the corresponding sequence of states of the channel $\mathbf{s}_k = [s_k...s_{k-(N-1)}]$ that maximizes $p(\mathbf{s}_k|\mathbf{r}_k)$ [35].

The states of the channel are defined as the possible values that the received signal sequences $\mathbf{r}_k$ can assume in the absence of noise, given the sequences of transmitted symbols $\mathbf{x}_k = [x_k...x_{k-(N-1)}]$. Assuming that the noise is circular and Gaussian with zero mean, the channel states can be obtained by observing the output of the channel [74–76] over N consecutive symbol intervals $\mathbf{r}$ and performing the following expectation

$$\mathbf{s}_m = E[\mathbf{r}|\mathbf{x}_m], \tag{3.1}$$

where $\mathbf{s}_m$ is the state associated with the m-th sequence of transmitted symbols $\mathbf{x}_m$. Note that, for a constellation with cardinality M, there will be M^N channel states.

Here, $\mathbf{r}$ is assumed to be the output of the adaptive equalizer and carrier phase recovery blocks. In the simulations performed, the adaptive equalizer was used to approximate the matched filter at the receiver for each tested configuration. The expectation in Eq. (3.1) is approximated using

35

histograms of $\mathbf{r}$, obtained using training sequences (8×10^4 symbols per polarization), and the estimated states $\mathbf{s}$ are stored in a lookup table.

The MLSD is performed per polarization at one sample per symbol, based on a minimum Euclidean distance metric. At the receiver, a sequence $\hat{\mathbf{x}}_k$ is decided after comparing $\mathbf{r}_k$ with all possible entries $\mathbf{s}$ in the lookup table, i.e.,

$$\hat{\mathbf{x}}_k = \arg \min_{\mathbf{x}_m} \|\mathbf{r}_k - \mathbf{s}(\mathbf{x}_m)\|_2, \tag{3.2}$$

where $\|\mathbf{x}\|_2$ denotes the Euclidean norm of $\mathbf{x}$.

Since the memory considered in the MLSD is shorter than the actual memory of the nonlinear fiber-optic channels assumed in the simulations, and circular additive white Gaussian noise (AWGN) statistics are assumed, the detection strategies adopted in this work are generally sub-optimal.

3.4   Numerical results

The results obtained by numerical simulations are presented in this section. The chosen figure of merit for performance assessment is the Q^2-factor, in dB, which is calculated from the bit-error rate (BER) according to $Q^2_{dB} = 20 \log_{10}[\sqrt{2}\mathrm{erfcinv}(2BER)]$.

3.4.1   5 × 32 GBd DP-QPSK superchannel

Figure 3.2 depicts in contour plots the Q^2-factor gain compared to electronic compensation of chromatic dispersion (EDC) only, obtained with SC-DBP as a function of carrier separation and fiber input power for DP-QPSK superchannel transmission. These results illustrate how the performance of SC-DBP is affected by inter-carrier interference for each transmitter configuration.

For coarse inter-carrier spacing ($\geq$ 40 GHz), SC-DBP results in similar performance improvement values in the nonlinear transmission regime for all three configurations. However, as carrier frequency spacing decreases towards quasi-Nyquist superchannel, the Q^2-factor improvement provided by SC-DBP per input power is less affected in the low roll-off RC configuration, what becomes evident by observing the bending of the contour lines in the density plots. This can be explained considering that a higher level of crosstalk increases the impact of inter-carrier nonlinear effects, which should reduce the single carrier NLC performance.
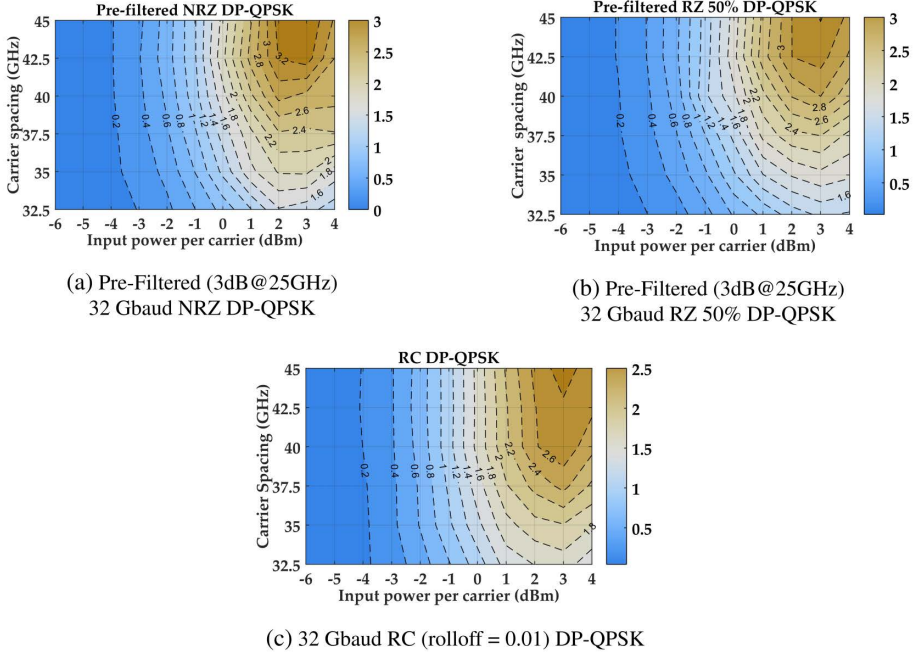
Figure 3.2 Q^2-factor improvement after SC-DBP as function of carrier spacing and fiber input power for the DP-QPSK superchannel after 3600 km transmission.

After comparing all three superchannel configurations, it can be concluded that modulated carriers with low roll-off Nyquist spectra provide performance robustness for SC-DBP in quasi-Nyquist superchannels, additionally to minimization of linear crosstalk interference.

The performance of MLSD is then investigated. Figure 3.3 shows the Q^2-factor gain obtained with 16, 256 and 4096 MLSD states (2, 4 and 6 taps, respectively) for 32.5 GHz frequency spacing, with and without NLC by SC-DBP. Under low crosstalk conditions (i.e, for coarse carrier frequency spacings) negligible performance improvement is obtained by MLSD compared with SbS decisions. However, approaching quasi-Nyquist carrier spacing (i.e., increasing crosstalk), MLSD and SbS strategies show distinct performances.

A Q^2-factor improvement of 0.5 dB over SbS decisions is obtained by MLSD at optimum fiber input power (-2 dBm$\leq P_{opt} \geq$-1 dBm), for systems with pre-filtering. This gain is attributed to linear crosstalk mitigation rather than intra-carrier NLC, since it is approximately constant for both linear regime and nonlinear regime after DBP.

(a) Pre-Filtered (3dB@25GHz)
32 Gbaud NRZ DP-QPSK

(b) Pre-Filtered (3dB@25GHz)
32 Gbaud RZ 50% DP-QPSK

(c) 32 Gbaud RC DP-QPSK
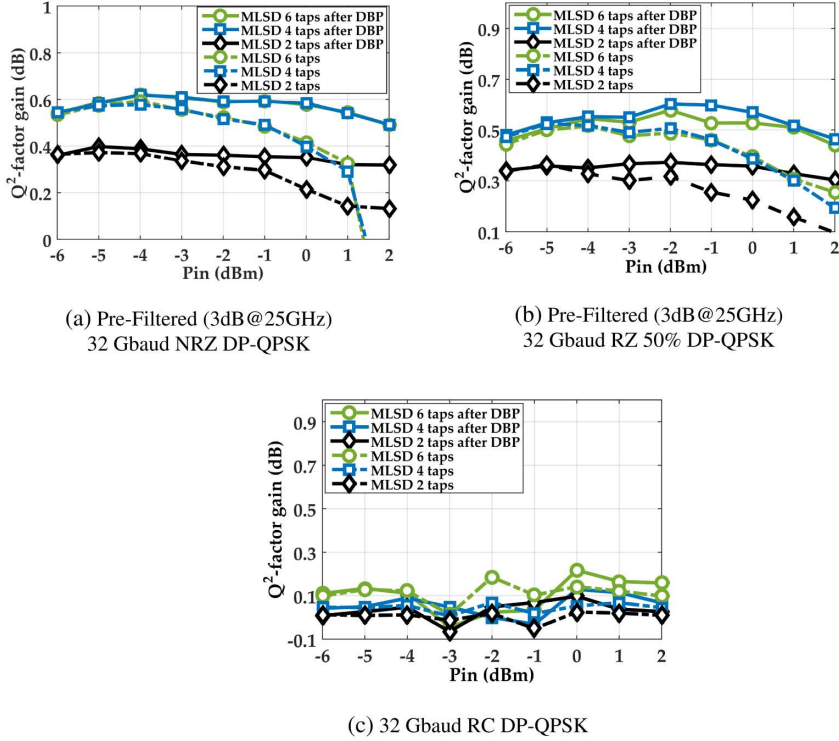
Figure 3.3 Q^2-factor improvement of MLSD compared with SbS decisions as function of fiber input power per carrier with 32.5 GHz carrier spacing for the DP-QPSK superchannel after 3600 km transmission.

The benefit by MLSD decreases faster in the nonlinear regime as the transmitted power increases if SC-DBP is not previously applied, due to the increasing weight of the nonlinear impairment in the overall noise variance. Additionally, no improvement is obtained using MLSD with RC configuration (Fig. 3.3(c)). It is shown (Fig. 3.3(a) and 3.3(b)) that the performance gain provided by MLSD saturates when more than four memory taps are considered, which indicates the time window limit for linear crosstalk effects that can be mitigated. In the absence of linear crosstalk, MLSD is not able to improve the performance compared with SbS decisions, and it may penalize it in some cases, due to error propagation of wrong symbol decisions, as the negative Q^2-factor gain values of Fig. 3.3 indicate.

Figure 3.4 shows the Q^2-factor versus input power per carrier for the quasi-Nyquist superchannel configuration. For this investigation, MLSD was

(a) Pre-Filtered (3dB@25GHz)
32 Gbaud NRZ DP-QPSK

(b) Pre-Filtered (3dB@25GHz)
32 Gbaud RZ 50% DP-QPSK

(c) 32 Gbaud RC DP-QPSK
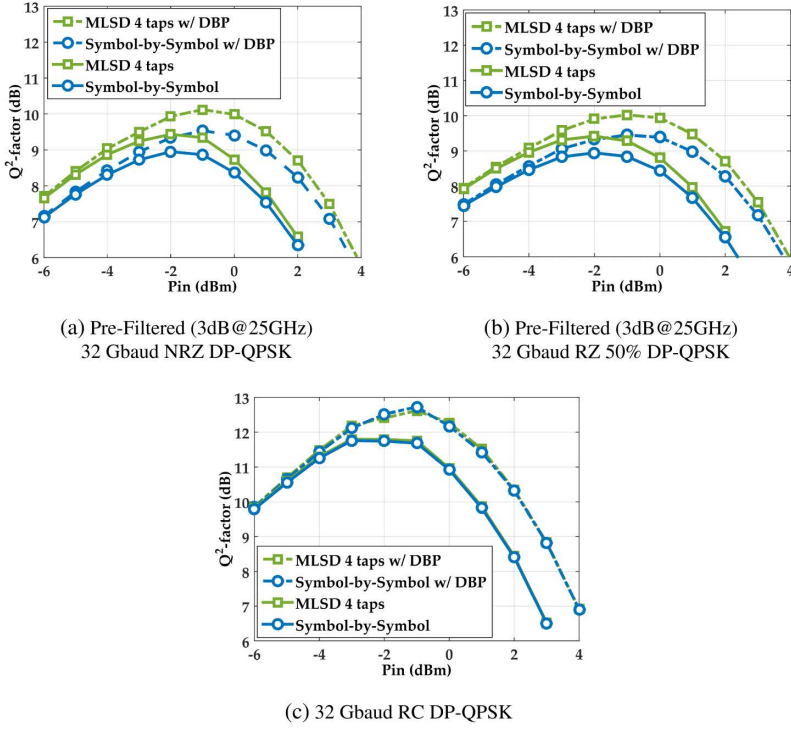
Figure 3.4 Q^2-factor as function of fiber input power per carrier for the 32.5 GHz carrier spacing configuration for the DP-QPSK superchannel after 3600 km transmission.

configured with 4 memory taps. For pre-filtered transmitters (Fig. 3.4(a) and 3.4(b)), at the optimal input power (-2 dBm) the Q^2-factor improvement of combined SC-DBP and MLSD is 1.0 dB.

In the nonlinear transmission regime with crosstalk, the gain of MLSD is degraded, and the performance curve tends to converge to the same obtained by SbS decisions. However, the combination of DBP and MLSD still improves the Q^2-factor by around 2.0 dB in the nonlinear transmission regime, compared with EDC and SbS detection. When the carriers experience low levels of crosstalk (Fig. 3.4(c)), SC-DBP provides the same 1.0 dB margin of improvement at the optimal input power, which is the expected value for single-carrier NLC [77, 78] in multicarrier transmission scenarios.

Finally, as depicted in Fig. 3.4(c), MLSD and SbS decisions have the same performance if the transmitter is configured with RC pulse shaping, either using DBP, or not. Such similarity can be explained by the Gaussian characteristic of the nonlinear impairments in long-haul dispersion uncom-

pensated links [42]. In this case, as the nonlinear impairment approximately behaves as uncorrelated additive Gaussian noise, its statistics also average out when the receiver searches for the probabilities distributions to be used in the MLSD stage.

3.4.2 5 × 32 GBd DP-16QAM superchannel

Figure 3.5 shows the gain in Q^2-factor provided by SC-DBP as a function of carrier frequency separation and fiber input power for the DP-16QAM super-channel transmission. The optimum input power was -1 dBm without and 0 dBm with SC-DBP. It can be noticed that, as the carrier spacing decreases, the area with DBP gain greater than 1 dB is reduced when compared to the DP-QPSK case (Fig. 3.2). These results indicate that the impact of inter-carrier crosstalk on SC-DBP performance depends on the modulation format, as also pointed out in [13, 43].

(a) Pre-Filtered (3dB@25GHz)
32 Gbaud NRZ DP-DP-16QAM

(b) Pre-Filtered (3dB@25GHz)
32 Gbaud RZ 50% DP-16QAM

(c) 32 Gbaud RC (rolloff = 0.01) DP-16QAM
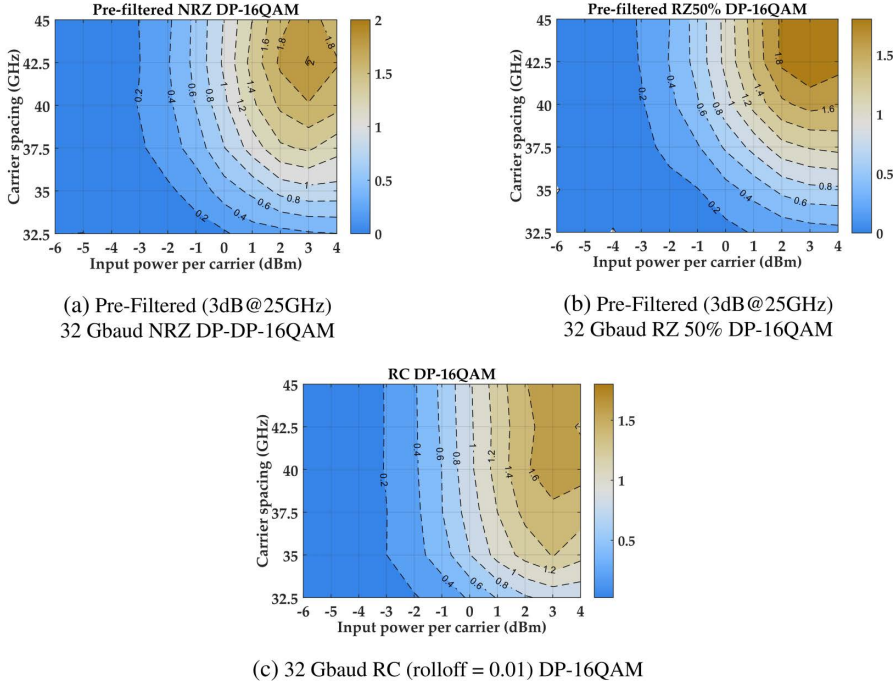
Figure 3.5 Q^2-factor improvement of SC-DBP as function of carrier spacing and fiber input power for the DP-16QAM superchannel after 800 km transmission.

Figure 3.6 shows the maximum Q^2-factor value obtained at the optimum

input power as a function of the carrier spacing for DP-16QAM superchannel transmission.

(a) Pre-Filtered (3dB@25GHz)
32 Gbaud NRZ DP-16QAM

(b) Pre-Filtered (3dB@25GHz)
32 Gbaud RZ 50% DP-16QAM

(c) 32 Gbaud RC DP-16QAM
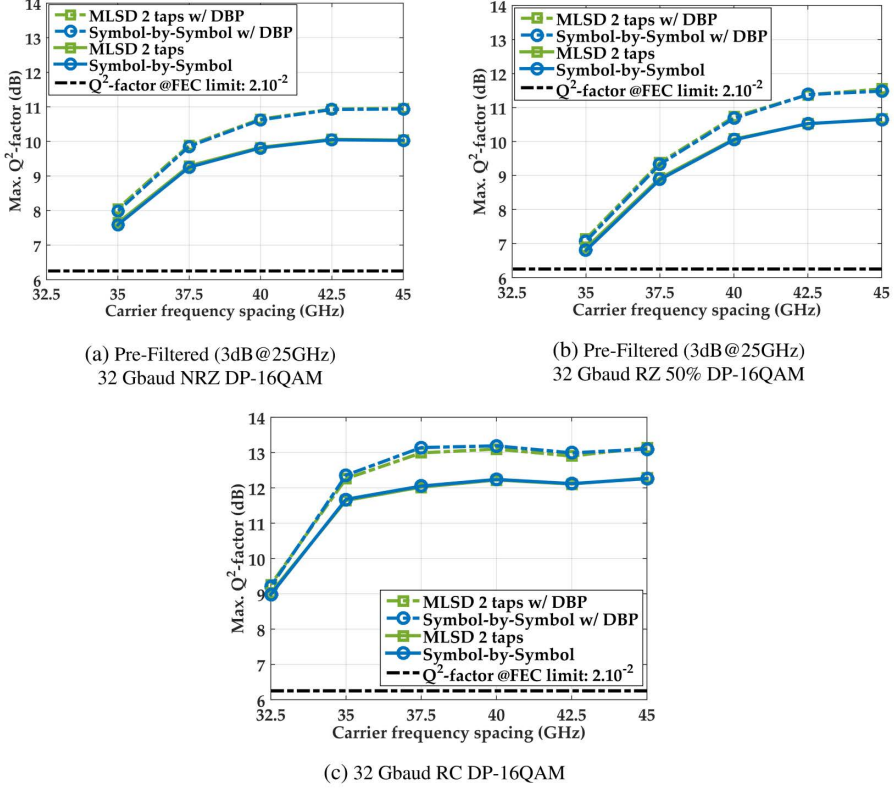
Figure 3.6 Maximum Q^2-factor as function of carrier spacing configuration for the DP-16QAM superchannel after 800 km transmission.

For coarse carrier spacing, SC-DBP provides a Q^2-factor improvement of 1.0 dB for all cases. This gain tends to vanish when the carriers move to the quasi-Nyquist superchannel configuration. For pre-filtered transmitters (Fig. 3.6(a) and 3.6(b)), the minimum allowed frequency spacing with Q^2-factor above the forward error correction (FEC) limit is 35 GHz. The crosstalk penalty is higher for the pre-filtered RZ 50% case than for the pre-filtered NRZ, due to the broader spectrum of the former.

Among all tested cases, only the RC pulse-shaping case is robust enough to provide acceptable pre-FEC performance at 32.5 GHz of carrier spacing. However, the Q^2-factor improvement due to SC-DBP reduces to 0.2 dB,

in agreement with similar experimental results shown in [79]. Using two memory taps ($16^2 = 256$ states), no improvement is provided by MLSD. Further increment to four memory taps MLSD ($16^4 = 665536$ states!) was not considered due to complexity constraints to run the algorithm.

3.4.3 Comments on the MLSD crosstalk mitigation performance

Although no detailed analysis of the mechanisms that allow MLSD to mitigate linear crosstalk penalties was targeted in this work, we can conjecture based on [80, 81]. Qualitatively, we can indicate that given the DSP configuration set in the receiver, the training rule to adapt the equalizer taps may indirectly choose a narrow bandwidth filter structures that suppress crosstalk from neighbor carriers. In other words, it may "translate" linear crosstalk penalty in a linear ISI penalty, which then can be mitigated with MLSD.

The negligible gain of MLSD in the DP-16QAM case can be attributed to two reasons: a large number of channel states which are not well separated in the Euclidean space, and insufficient signal-to-noise ratio at the receiver. Further investigation would be required to define the limits of MLSD performance for each modulation format.

3.5 Summary

Combined performance of single-carrier digital backpropagation and maximum likelihood sequence detection has been investigated for mitigation of linear and nonlinear impairments in optical DP-QPSK and DP-16QAM superchannels generated with three distinct spectral shaping techniques: optical pre-filtering of RZ and NRZ spectra, and digital Nyquist filtering. We evaluate the impact of superchannel carrier spacing on the performance of each algorithm.

The numerical results obtained indicate that the use of both algorithms can complementary provide, at the nonlinear threshold, up to 1.0 dB of Q^2-factor improvement, over standard chromatic dispersion compensation in the digital domain. However, we showed that MLSD is only advantageous for transmitters using optical spectral shaping, in configurations where linear inter-carrier crosstalk is present.

The results obtained for DP-QPSK with the DP-16QAM indicated that the impact of the impairments scale with the order of the modulation format,

suggesting that, for dense superchannels transmitted over long-haul dispersion uncompensated links, the combination of both techniques is more effective for low-order modulation formats.

Chapter 4

Impact of frequency-referenced transmission on the full-field multicarrier digital backpropagation

The analysis and results presented in Chapter 3 have only considered the compensation of intra-carrier Kerr nonlinear distortions with single-carrier digital backpropagation (SC-DBP). However, if the number of co-propagating carriers in a wavelength-division multiplexing (WDM) system can be coherently detected and jointly processed in the digital domain, the deterministic inter-carrier nonlinear distortions can also be compensated simply by performing a joint backpropagation, or multicarrier digital backpropagation (MC-DBP), of the entire set of carriers. Some of the first investigations of multicarrier nonlinearity compensation (NLC) were reported in [83–88]. The state-of-the-art of NLC using MC-DBP has been expanded in the last few years with numerical investigations and experimental demonstrations.

In [60], five synchronized coherent receivers [1] are used to detect the entire electrical field of a 5×32 GBd dual polarization 16QAM (DP-16QAM)

---

[1]a bank of multiple synchronized coherent receivers used to detect a broadband signal is known in the literature of optical communications by the term "spectrally-sliced" receiver.

superchannel. After a pre-processing to reconstruct the multicarrier signal in the digital domain, full-field MC-DBP is applied providing a maximum performance gain of 1.0 dB in the Q^2-factor after 960 km of transmission over Truewave Reduced Slope fiber.

In [58], the performance of NLC with full-field MC-DBP is numerically assessed considering dispersion uncompensated transmission over standard single-mode fiber (SSMF). The performance of NLC is investigated as a function of the digital backpropagation (DBP) precision and number of jointly processed carriers. It is shown that the optimum parameters for the algorithm vary substantially as the number of processed carriers increase. In particular, MC-DBP requires a more precise tuning of the channel parameters.

In [59, 89], the extension of the maximum transmission reach enabled by MC-DBP is experimentally evaluated. Both demonstrations assumed superchannels with seven closely spaced subcarriers modulated at 10 GBd. In [59], the maximum reach is extended by 85% from 3190 km to 5890 km, for the DP-16QAM modulation format. In [89], 100% of maximum reach extension is obtained, from 640 km to 1280 km, for the dual polarization 64QAM (DP-64QAM) modulation format. A similar investigation is performed for unrepeated transmission links in [90, 91].

In [92], MC-DBP is experimentally investigated for 400 Gb/s superchannels in WDM systems with 75 GHz of grid spacing. Long-haul (2×31.5 GBd DP-16QAM and 3×21 GBd DP-16QAM) and shorter-reach scenarios (3×14 GBd DP-64QAM) are considered. A comparison between full-field MC-DBP and coupled-equations MC-DBP is presented showing that the second approach can be more effective given some implementation constraints.

Still in the 400 Gb/s superchannels scenario, in [93] MC-DBP is compared against a Volterra-based nonlinear equalizer. It is shown that when the number of jointly processed carriers increases, the Volterra equalizer performs similarly to full-field MC-DBP, but operating with 1 sample/symbol and, hence, reducing the computational complexity of the multicarrier NLC.

In [94–96], MC-DBP is implemented at the transmitter as pre-distortion of the modulated subcarriers. It is demonstrated that the performance of the NLC is largely improved when the pre-distorted carriers are locked in frequency (frequency-referenced carriers), as addressed in [61]. In [95], pre-distortion and frequency-locking enables a two-fold reach increase of a single polarization multicarrier signal, composed by three carriers separated by 25 GHz and modulated with 16quadrature amplitude modulation (QAM)

at 16 GBd. Further experimental investigation of this technique is shown in [97] to enabling a reach tripling of a 3×24 GBd DP-64QAM multicarrier signal, from 425 km to 1275 km.

Therefore, MC-DBP has received considerable attention from the research community as a digital signal processing (DSP)-based technique for NLC.

This chapter summarizes one of the contributions of the thesis related to this topic, consisting in the first experimental investigation of the impact of frequency-referenced long-haul transmission on the performance of receiver-side full-field MC-DBP for polarization multiplexed systems. The content presented here is an extension of the work originally reported in [C12].

4.1   Introduction

Inter-channel nonlinear interference (NLI) induced by the Kerr effect plays a major role in limiting the achievable information rates of optical communication systems over single mode fibers [9,11]. Similarly to the intra-channel NLI, a deterministic fraction of the inter-channel NLI can be compensated via DSP. However, due to the strong data dependent characteristics of the Kerr distortions [43], its compensation requires the joint processing, at the receiver or the transmitter, of all co-propagating carriers within the fiber. This is not always possible in a dynamic network environment, where interfering carriers can be routed through different paths at different nodes. Nevertheless, mainly in point-to-point system scenarios, multicarrier NLC schemes have been investigated.

However, as discussed in [61], because multicarrier NLC techniques rely on approximated models for the nonlinear fiber channel, a fundamental limitation to their effectiveness arises from the inherent uncertainty in the frequency spacing between interfering carriers in a WDM system. The frequency-referenced transmission was proposed in [61] to tackle this problem. In this scheme, all transmitted carriers come from a stable optical frequency comb, hence preserving a fixed frequency separation. Such strategy has been proved to benefit multicarrier NLC when performed by applying nonlinear pre-distortion at the transmitter.

Experimental investigations on the performance of multicarrier nonlinear pre-distortion for frequency-referenced and frequency-unlocked carrier transmission have been presented in [94–96]. However, no study is provided regarding the impact of such scheme on the performance of full-field MC-DBP at the receiver. Additionally, [94–96] investigate for single-polarization

systems.

Because the signal-to-noise ratio (SNR) decreases from the start to the end of transmission, pre-distortion techniques for NLC are more efficient in compensating the NLI of the first spans of the fiber link, where the accumulated noise power is smaller and has less impact on the NLI when compared to the last spans. For multicarrier NLC, however, pre-distortion demands extra effort on the transmitter design. In this aspect, receiver full-field MC-DBP has a lower implementation complexity than nonlinear pre-distortion, since the last one implies further requirements on synchronization, analog bandwidth, and resolution of digital-to-analog converter (DAC)s at the transmitters. More importantly, full-field MC-DBP based on split-step Fourier method (SSFM) does not assume any *a priori* carrier frequency allocation to perform the inverse channel propagation. Therefore, the use of frequency-referenced transmission may result in different performance impacts, if NLC is carried out using *receiver-side* MC-DBP instead of nonlinear pre-distortion at the transmitter. Moreover, since NLC can also be split between transmitter and receiver, the use of both pre-distortion and DBP it is shown to be advantageous [98] and, therefore, it is important to understand the influence of frequency-referenced transmission in both cases. In [59], the performance of MC-DBP is evaluated in a transmission setup with frequency-locked carriers. However, no comparison to the case of unlocked carriers transmission is provided.

Nevertheless, the understanding of the frequency stability influence on the NLC performance is an important matter for practical design of transmission systems and NLC techniques. That is the main motivation of the work reported in this chapter.

The following analysis details an experimental evaluation of the performance gains obtained with MC-DBP. In the experimental study, the transmission of a 4 × 8 GBd dual polarization quadrature phase-shift keying (DP-QPSK) multicarrier system is considered, with and without the use of frequency-referenced carriers, up to 4000 km of reach.

The remaining of the chapter is organized as follows. In Section 4.2, a detailed description of the experimental setup is shown. In Section 4.3, the results obtained after offline processing of the experimental data are discussed. Section 4.4 summarizes the main conclusions.

4.2   Experimental setup

The experimental setup is shown in Fig. 4.1.
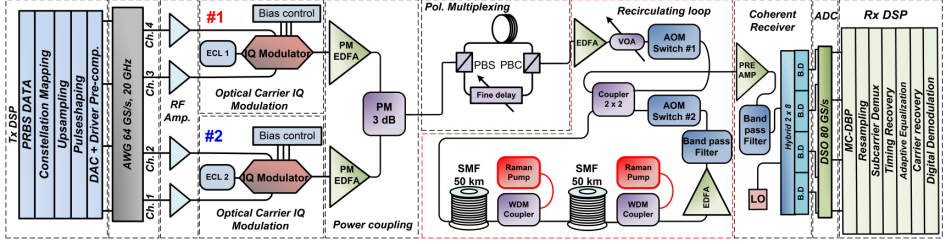
Figure 4.1 Experimental setup used to evaluate the performance of receiver-side MC-DBP in frequency-referenced polarization multiplexed long-haul transmission.
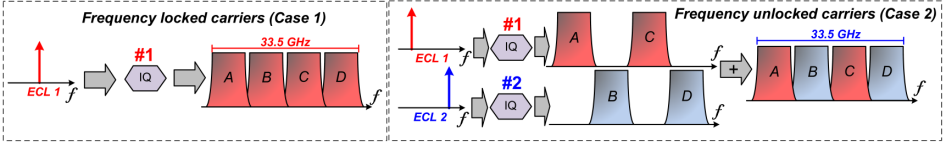
Figure 4.2 Schematic of the two configurations used to generate the transmitted carriers. (a) Only one laser is modulated. Four decorrelated carriers spaced of 8.5 GHz are generated directly from the AWG output. (b) Two free-running lasers are modulated by different IQ modulators. The AWG output generates two carriers spaced by 17 GHz. Four decorrelated carriers spaced of 8.5 GHz are obtained after 3 dB coupling, with even, and odd originated from different lasers.

At the transmitter, two in-phase/quadrature (IQ) modulators and two independent external cavity lasers (ECLs) with 100 kHz linewidth are used. The central frequencies of the two lasers are separated by 8.5 GHz. The baseband signals driving the modulators are synthesized by an AWG with a sampling rate of 64 GSa/s and analog bandwidth of 20 GHz. The AWG's outputs are amplified to 5.0 V of peak-to-peak amplitude to drive the IQ modulators. Offline DSP is applied to pre-compensate the combined frequency response of the AWG outputs, radio frequency (RF) cables, and amplifiers.

The modulated baseband signals synthesized by the AWG are generated in two different subcarrier configurations. In Case 1, only modulator #1 in Fig. 4.1 is driven. The two AWG outputs connected to #1 generate four decorrelated quadrature phase-shift keying (QPSK) subcarriers. All subcarriers are modulated at 8 GBd, with root raised cosine (RRC) pulse shape with a roll-off factor of 1%, and separated by 500 MHz (6.25% of the baud rate) guard bands, as shown in Fig. 4.2 (a). Therefore, in this configuration, the modulator #1 outputs a multicarrier signal with four frequency-locked subcarriers which are subsequently amplified by a polarization maintaining (PM) Erbium-doped fiber amplifier (EDFA).

49

In Case 2, modulators #1 and #2 in Fig. 4.1 are driven simultaneously. The AWG sends two decorrelated QPSK subcarriers to each modulator, each subcarrier modulated at 8 GBd, with RRC pulse shape (roll-off factor of 1%), and separated by 17 GHz, as shown in Fig. 4.2 (b). The outputs of the modulators are amplified by PM EDFAs and combined with a 3 dB PM coupler. Therefore, the multicarrier signal in Case 2 has the same characteristics of the one in Case 1, but with even and odd subcarriers originating from two independent free-running lasers. Although in Case 2 not all subcarriers are unlocked in frequency, such configuration is valid for test case comparison, according to the analysis presented in [61].

The data of the QPSK subcarriers are mapped from distinct decorrelated subsequences of a pseudo-random binary sequence (PRBS) with length $2^{23} - 1$. The order of independently modulated subcarrier allocation (*A, B, C, D*) is intentionally chosen to avoid possible inconsistency on the results obtained in the nonlinear transmission regime due to correlation imposed by even and odd (*A, B, A, B*) data allocation, as mentioned in [99].

After the power coupling stage in Fig. 4.1, the modulated subcarriers are sent to a polarization multiplexing emulation stage, to get the final DP-QPSK multicarrier system. The optical signal is amplified by a booster EDFA, forwarded to a variable optical attenuator and connected to the input of a recirculating loop. The passive structure of the recirculating loop is composed by two 50 km spans of SSMF, an optical bandpass filter, a 2-by-2 coupler and two acousto-optic switches. All fiber losses are compensated by distributed Raman amplification, performed with a backward pumping scheme per span (26 dBm@1450 nm). An EDFA is positioned inside the loop to compensate for the remaining losses.

At the output of the recirculating loop, the signal is pre-amplified, filtered to suppress out of band noise, and coherently detected with a single optical coherent receiver. The detected signal is sampled and acquired with a real-time sampling oscilloscope at 80 GSa/s and 33 GHz of analog bandwidth. Offline DSP is performed to demodulate the received subcarriers [73]. The flow of DSP algorithms is composed by full-field MC-DBP, resampling, subcarrier demultiplexing (downconversion and matched filtering), timing recovery, adaptive equalization with the constant modulus algorithm (CMA), carrier recovery, digital demodulation, and bit error counting.

Full-field MC-DBP is performed using a non-iterative symmetric SSFM to solve the Manakov approximation of the nonlinear Schrödinger equation (NLSE), with a fixed step size of 0.625 km (80 steps per 50 km span). Each

processed dataset had 10^6 signal samples, which allowed a minimum reliable bit-error rate (BER) counting of 10^{-4} per carrier (i.e., Q^2-factor of 11.4 dB), before hard-decision forward error correction (HD-FEC).

4.3   Results and discussions

The Q^2-factor calculated from the average BER of all carriers ($Q^2 = 20\log_{10}[\sqrt{2}\mathrm{erfcinv}(2.BER_{av})]$) is the figure of merit used to evaluate the performance. For the *error free* data sets, the Q^2-factor was estimated using the error vector magnitude (EVM) calculated from the error free received constellations (i.e. Q^2-factor values higher than 11.4 dB).

4.3.1   Back-to-back performance

In Fig. 4.3, the back-to-back performance is presented in Q^2-factor as a function of optical signal-to-noise ratio (OSNR) for the 4×8 GBd DP-QPSK multicarrier signal for both cases of interest.
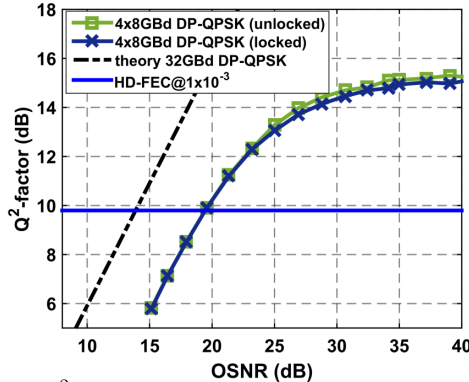
Figure 4.3 Back-to-back Q^2-factor performance of the two tested transmitter configurations. The OSNR is measured assuming a noise bandwidth of 0.1 nm.

Similar performance is obtained for frequency-locked (Case 1) and frequency-unlocked (Case 2) carriers transmitters. An implementation penalty of 5 dB compared with the theoretical curve is noticed. This penalty is mainly due to the impact of imperfect IQ imbalance calibration and the peak-to-average power ratio (PAPR) of the baseband signal [100]. Two factors contribute to increasing the PAPR of the signal delivered by the AWG: multicarrier generation and low roll-off RRC filtering. However, since both cases presented negligible differences in the back-to-back characteri-

zation, the performance after transmission can be compared on a common
basis.

4.3.2 MC-DBP Q^2-factor gain analysis

The density plots in Fig. 4.4 quantify the performance gains obtained after
MC-DBP for different transmission distances and fiber input powers for the
two tested cases. For a given input power, the gain is calculated with
respect to the Q^2-factor measured after applying only frequency domain
electronic compensation of chromatic dispersion (EDC).
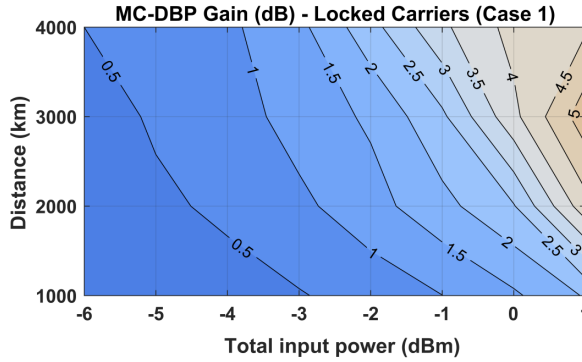
(a)
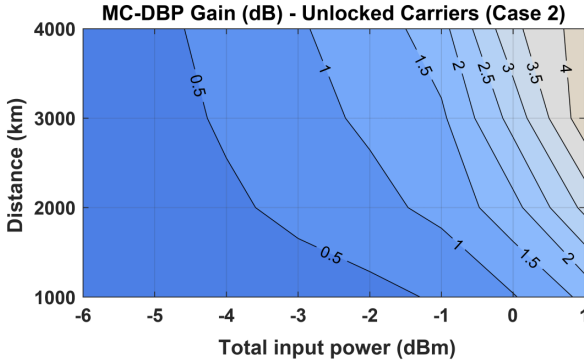
(b)

Figure 4.4 Density plot of the Q^2-factor gain, in dB, provided by MC-DBP for the two cases
under study. The gain is evaluated as a function of transmission distance and fiber input
power. (a) Frequency-locked system (Case 1); (b) Frequency-unlocked system (Case 2).

Comparing Fig. 4.4 (a) with Fig. 4.4 (b) it can be noticed that higher

Q^2-factor gain values tend to be obtained by MC-DBP in Case 1. This trend is particularly clear at 4000 km, the maximum distance investigated in the experiment.

Therefore, we conclude that frequency-referenced transmission is beneficial to the performance gain provided by full-field MC-DBP. Such performance advantage is mostly identified when the launch power is increased towards the nonlinear transmission regime.

4.3.3 Performance after 4000 km of transmission

Figure 4.5 details the Q^2-factor performance after 4000 km of transmission as a function of the total launch power into the fiber for both tested cases. Each Q^2-factor curve obtained correspond to one of the three distinct signal processing algorithms considered: EDC, SC-DBP, and MC-DBP.

Comparing the EDC results in Fig. 4.5 (a) and Fig. 4.5 (b) it can be noticed that both cases exhibits similar performance at -3 dBm of launch power. For power levels above -3 dBm, Case 2 tends to show better performance than Case 1, and the opposite happening for powers below -3 dBm.

Additionally, the optimal launch power value for Case 1 is -6 dBm, which is 2 dB lower compared to the optimal in Case 2, -4 dBm. These results show that the performance of the frequency-locked system decays faster than the performance of the frequency-unlocked in the nonlinear regime. In other words, frequency locking seems to enhance the impact of NLI in the nonlinear regime. However, the curves also show a better performance of MC-DBP in Case 1 in comparison with Case 2.

According to what is discussed in [61], due to a higher level of coherence of the carriers in Case 1 compared to Case 2, a larger fraction of deterministic NLI is produced, which can be compensated by MC-DBP. The Q^2-factor performances of SC-DBP are quite close in both Case 1 and Case 2, although the gain obtained in the nonlinear regime is still slightly better in Case 1. Overall, the maximum Q^2-factor obtained after MC-DBP in Case 1 overtakes the maximum in Case 2 by 0.6 dB.

4.3.4 Additional comments

As it is characteristic of Kerr nonlinearities, dependencies on frequency spacing, modulation format and symbol rate of the carriers may also have an influence on the system performance. Those degrees of freedom were not explored in this work. Since the experimental setup did not cover bandwidths as broad as the ones of typical WDM systems, it is not possible to

generalize quantitatively the results obtained for larger numbers of carriers. However, qualitatively the experimental results clearly point out that the level of coherence of the WDM carriers affects the characteristics of the NLI present in the system, with consequences for the performance of NLC by DBP.
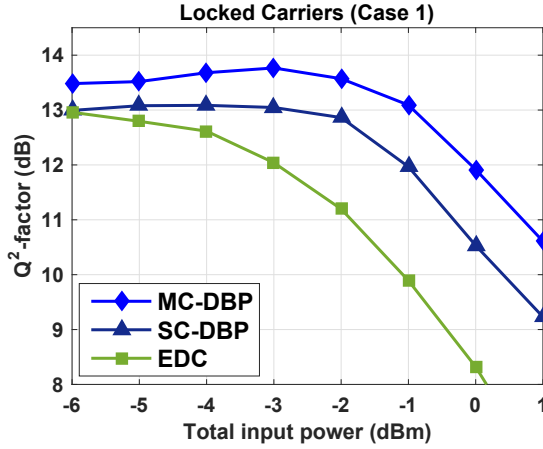
(a)
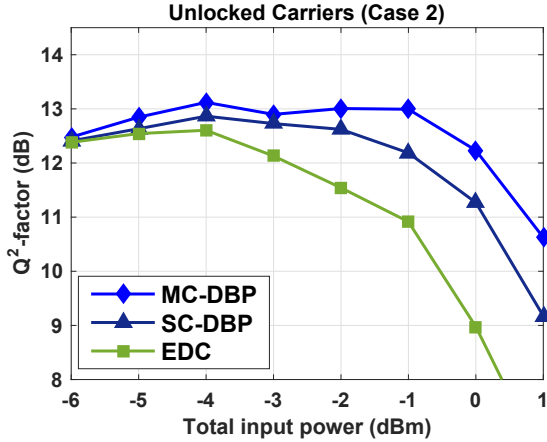
(b)

Figure 4.5 Q^2-factor performance after 4000 km of transmission distance for the two cases of interest (a) Frequency-locked carriers (Case 1); (b) Non frequency-referenced case (Case 2). In each case, the three curves indicate the performance obtained by applying EDC, SC-DBP and MC-DBP.

4.4 Summary

In this chapter, the impact of frequency-referenced transmission on the performance of receiver-side full-field MC-DBP for dual polarization systems was investigated. The analysis was centered on a comparative experimental study of long-haul multicarrier transmission, with and without frequency-locked carriers.

The results obtained with a 4×8 GBd DP-QPSK system have shown that the use of frequency-referenced transmission has an influence on the performance of receiver-side full-field MC-DBP. In particular, the performance of MC-DBP was improved when the transmitted carriers were locked in frequency. After 4000 km of transmission, the use of a frequency-referenced scheme has allowed an average improvement of 0.6 dB in the maximum Q^2-factor obtained after MC-DBP, compared with the case where the back-propagated carriers are not frequency-locked.

Chapter 5

Experimental study of probabilistic shaping versus DBP in WDM systems with DP-256QAM/1024QAM

The ultimate purpose of Kerr nonlinearity compensation is to enable higher throughput over the nonlinear fiber-optic channel by eliminating the deterministic fraction of the nonlinear interference (NLI) distorting the transmitted signals. More recently, constellation shaping has been proposed as an alternative to increasing the information rates. However, the second approach does not aim nonlinearity compensation (NLC), but a better exploitation of the channel given some constraints on its use.

From an information-theoretic point of view, the amount of information that can be reliably transferred from the input X to the output Y of given channel can be found from the mutual information (MI) between X and Y, $I(X;Y)$ [101]. The supremum of MI over all possible probability distributions of the input is the channel capacity C,

$$C = \sup_{p(X)} I(X;Y). \tag{5.1}$$

Uniformly distributed quadrature amplitude modulation (QAM) constellations are popular in coherent optical communications [62] due to its simplicity of implementation. However, for a fixed channel rule $p(Y|X)$, $I(X;Y)$ is a concave function of the input distribution $p(X)$ [101], i.e., it achieves a maximum value for some probability distribution of the input.

In general, the input distribution that maximizes MI may not be uniform. In this context, constellation shaping refers to the designing of the input distribution with the objective of approximating the distribution that maximizes MI under some given constraints. It is well known that for the power constrained additive white Gaussian noise (AWGN) channel such input distribution is a continuous Gaussian distribution, with variance dependent on the signal-to-noise ratio (SNR). The memory and the nonlinearity of fiber-optic channel, on the other hand, prevent it to be framed in a tractable channel rule. In particular, for this channel, $p(Y|X)$ is also a function of $p(X)$, and the evaluation or optimization of $I(X;Y)$ is a difficult task. Nonetheless, it is possible to calculate lower bound estimates of $I(X;Y)$ based on approximated channel models.

For uncompensated dispersion fiber transmission links, the NLI can be well modeled as an additive Gaussian noise [42]. This property allows the fiber-optic channel to be approximated by a memoryless AWGN channel. Therefore, constellation shaping strategies originally designed for the AWGN channel can be extended to the optical fiber. In this case, the aim of shaping is to increase the Gaussianity of the input distribution. Under those assumptions, geometric constellation shaping [9, 102–104] and probabilistic constellation shaping [105–110] have been proposed and investigated, numerically and experimentally, for the fiber-optic channel.

The statistical dependence of the inter-channel NLI on the modulation formats of the interfering carriers has been considered to devise new shaping strategies specific for the nonlinear fiber channel [111]. Differently from the previously mentioned references, in [111] the rate gains are due to the mitigation of inter-channel NLI. An approach to performing shaping considering a limited window of symbols in the optimization process was recently proposed in [112]. This strategy aims to include the relevant temporal statistics of the nonlinear channel in the constellation design.

Through this chapter the results are presented in MI, which has been proposed as a reliable figure of merit to assess performances of coherent optical transmission systems using soft-decision forward error correction (FEC) with an ideal demmapper [113–115].

As an original contribution from this thesis, this chapter reports an experimental study conducted to investigate and compare the gains on achievable information rate (AIR) that may result from the application of each technique, as from the combination of both. To the best of our knowledge, this investigation was the first of its kind presented and, in particular, the first to consider such high-order QAM modulation formats. The content

presented here is an adaptation of the conference paper [C3].

The constellation shaping algorithms utilized here are detailed in [116].

5.1 Introduction

As the coherent optical transmission systems approach the estimated lower bounds of AIRs over single-mode fiber (SMF), further improvement in throughput comes with the cost of extra effort directed to the optimization of transmitters and receivers. This is the main driver for the investigation of probabilistic constellation shaping and NLC.

Although both strategies seek the similar results, the nature and complexity of implementation for each differ significantly. Probabilistic shaping algorithms are designed for specific modulation formats and usually require a particular rate adaptation method, which restricts flexibility. Such algorithms also require information from the channel, especially the SNR available at the receiver. On the other hand, digital backpropagation (DBP) is transparent regarding modulation format and any aspect related to channel coding or rate adaptation. This relative freedom comes with a higher requirement for sampling rates and digital signal processing (DSP) complexity. Moreover, DBP requires the knowledge of extra channel information, such as the physical parameters of the fiber and the amplification scheme. The gains obtained with DBP are affected by a set of system's variables, such as the number of co-propagating wavelength-division multiplexing (WDM) channels [117], whereas gains from probabilistic shaping are expected to be dependent mainly of the SNR. Therefore, the effective utilization of each technique will be unavoidably related to the underlying application scenario.

Since both approaches require additional complexity in the transceiver implementation, an important question yet to be clarified is how much benefit can be provided by each one, enabling a better perspective for further analysis of performance gain versus implementation complexity trade-offs. That is the motivation for the work presented in this chapter.

The WDM system under investigation is composed of five carriers modulated at 10 GBd with dual polarization 256QAM (DP-256QAM) and dual polarization 1024QAM (DP-1024QAM). Probabilistic shaping is applied for both modulation formats, targeting rates around 5 and 6 bits/QAM symbol. Due to receiver bandwidth limitations, only single-carrier digital backpropagation (SC-DBP) is considered as NLC technique. Transmission distances investigated range from metro- to long-haul distances

($\geq$ 1000 km), up to 1700 km.

The remaining of the chapter is divided as follows. In Section 5.2, the experimental setup is detailed. Section 5.3 discuss the method employed to estimate the AIR, which is the evaluated figure of merit. Section 5.4 presents and discuss the results obtained and its followed by a final section with a summary of the main conclusions.

5.2   Experimental setup

The experimental setup is depicted in Fig. 5.1. At the transmitter, of-fline DSP is used to generate the sequences of encoded data symbols for four distinct constellations: uniformly distributed 256QAM, probabilistically shaped 256QAM, uniformly distributed 1024QAM, and probabilistically shaped 1024QAM. The probabilistic shaping method applied is based on the dyadic approximations of the optimum symbol input distributions for a large QAM constellation [105,108].

The sequence of complex-valued symbols is upsampled and pulse shaped with a root-raised cosine filter having a roll-off factor of 0.5. Within the stream of data symbols, quadrature phase-shift keying (QPSK) pilot symbols
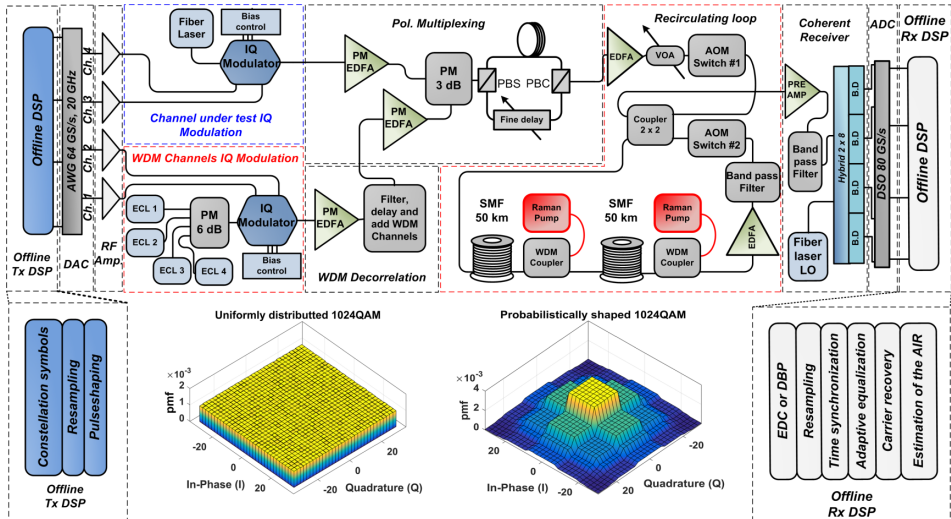
Figure 5.1 Experimental setup for WDM generation, transmission, coherent detection, and offline DSP processing of 5×10 GBd DP-256QAM/DP-1024QAM. At the center bottom, a two-dimensional density plot of the probability mass function of a uniform and a shaped 1024QAM constellation.

are inserted at a 2% rate to be used for adaptive equalization and carrier phase recovery. The data is digital-to-analog converted by a 64 GSa/s arbitrary waveform generator (AWG) with 20 GHz of bandwidth and amplified by radio frequency (RF) linear drivers. The baseband signal drives the optical in-phase/quadrature (IQ) modulators.

Two optical modulators are present in the setup. The first one modulates a sub-kHz linewidth fiber laser (Koheras BasiK C-15), which is used as the optical carrier for the channel under test (CUT). The second modulates the remaining four WDM carriers (external cavity laser (ECL)s, linewidth $\leq$ 100 kHz), which are subsequently split with a wavelength selective switch (WSS), decorrelated in time, and recombined with the CUT.

To measure the performance of each WDM channel, the central frequency of the fiber laser is systematically swapped in the 25 GHz frequency grid with the corresponding ECL of the channel to be assessed, such that the CUT is always measured with the same sub-kHz linewidth laser. This procedure is adopted to minimize the influence of the laser's phase noise in the measurements. The WDM channels are sent to the delay-and-add polarization multiplexing emulator stage which provides the dual-polarization signal.

The WDM transmission is performed in a recirculating loop composed by two 50 km spans of standard single-mode fiber (SSMF), an optical bandpass filter, a 2-by-2 coupler and two acousto-optic switches. All fiber losses are compensated by Raman amplification in backward pumping configuration (26 dBm@1450 nm). The remaining losses are compensated by an Erbium-doped fiber amplifier (EDFA). At the loop output, the signal is pre-amplified, filtered, and detected with an optical coherent receiver.

The local oscillator used by the coherent receiver is also a fiber laser with sub-kHz linewidth (Koheras BasiK E-15). The detected signal is acquired with a real-time sampling oscilloscope at 80 GSa/s and 33 GHz of bandwidth. The data is processed offline.

The flow of DSP algorithms is composed by low pass filtering, SC-DBP or electronic compensation of chromatic dispersion (EDC), resampling, timing recovery, pilot-assisted adaptive equalization with the constant modulus algorithm (CMA), carrier phase recovery [51], demodulation, and decoding.

The SC-DBP algorithm is performed using a non-iterative symmetric split-step Fourier method (SSFM) [118] to solve the Manakov approximation of the coupled mode nonlinear Schrödinger equation (NLSE) with a fixed step size.
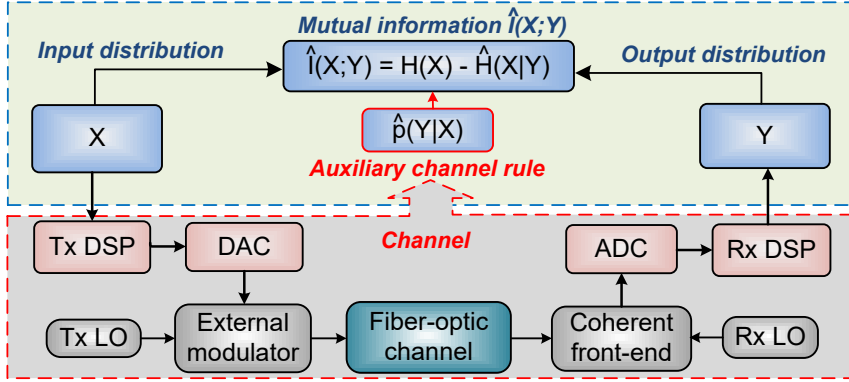
Figure 5.2 Block diagram illustrating the general procedure utilized for estimating the AIR estimation.

5.3   Estimation of the information rates

For all results presented in this chapter, the AIR is estimated after time synchronization, equalization, and carrier recovery. Figure 5.2 illustrates the process and variables involved in the AIR estimation.

The exact calculation of the MI $I(X;Y)$ between the input X and the output Y of the channel requires the conditional probability distribution $p(Y|X)$ to be known. Since the input-output relation of the fiber-optic channel is not available in a closed form, an auxiliary conditional probability distribution $\hat{p}(Y|X)$ is assumed. Because $\hat{p}(Y|X)$ is an approximation of the actual channel rule $p(Y|X)$, the MI $\hat{I}(X;Y)$ obtained with the auxiliary channel rule is a lower bound on the actual MI, i.e., $\hat{I}(X;Y) \leq I(X;Y)$. Moreover, since an optimum detection strategy is associated with the auxiliary channel model, $\hat{I}(X;Y)$ is said to be an AIR [119].

In the offline DSP applied to the received data, the Tikhonov distribution-based phase recovery algorithm proposed in [51] is used. This algorithm directly produces the posterior probability distributions $\hat{p}(X|Y)$, where X is a random variable describing the QAM symbols at the input of the channel and Y is the output of the adaptive equalizer. The AIR is then numerically estimated over long sequences of received data ($\geqslant 10^5$ QAM symbols per polarization) by calculating the mutual information

$$\hat{I}(X;Y) = H(X) - \hat{H}(X|Y),\tag{5.2}$$

where $H(X)$ is the entropy of the input distribution and $\hat{H}(X|Y)$ is the entropy of the posterior probability distribution.

The estimated AIRs are independent of the channel coding implementation, but a function of the channel and the signal processing at the receiver, including the EDC/DBP, synchronization, equalization and carrier phase recovery performed, and the input distribution.

5.4   Results and discussions

The results shown in this section corresponds to the performance of the system at the optimum *total* launched power which, for all tested configurations, was observed to be around -5 dBm without, and -3 dBm with DBP. Single channel DBP was applied using the largest step size in the SSFM, found to be 12.5 km (4 steps/span), that allowed the maximum improvement in AIR from the NLC.

Figure 5.3 shows the estimated AIR of the central WDM channel as a function of the transmission distance for all investigated configurations at the optimal launch power. The lowest AIR is exhibited by the uniform DP-256QAM without DBP, which achieves 5.2 bits/QAM symbol (104 Gb/s) at 1700 km of reach. For the same reach, the best performance is obtained for shaped DP-1024QAM with DBP - 5.9 bits/QAM symbol (118 Gb/s). The remaining cases, situated in between these two extremes, can be used to isolate the AIR gains provided by probabilistic shaping and DBP.
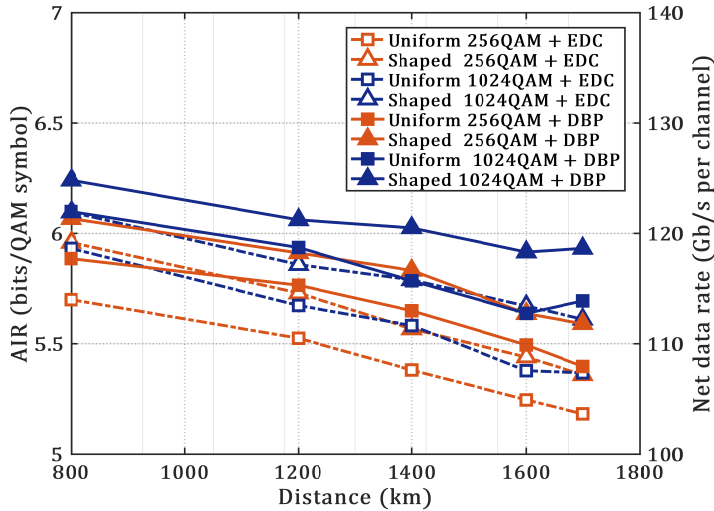
Figure 5.3 Estimated AIR of the central WDM channel versus distance for all investigated cases.

From the curves, it can be observed that uniform DP-256QAM with DBP, shaped DP-256QAM, and uniform DP-1024QAM present approximately the same AIR for all studied distances. The same conclusion follows from the configurations uniform DP-1024QAM with DBP, shaped DP-1024QAM, and shaped DP-256QAM with DBP.
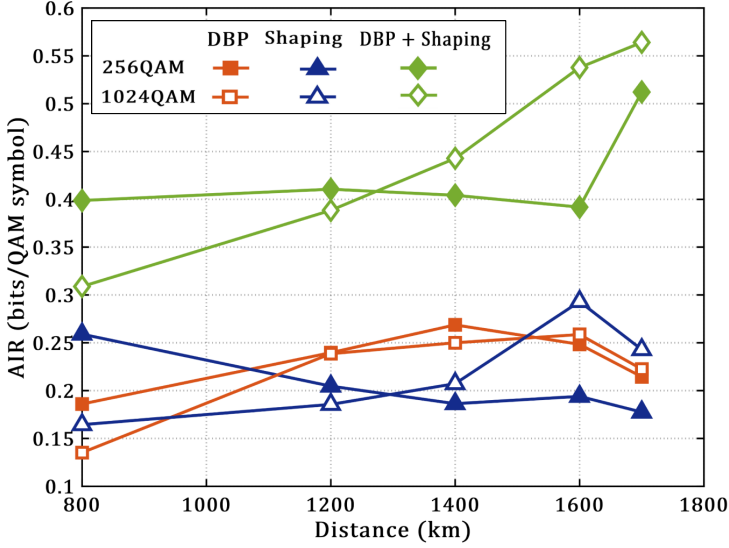
Figure 5.4 Gain in AIR of the central WDM channel compared to the uniform distributed constellation performance applying only EDC.

Figure 5.4 shows the AIR gains provided by probabilistic shaping, DBP and the combination of both in comparison with the transmission of the respective uniformly distributed constellation, as a function of the reach.

The first detail to be noticed is the consistency of the gains provided by DBP for both modulation formats. This behavior reflects the transparency of DBP concerning the modulation format. It is also verified that the probabilistic shaping gains vary with the distance. Such variation can be attributed to the mismatch between the channel parameters assumed in the numerical probabilistic optimization stage and the actual values in the experiment, as well imperfect signal processing and statistical variations due to the limited size of data sequences.

The similarity between the values of AIR gains from shaping and DBP is noticed. Moreover, the gain resulting from the joint application of both techniques is virtually equal to the sum of the gains obtained by applying
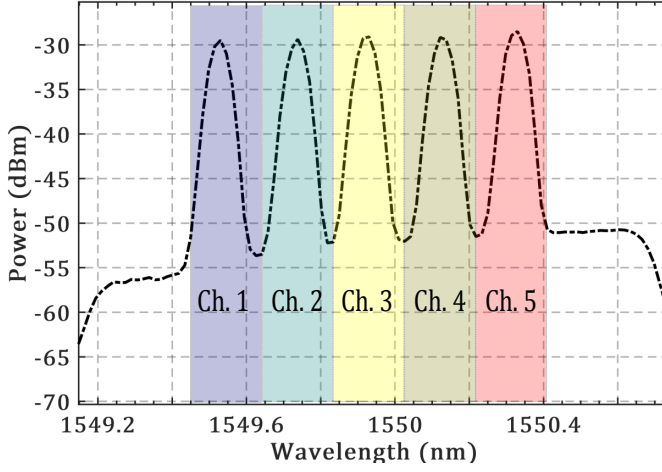
AIR in bits/QAM symbol

Channel #	1	2	3	4	5
Uniform 1024QAM	5.55	5.53	5.37	5.65	5.6
Shaped 1024QAM + DBP	6.06	5.93	5.93	5.99	5.79

Figure 5.5 Received spectrum and estimated AIR for all WDM channels for DP-1024QAM after 1700 km of transmission.

each technique separately. The maximum gain is verified to be between 0.5 to 0.6 bits/QAM symbol for shaped DP-1024QAM with DBP.

It is worth to mention that, for this experiment, the probabilistic optimization did not take into account the gain in SNR any other statistics that the receiver observes after DBP. However, in case this information is also included in the optimization process, it is likely that the gain obtained with the combination of both methods will surpass the sum of the gains observed when each technique is applied separately.

Figure 5.5 shows the spectrum and the estimated AIR for each of the five WDM channels after 1700 km of transmission distance of uniformly distributed DP-1024QAM and probabilistically shaped DP-1024QAM with DBP. Although there is a tilt in the noise spectrum, all inner channels reach quite similar performance. A small deviation can be noticed in AIR performance (see the table in Fig. 5.5) of the outer channels due to the fact those are the ones who mostly differ in the optical signal-to-noise ratio (OSNR). Nevertheless, the results demonstrate very similar performance gains for the

central channel and its WDM neighbors.

5.5   Summary

In this chapter, an experimental study comparing SC-DBP and probabilistic shaping was presented. The experimental results reported have shown that systems using DP-256QAM and DP-1024QAM modulation formats may have similar benefits in achievable information rates from probabilistic constellation shaping and DBP.

The independence of the performance gains from DBP, and probabilistic shaping allows them to add up, such that the overall benefit corresponds to the sum of the improvement achieved by each technique.

The use of both techniques has enabled a maximum improvement of 0.5 to 0.6 bits/QAM symbol, observed after 1700 km transmission of DP-1024QAM.

Part II

Spectral shaping

Chapter 6

Combined optical and electrical spectrum shaping for high baud rate Nyquist-WDM transceivers

The increase in the symbol rates of the optical transceivers has been a crucial enabler for the growth of the throughput rates in wavelength-division multiplexing (WDM) systems. Such importance is a consequence of the progress in building fast electronic devices and electro-optic interfaces. Moreover, constraints on power consumption, space, and cost of the transceivers have induced an effort to minimize the amount of their hardware parallelism [120].

However, for the next generations of WDM systems, operating at transmission rates of 400 Gb/s, 1 Tb/s and above, the spectral efficiency (SE) requirements establish challenges for the implementation of high symbol rate transceivers.

In this chapter, one aspect of the problem is investigated. The focus is on the conception of high symbol rate transceivers based on optical time-division multiplexing (OTDM). Particularly, the advantages and trade-offs of associating electrical and optical pulse shaping to minimize the spectral occupancy of OTDM signals are discussed.

The content of this chapter is based on the author's original publication [J5].

6.1 Introduction

Historically, the industry has adopted single-carrier based transceivers for optical WDM systems. Following this path, to attend with the future throughput requirements of WDM networks, single-carrier transceivers based on high serial interface rates and advanced modulation formats are needed.

Such architectures can be designed using different time-division multiplexing (TDM) signal generation techniques. In [121], experimental demonstrations of high baud rate transmission systems employing electrical time-division multiplexing (ETDM), quadrature phase-shift keying (QPSK) and quadrature amplitude modulation (QAM) are shown. Transmission of dual polarization quadrature phase-shift keying (DP-QPSK) and dual polarization 16QAM (DP-16QAM) at 107 GBd, and dual polarization 64QAM (DP-64QAM) at 72 GBd were demonstrated over dispersion uncompensated links. The all-ETDM generation of a single-carrier 90 GBd DP-64QAM has been demonstrated in [122]. However, when approaching such high ETDM rates (> 100 GBd), constraints on the bandwidth of the digital-to-analog converters (DACs) and electrical multiplexers impose challenges to increase the SE [123, 124]. For example, all-ETDM based transmission at high baud rates, in general, does not allow sophisticated pulse shaping to obtain low roll-off Nyquist modulated spectra, limiting SE.

Transmission at high symbol rates can also be achieved by performing TDM in the optical domain with the well known OTDM techniques [125]. Recent works using orthogonal time division multiplexing of optical Nyquist pulses (Nyquist-OTDM) have demonstrated the possibility to obtain single-carrier systems achieving both high symbol rate, and Nyquist modulated spectra [126].

However, similarly to conventional OTDM systems, Nyquist-OTDM requires complicated synchronization and demultiplexing schemes dependent of optical phase-locked loops and nonlinear optical signal processing. For those reasons, its application has traditionally been limited to dispersion compensated links. Additionally, after data modulation, Nyquist-OTDM suffers from limited suppression ratio of the spectrum sidebands, since the final roll-off of the modulated spectrum depends on the number of TDM stages employed [127]. Spectra with sharp roll-offs after modulation are approximated by increasing the number of TDM tributaries. The complexity of building an OTDM system with a large number of branches is generally not realistic, for a network transceiver. Furthermore, for a reduced number

of TDM stages, such technique may require guard bands between independent WDM channels [128]. Therefore, the SE will be reduced.

In the attempt to avoid the mentioned limitations of pure ETDM and OTDM approaches, hybrid signal generation techniques have been proposed and experimentally demonstrated.

In [129], a single channel, single polarization 125 GBd QPSK Nyquist-OTDM experiment employing full band signal coherent detection has been presented. Full field coherent detection enables the receiver to demodulate the OTDM data without any additional requirement on the synchronization between transmitter and receiver.

In [131, 132], sub-band synthesis is employed to generate single-carrier 124 GBd dual polarization 32QAM (DP-32QAM) and 128 GBd DP-16QAM, respectively, with low roll-off Nyquist spectral shaping. Hybrid techniques provide ways to explore the limits of each approach by splitting the overall signal generation complexity between electrical and optical domains.

This chapter addresses the content of [J5], where a hybrid approach for Nyquist-OTDM signal generation is proposed and experimentally demonstrated. The center idea is to ally optical generation of periodic sinc pulses and electrical pulse shaping to obtain Nyquist modulated spectra at high symbol rates (> 100 GBd), without the use of any extra optical filtering for side band suppressing. The experiment performed was the first to conceive a WDM Nyquist-OTDM signal generation based on a periodic train of sinc pulses. Straight line transmission of five 112.5 GBd Nyquist-OTDM DP-QPSK channels is demonstrated, up to 640 km dispersion uncompensated links, with full-field coherent detection at the receiver. After coherent detection, all steps necessary to estimate the received data are performed with digital signal processing (DSP), including clock recovery and time demultiplexing of the OTDM tributaries.

It is shown that such design strategy effectively improves the roll-off of the modulated OTDM signal, reducing the crosstalk penalty in baud-rate-spaced Nyquist-WDM systems.

The remaining of the chapter is divided as follows. Section 6.2 provides a detailed discussion on the variables that define the spectrum of Nyquist-OTDM signals. Section 6.3 shows analytical derivations explaining how optical and electrical pulse shaping techniques can be allied to minimize the spectral support of Nyquist-OTDM signals. Section 6.4 describes the experimental setup used to verify the analysis of Section 6.3. In Section 6.5, the experimental results are presents and discussed. The last section provides a summary of the conclusions.

6.2   Spectrum of Nyquist-OTDM signals

The Nyquist-OTDM techniques considered in this work are the ones based on the optical generation of periodic sinc pulses [127]. Such pulse trains can be orthogonally multiplexed in the time domain since they comply with the Nyquist criteria for zero intersymbol interference (ISI) [35].
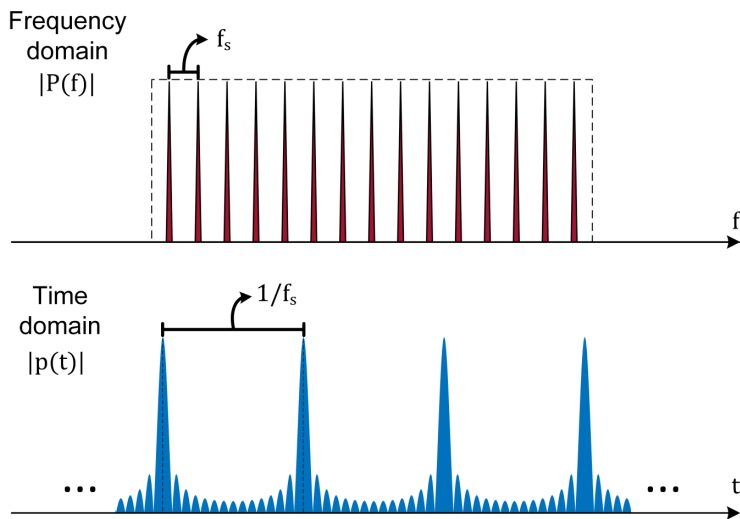
Figure 6.1 Duality between flat comb in frequency and periodic sinc pulse train in time.

A periodic train of sinc pulses in the time domain corresponds to a set of equidistant discrete tones, all with the same amplitude and with linear phase relationship, in the frequency domain mapped by the Fourier transform, as illustrated in Fig. 6.1. Such property allows one to obtain a periodic train of optical sinc pulses by designing the correspondent optical frequency comb.

The frequency comb can be primarily seen as the sampled version of a rectangular spectrum. As the frequency sampling resolution improves, i.e., the number of frequency tones within the rectangle bandwidth increases, the repetition rate of sinc pulses reduces and each pulse resembles better an ideal isolated sinc. The rectangle width defines the maximum serial baud rate that can be obtained after OTDM.

A model of a Nyquist-OTDM transmitter is shown in Fig. 6.2. Trains of
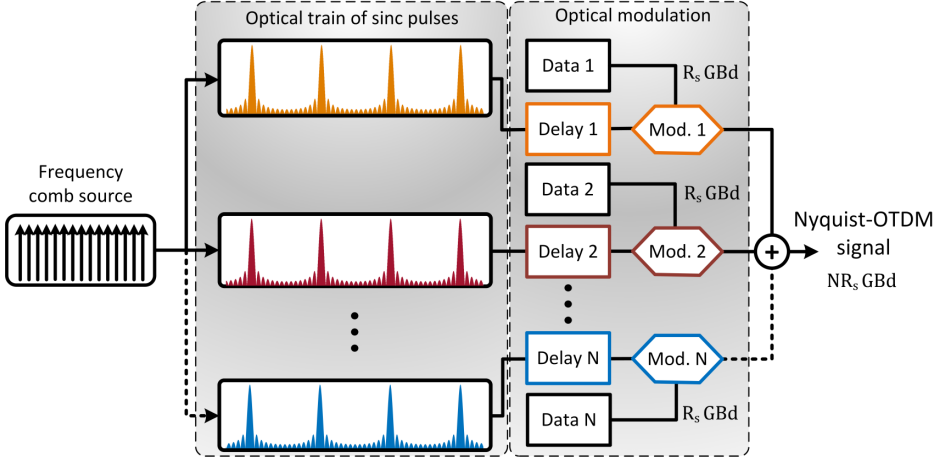
Figure 6.2 Diagram of a Nyquist-OTDM transmitter based on trains of periodic optical sinc pulses generated by a optical frequency comb.

periodic optical sinc pulses are obtained from an optical frequency comb. Each train delayed and modulated by an independent optical modulator. The delays are such that the peaks of a given sinc train will be aligned with a zero-crossing instant of all remaining pulse trains.

The N-parallel OTDM tributaries are obtained after independent modulation of each pulse train. The symbol rate of the modulation (R_s) corresponds to the frequency separation (f_s) of adjacent lines in the frequency comb. The last stage is the sum of all modulated tributaries to obtain the final OTDM signal with symbol rate NR_s.

Design trade-offs of optical pulse shaping

The repetition rate of the sinc pulses is the base rate for TDM. The linear in-phase/quadrature (IQ) modulation is commonly performed with standard square non-return-to-zero (NRZ) electrical pulse shape. The modulation stage does not affect the position of the zero crossings of the optical pulses in consecutive TDM slots.

However, modulated trains of sinc pulses are no longer deterministic, but cyclostationary random processes (see Section 2.2). After modulation, the power spectrum density (PSD) of the OTDM signal will be broader than the rectangular spectral window sampled by the frequency comb. This broadening occurs because the PSD of the process is dependent on the shape of the truncated sinc pulse modulated at each symbol period. Hence,

the roll-off factor of the modulated spectra will depend on the quality of the approximation of an infinite sinc obtained with the truncated pulse within each TDM slot. Specifically, the sampling resolution of the rectangular spectrum approximated by the frequency comb defines the fidelity of an isolated sinc pulse in time, which determines the final roll-off of the modulated spectrum. Therefore, with respect to the periodic optical pulses generation scheme, the use of frequency combs with a large number of tones is necessary to obtain PSDs with small roll-offs [129].

As stated in [127], such spectral broadening theoretically does not prevent WDM channels to be baud-rate-spaced without introducing crosstalk penalties. However, as a necessary condition to build such system, all WDM channels must be locked in frequency and phase, which is hard to accomplish in practical WDM architectures. Moreover, in real optical comb generation schemes, complete suppression of side band harmonics usually can not be achieved. Hence, such imperfections will also contribute to the spectral broadening after modulation. In practice, guard bands would be required to avoid performance degradation due to crosstalk between WDM channels.

Therefore, the spectral broadening caused by data modulation establishes a trade-off between SE and system complexity. A low repetition rate is required for the sinc pulse train, to minimize the roll-off factor of the final modulated spectrum and maximize the SE. Hence, a significant number of parallel TDM branches is needed, increasing the complexity of the transmitter.

Furthermore, increasing the number of comb tones will quickly increase the peak power values of the sinc pulses, which may bring additional practical problems. On the other hand, increasing the repetition rate of the pulses to use a reduced number of TDM stages will result in a poor spectrum roll-off after modulation. Therefore, it would be beneficial to find a strategy where low roll-off factor Nyquist-OTDM modulated spectra can be generated using a reduced number of TDM stages, i.e., employing frequency combs with a small number of frequency tones.

6.3   Combining optical and electrical spectrum shaping

To avoid the complexity versus spectral confinement trade-offs explained in Section 6.2, a hybrid approach based on the combined effect of optical and electrical spectrum shaping is proposed. In the following, a detailed analysis

is conducted to clarify the role of optical and electrical pulse shaping in the spectrum of a Nyquist-OTDM signal.

A known result from the Fourier analysis of periodic functions establishes that the inverse Fourier transform of an infinite periodic sequence of impulses in the frequency domain $P(f)$, with period f_s, corresponds to an infinite periodic sequence of impulses in time domain $p(t)$, with period $T_s = \frac{1}{f_s}$. This duality can be expressed as

$$P(f) = \frac{1}{T_s} \sum_{n=-\infty}^{\infty} \delta(f - nf_s) \iff p(t) = \sum_{n=-\infty}^{\infty} \delta(t - nT_s), \qquad (6.1)$$

where n is an integer number.

Consider $P_N(f)$ to be a finite window of N frequency tones centered around the zero frequency. Assume that N is an odd number for simplicity. To extract $P_N(f)$ from the infinite sequence $P(f)$, we define a rectangular window $R(f)$ in frequency domain and its correspondent inverse Fourier function in time

$$R(f) = \begin{cases} 1, & |f| \leq \frac{Nf_s}{2} \\ 0, & |f| \geq \frac{Nf_s}{2} \end{cases} \iff r(t) = N \operatorname{sinc}(Nf_s t), \qquad (6.2)$$

where $\operatorname{sinc}(x) = \sin(\pi x)/\pi x$.
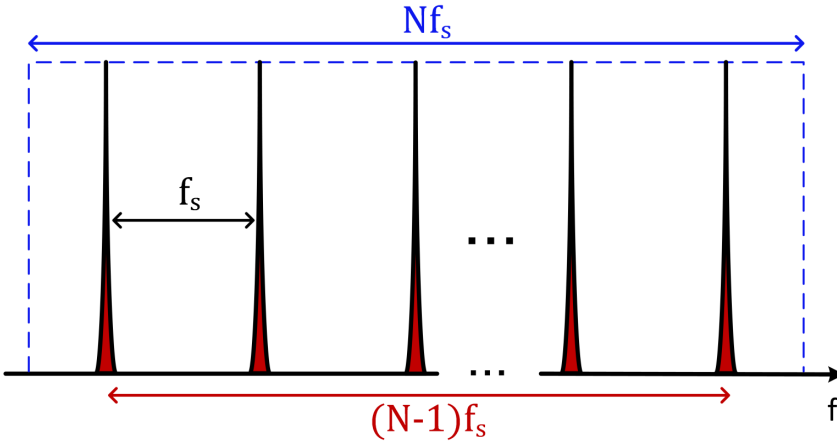
Figure 6.3 Illustration of an ideal frequency comb with N tones spaced by f_s Hz, resembling a sampled rectangular spectrum with bandwidth Nf_s Hz.

Therefore, using the equivalence between convolution in the time domain and multiplication in the frequency domain, it follows that

$$P_N(f) = R(f)P(f) \Longleftrightarrow p_N(t) = r(t) * p(t), \tag{6.3}$$

$$p_N(t) = N \operatorname{sinc}(Nf_s t) * \sum_{n=-\infty}^{\infty} \delta(t - nT_s), \tag{6.4}$$

$$p_N(t) = \sum_{n=-\infty}^{\infty} N \operatorname{sinc}[Nf_s(t - nT_s)]. \tag{6.5}$$

If the bandwidth of the rectangular window is fixed to $B = Nf_s$, then $N = B/f_s$ (see Fig. 6.3). Replacing it in Eq. (6.5), we have

$$p_N(t) = \sum_{n=-\infty}^{\infty} \frac{B}{f_s} \operatorname{sinc}\left[\frac{B}{f_s}\left(\frac{t}{T_s} - n\right)\right]. \tag{6.6}$$

Equation (6.6) represents a periodic train of sinc pulses in the time domain, generated by a comb with $N = B/f_s$ frequency components. The repetition rate of consecutive sinc pulses is equal to f_s, and the number of zero crossings between two consecutive pulse peaks is given by N.

An equivalent expression considering an even number of comb lines can be obtained by using the same steps. To simplify the calculations using properties of the Fourier transform, $P(f)$ should be shifted by $f_s/2$ to have both impulse train and rectangular window symmetric around $f = 0$. This operation does not affect the generality of the result. We then have

$$P_N(f) = R(f)P(f - f_s/2) \Longleftrightarrow p_N(t) = r(t) * p(t)e^{j\pi f_s t}, \tag{6.7}$$

$$p_N(t) = N \operatorname{sinc}(Nf_s t) * \sum_{n=-\infty}^{\infty} e^{j\pi f_s t} \delta(t - nT_s), \tag{6.8}$$

$$p_N(t) = \sum_{n=-\infty}^{\infty} e^{j\pi n} N \operatorname{sinc}[Nf_s(t - nT_s)], \tag{6.9}$$

$$p_N(t) = \sum_{n=-\infty}^{\infty} (-1)^n \frac{B}{f_s} \operatorname{sinc}\left[\frac{B}{f_s}\left(\frac{t}{T_s} - n\right)\right]. \tag{6.10}$$

A general expression for both cases is given by

$$p_N(t) = \sum_{n=-\infty}^{\infty} (-1)^{(B/f_s - 1)n} \frac{B}{f_s} \operatorname{sinc}\left[\frac{B}{f_s}\left(\frac{t}{T_s} - n\right)\right]. \tag{6.11}$$

Consider the case where the optical pulse train is modulated by applying a linear memoryless M-ary modulation format with unitary average symbol energy. Assuming an electrical pulse shape $g(t)$, with Fourier transform $G(f)$, the equivalent low-pass complex-valued modulated signal $s(t)$ and its corresponding PSD $\Phi_s(f)$ will be given, respectively, by

$$s(t) = \sum_{k=-\infty}^{\infty} s_k g(t - kT_s) p_N(t), \qquad (6.12)$$

$$\Phi_s(f) = \frac{1}{T_s} |G(f) * P_N(f)|^2, \qquad (6.13)$$

where s_k represent the symbol transmitted at the $t = kT_s$ instant. Figure 6.4 shows an example of how the waveforms in Eq. (6.12) may look like in time domain.
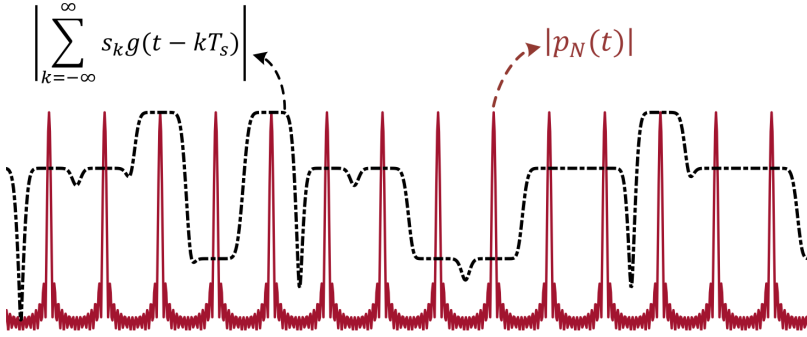
Figure 6.4 Example of the waveforms included in Eq. (6.12) (absolute values). The dashed line exemplifies a baseband electrical modulated waveform. The continuous line corresponds to a train of optical sinc pulses.

From Eq. (6.13) we can easily see that the final bandwidth of the modulated signal (B_S) will be given by the sum of bandwidth of the optical comb (B_{P_N}) with the bandwidth of the electrical pulse (B_G). As depicted in Fig. 6.3, we have $B_{P_N} = (N-1)f_s$. It follows that

$$B_S = (N-1)f_s + B_G \geq B = Nf_s, \qquad (6.14)$$

where the equality holds at the Nyquist limit. Therefore, in the Nyquist limit, $B_G = f_s$. Since $G(f)$ is independent of N, the same applies to the final roll-off of the modulated spectrum. Additionally, it is shown that it is possible to obtain low roll-offs for Nyquist-OTDM signals even when N is a small number.
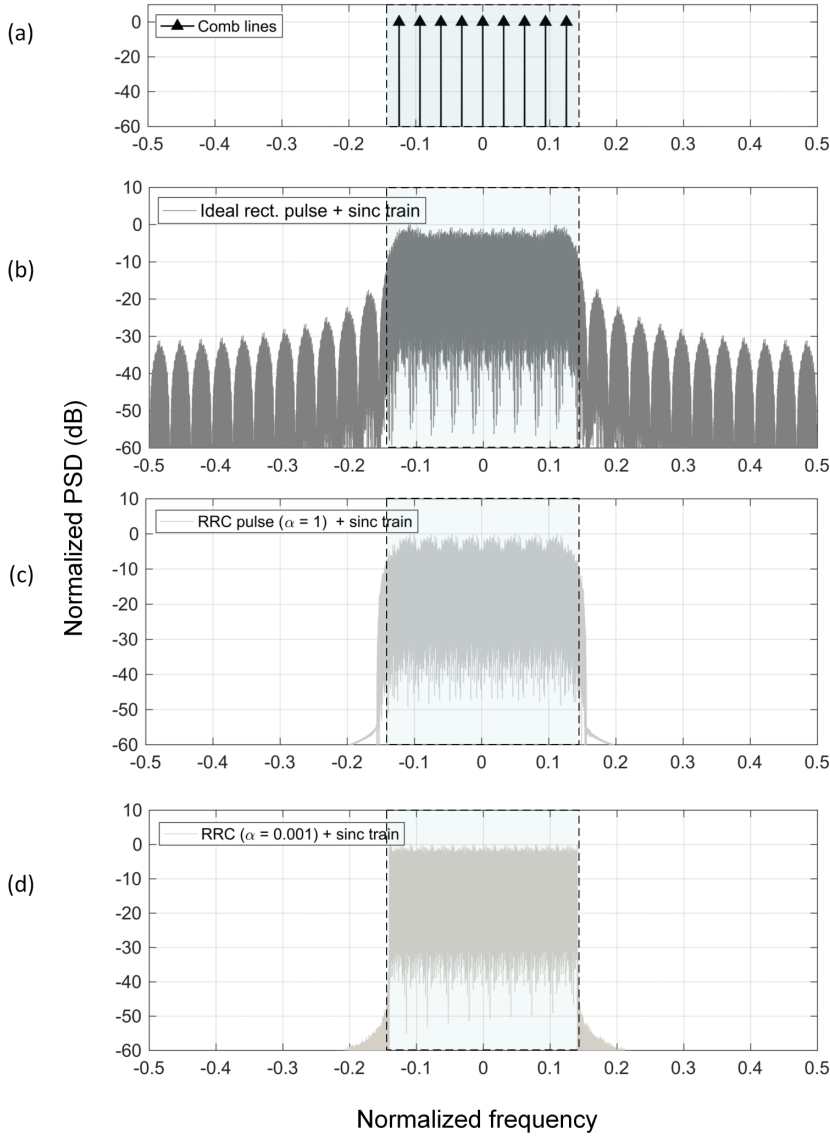
Figure 6.5 Numerical comparison of Nyquist-OTDM spectra obtained with an ideal optical comb source with nine frequency tones, modulated with different electrical pulse shaping. (a) Frequency comb lines; (b) Ideal NRZ rectangular pulse; (c) RRC with roll-off $\alpha = 1$; (d) RRC with roll-off $\alpha = 0.001$. The advantage of RRC over NRZ is clear in terms of sidelobes supression.

Therefore, to approach the Nyquist limit, the electrical pulse shape $g(t)$ can be selected from a family of pulses with narrow spectra, such as raised cosine (RC) or RRC pulses. For the analysis presented here, the RRC pulse shapes were chosen, due to its common use in communications.

The replacement of the electrical square NRZ pulse shape by the RRC shape allows one to control the roll-off factor of the resultant modulated spectrum, independently of how many TDM stages compose the OTDM signal. The RRC pulse shaping is implemented with finite impulse response (FIR) filters in the digital domain, and DACs. The effect of this change on the OTDM modulated spectrum is shown in Fig. 6.5.

Since the pulse shaping is performed with DSP, the FIR filters can be designed with a long window of symbols. Hence, the roll-off factor will not be limited by the shape of the optical truncated sinc pulses. Therefore, performing spectrum shaping on the electrical signals before optical modulation improves the spectral confinement of the final Nyquist-OTDM signals.

To experimentally verify the benefits of this approach, the setup described in Section 6.4 is built.

6.4 Experimental setup

The experimental setup is shown in Fig. 6.6. We should point first that, due to practical convenience to generate a WDM system, the sinc pulse generator was positioned after the data modulation. In this case, the periodic sinc generation acts as a pulse carver. However, it can be shown that the mathematical operations describing pulse carving and modulation commute, so the order in which the two are carried out has no impact on the final result (Section 6.3, Eq. (6.12) and (6.13)).

At the transmitter side, an arbitrary waveform generator (AWG) with 64 GSa/s and 20 GHz bandwidth was used to generate either 7 or 12.5 GBd QPSK modulated signals, to obtain the symbol rates of 63 and 112.5 GBd, respectively, after OTDM. To perform pulse shaping on the baseband signal generated by the AWG, a RRC digital filter was used. The filter was configured to provide the roll-off values (α) of 0.01, 0.2, 0.5 or 1 for the baseband spectrum. The electrical signal was then amplified to drive an optical IQ modulator. The optical input to the modulator was provided by an array of free-running continuous wave (CW) external cavity lasers (ECLs) with 100 kHz linewidth.

For the single-channel characterization, one laser centered at 193.4 THz

was used, while for the WDM case, five lasers centered at 192.625 THz, with
spacing varied between 100 and 200 GHz in steps of 12.5 GHz, were used.
The modulated signal was then sent to the Nyquist pulse carver (cf. eye
diagram inset in Fig. 6.6). Both Mach-Zehnder modulators (MZMs) were
driven by two RF sources synchronized with a 10 MHz reference clock. The
second MZM was driven by a sinusoidal clock generated by the AWG at a fre-
quency equal to the base symbol rate, i.e., 7 or 12.5 GHz and the first MZM
with the triple of the respective frequency, i.e., 21 or 37.5 GHz. An auto-
matic bias control for MZMs enabled stability and flatness of the frequency
tones. Nine spectral lines composed the comb, resulting in a sinc pulse
repetition after each nine consecutive zero crossings in the time domain.
Therefore, such configuration provided nine-time multiplexing slots, allow-
ing Nyquist-OTDM maximum aggregated serial rates of 63 and 112.5 GBd
per channel.

This signal was then fed to a three-stage OTDM multiplexer, where at
each stage the signal was split, delayed and recombined. Since the multi-
plexer was only able to fill 8 TDM slots, one slot was left empty. Therefore,
the effective transmission rates in Gb/s for the 63 GBd and 112.5 GBd test
cases were 224 Gb/s and 400 Gb/s per channel, respectively. However, the
spectral width of both modulated signals is not affected by the empty slot,
hence corresponding to 63 GHz and 112.5 GHz in the Nyquist limit (see
Section 6.3).

For the WDM transmission, the signal passed through a flex-grid inter-
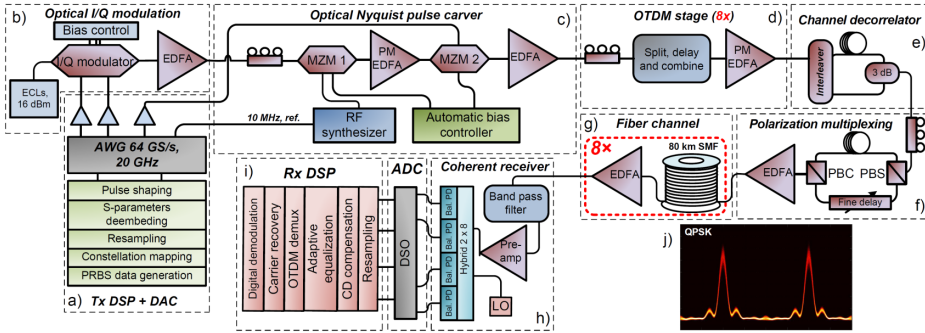
Figure 6.6 Experimental setup used to generate five 112.5 GBd DP-QPSK Nyquist-OTDM
channels. (a) Transmitter DSP, ADC conversion and linear electrical amplification (b)
Optical I/Q modulation (c) Periodic sinc pulse carving (d) Delay and add OTDM emula-
tion (e) Decorrelation of WDM channels (f) Polarization multiplexing emulation stage (g)
Straight line fiber channel with EDFA only amplification (h) Coherent receiver frontend
(i) Receiver's offline DSP (j) QPSK eye diagram of the signal before the OTDM stage.

leaver, to decorrelate WDM channels after modulation with a single modulator. The OTDM signal was then passed to the polarization multiplexer, where it was combined with its delayed copy in the orthogonal polarization.

For the experiment with fiber transmission, the signal was sent to a straight line fiber link composed of up to eight spans, each with 80 km of standard single-mode fiber (SSMF) and an Erbium-doped fiber amplifier (EDFA) compensating for the fiber losses. The launch power was kept at 0 dBm per channel.

After passing through the fiber link, the signal was pre-amplified, sent to a 0.9 nm optical bandpass filter and detected by a 40 GHz coherent receiver, using an ECL with a 100 kHz linewidth as a local oscillator. A real-time sampling oscilloscope with 33/63 GHz analog bandwidth per channel and sampling rate of 80/160 GSa/s was used to sample the 63/112.5 GBd signals. As only two 63 GHz inputs were available in the oscilloscope, only one polarization of the 112.5 GBd signal was digitized at the receiver, and the incoming signal was appropriately aligned by a polarization controller.

A set of coherent DSP algorithms [73], consisting of resampling, chromatic dispersion compensation, timing recovery, polarization demultiplexing and equalization, digital demultiplexing of the OTDM tributaries, and carrier frequency and phase recovery with an extended Kalman filter [133] was used to perform signal demodulation.

6.5 Results and discussions

Figure 6.7 shows the single channel back-to-back performance for 63 and 112.5 GBd DP-QPSK, with implementation penalties of 2 dB for both cases, at the bit-error rate (BER) threshold of 3.8×10^{-3} for the 7% overhead hard forward error correction (FEC). The curves depicted represent a superposition of the average BER of each OTDM tributary. The BER values below 10^{-5} were estimated from error vector magnitude (EVM), calculated from the received constellation after carrier recovery.

The inset plot in Fig. 6.8 shows a magnified positive side of the single-carrier baseband spectrum, around the symbol rate boundary (56.25 GHz), for all investigated values of α. This plot shows how the spectrum confinement is improved as α decreases. Lowering α largely suppresses spectral leakage from neighboring WDM channels and thus reduces inter-channel crosstalk for baud rate spacing [128].

The main plot in Fig. 6.8 shows the performance penalty due to crosstalk on the central channel for different values of α of the electri-
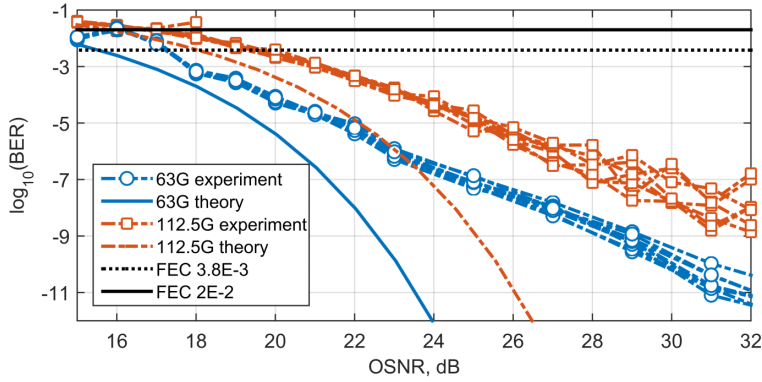
Figure 6.7 Back-to-back performance curves for 63 GBd and 112.5 GBd DP-QPSK.
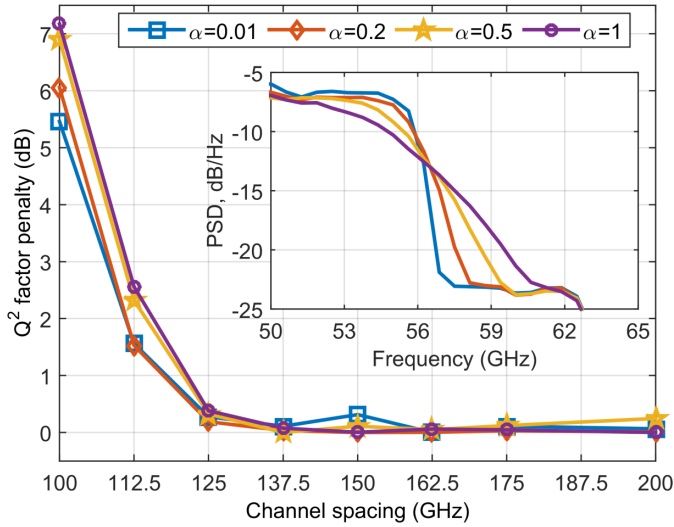
Figure 6.8 Crosstalk penalty on the central channel performance as a function of the carrier spacing for the back-to-back WDM configuration consisting of five 112.5 GBd DP-QPSK channels. The values for carrier spacing were chosen in agreement with the ITU flexigrid standard.

cal RRC shaping for 112.5 GBd DP-QPSK. For each α chosen, the penalty is calculated with respect to the best Q^2-factor obtained when the carriers are sufficiently spaced ($\geq$ 150 GHz) to disregard crosstalk penalties safely. It is shown that for channel spacing equal to the baud rate, lower values of α result in less crosstalk penalty. The minimum penalty at baud rate spacing is 1.5 dB, which is close to the optimum values reported in [134], obtained

for baud rate-spaced Nyquist-WDM systems based on digital filtering only.

A drawback of this technique is the fact that, when α is reduced, there is an increase of the peak-to-average power ratio (PAPR) on the AWG outputs [135], which leads to increased implementation penalty. Therefore, further investigation is needed to quantify the trade-off between crosstalk suppression and PAPR penalty.
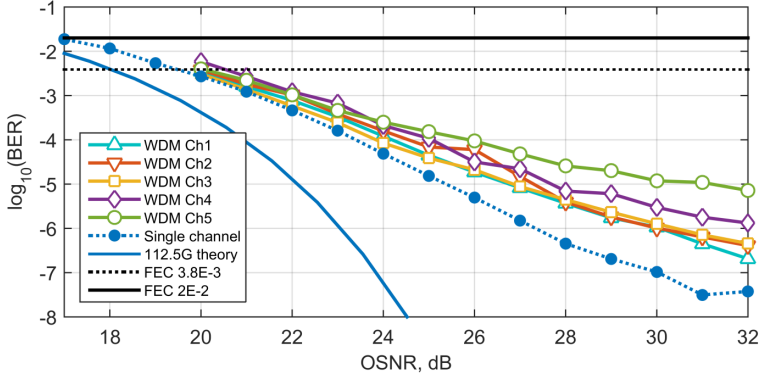
Figure 6.9 Back-to-back performance of all five channels for the WDM 112.5 GBd DP-QPSK configuration.
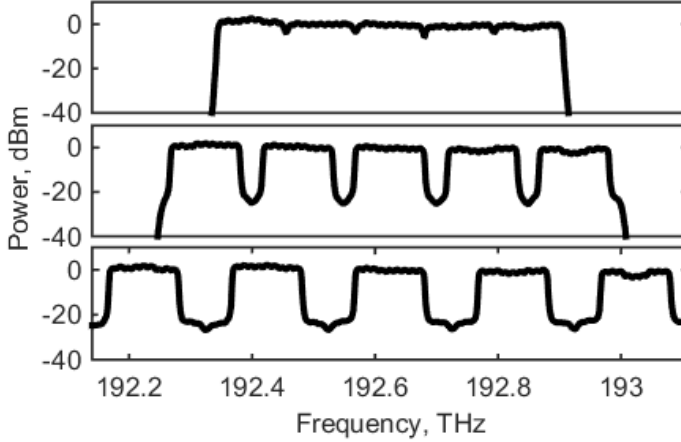
Figure 6.10 Spectrum of the modulated optical carriers for three different channel spacings (a) 112.5 GHz (baud rate spacing) (b) 125 GHz (c) 200 GHz.

Figure 6.9 shows the back-to-back BER performance for all WDM channels in comparison to the performance of a single channel. Each plotted
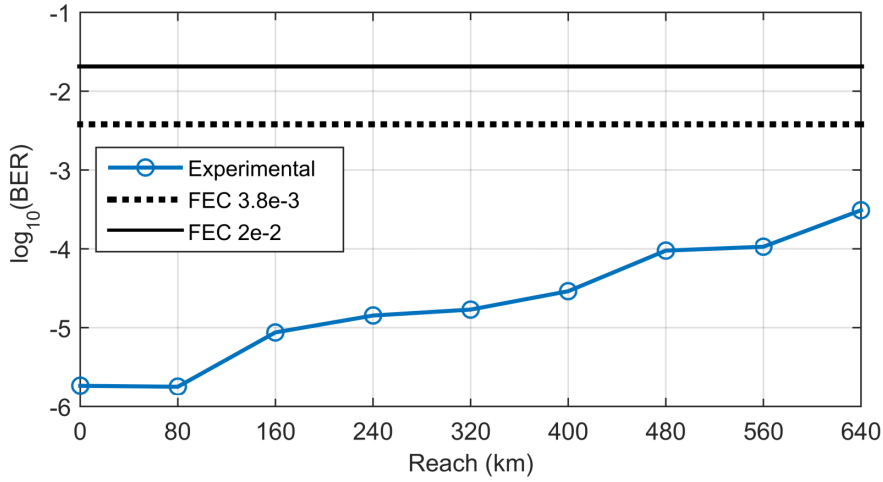
Figure 6.11 Transmission performance over straight line SSMF spans for the central channel in the WDM configuration. The indicated BER is the average value of all OTDM tributaries

value corresponds to average BER of all OTDM tributaries. A WDM implementation penalty of 2 dB for the best WDM channel is observed. Performance varies across different WDM channels due to non-flat noise floor at higher optical signal-to-noise ratios (OSNRs) as well as a slight dependence of the Nyquist carver modulators bias on the wavelength, leading to suboptimal Nyquist pulse generation for outer channels. This is also visible in Fig. 6.10, which depicts optical spectra for the WDM channel spacing of 112.5 GHz, 150 GHz, and 200 GHz. Particularly at a spacing of 200 GHz, this dependence can be easily observed in the uneven spectra of non-central WDM channels.

Figure 6.11 shows 5-channel WDM Nyquist-OTDM 112.5 GBd DP-QPSK back-to-back performance, with $\alpha = 1$ and channel grid spacing of 125 GHz. The grid spacing was set to 125 GHz, instead of 112.5 GHz, due to the limitations of the WaveShaper [72] used to emulate a WDM optical interleaver on the channel decorrelator (Fig. 6.6). Since it was not possible to create an attenuation profile to demultiplex and decorrelate even and odd channels at 112.5 GHz, the channel grid was to increased by 12.5 GHz, to maintain the agreement with the ITU flexigrid standard [136]. The choice of α was made to minimize a possible impact of PAPR on the transmission results.

Successful straight line transmission of the WDM signal was performed for up to 640 km of dispersion uncompensated fiber spans. The launched

power per channel was set to 0 dBm to guarantee linear regime of operation. The OSNR value of 23.2 dB per carrier was measured after 640 km of transmission. Similar performance was achieved after transmission and back-to-back at the same OSNR values, indicating that the linear fiber impairments were fully compensated after DSP. Additional investigation is required to evaluate optimum launch power per channel, which for this experiment was roughly estimated around 4 dBm, and the maximum transmission reach, which was limited by the amount of fiber available in straight line setup.

One should point that the performance results presented in Fig. 6.11 may be *underestimated* since only one polarization of the signal is being acquired and processed at the time. Better performances should be expected with the use of a complete dual polarization coherent receiver for the 112.5 GBd setup, which would allow optimal equalization of the polarization mixing effects. Additionally, the BER values obtained in a sub-optimal scenario are small enough to guarantee that the results can be reproduced with the complete dual polarization receiver.

6.6 Summary

In this chapter, it was shown that by combining the optical generation of periodic sinc pulses with electrical pulse shaping, the roll-off factor of the OTDM modulated spectrum can be reduced, independently of the number of optical comb lines used to generate the periodic train of sinc pulses. The proposed approach can balance the complexity of the transmitter between optical and electrical domains, enabling the generation of Nyquist modulated channels at symbol rates higher than 100 GBd, without the use of any bandpass optical filter for sidelobe suppression.

The benefits of this approach are experimentally quantified, showing that inter-channel crosstalk penalty can be reduced up to 1.5 dB at baud rate spacing of 112.5 GBd DP-QPSK channels. Additionally, based on this technique, we successfully demonstrated the first WDM generation and straight line dispersion uncompensated transmission of five 112.5 GBd DP-QPSK Nyquist-OTDM carriers over 640 km with full-field coherent detection at the receiver. It was shown that this approach can be suitable for designing small roll-off, high baud rate Nyquist-WDM transceivers. Further investigation is needed to quantify the impact of PAPR induced by the electrical pulse shaping and the performance for higher-order modulation formats.

Part III

Adaptive equalization

Chapter 7

Widely linear equalization for coherent optical receivers

Efficient and robust DSP equalization methods are necessary for coherent optical transceivers to compensate linear fiber impairments, such as chromatic dispersion (CD) and polarization mode dispersion (PMD) [137]. The design of such algorithms for coherent optical receivers has been mostly based on the physical models of the linear fiber effects. However, coherently detected signals can also be affected by imperfections present at the receiver or at the transmitter, which may result in a bad performance of the linear equalization.

This chapter presents one of the main contributions of this thesis. Here, the use of augmented complex-valued models, also known as widely linear (WL) complex-valued transformations, is proposed to define a general and systematic design for the equalizers used in coherent optical receivers. It is shown the usefulness of these models to design linear equalization structures that can take into account receiver front-end imperfections, such as in-phase/quadrature (IQ) imbalance and IQ skew, here generally referred to as IQ-mixing effects. Even though the analysis presented in this chapter is restricted to IQ-mixing happening at the receiver, the same procedure can be applied to the transmitter side, as exemplified in Chapter 8.

Complex-valued WL transformations have been extensively investigated in the digital signal processing (DSP) literature, particularly for statistical modeling and equalization problems. A comprehensive overview of this topic can be found in [145]. Examples of application of complex-valued WL equalization techniques can be consulted in e.g. [146–149]. The results presented in this chapter comprise the content of the work published by

the author in [J3].

7.1 Introduction

Usually, coherent optical receivers require two steps of linear equalization. In the first step, the accumulated CD is compensated by a zero-forcing (ZF) static equalizer. Zero-forcing equalization is performed when the channel frequency response $H(\omega)$ is compensated by directly applying its inverse $H(\omega)^{-1} = 1/H(\omega)$ to the detected signals at the receiver [138]. The channel response is assumed to be known at the receiver. As a drawback, the use of such equalizers may result in performance degradation for systems with frequency-selective channel characteristics, due to noise enhancement. Fortunately, CD has all-pass frequency response characteristic and its compensation by a static ZF equalizer is practically viable for coherent optical receivers [137]. In the second step, an adaptive equalizer is used to compensate the residual linear intersymbol interference (ISI) and to demultiplex polarizations.

Common sources of linear ISI are the frequency response of transmitter/receiver, reconfigurable optical add-drop multiplexer (ROADM) filtering, residual CD and polarization mixing, due solely to rotations of the state of polarization (SOP) or to PMD, which can be time-varying.

These two stages of equalization are enough to compensate the linear ISI originated in the fiber-optic channel. However, especially when such systems evolve to use high order modulation formats or high symbol rate signaling, imperfections at the receiver front-end may have considerable influence on the equalization performance. Transceivers employing large order M-ary quadrature amplitude modulation (QAM) formats usually require high signal-to-noise ratio (SNR) values for reliable transmission, which make their implementation less tolerant to receiver front-end imbalances. Therefore, two important problems in this scenario are how these imperfections relate to the performance of the signal detection and equalization, and how the DSP can be designed to mitigate eventual penalties.

Recent works have investigated adaptive equalization architectures robust to receiver front-end imperfections [139–142]. In [139], a complex-valued blind equalization structure is proposed to compensate IQ-mixing in dual polarization (DP) receivers, assuming the use of Nyquist filtering. Only back-to-back experimental performance evaluation is presented.

In [140], a real-valued least mean square (LMS) approach for IQ-mixing compensation is proposed and numerically validated. The ZF compensa-

tion of CD in the presence of IQ-mixing turned out to be problematic for the equalizers proposed in [139, 140]. In [141, 142], the authors suggest a modification on the ZF CD equalizer and propose a new complex-valued blind adaptive equalizer structure, to allow the compensation of IQ skew when the detected signals have large accumulated CD.

However, a detailed analysis of the connection between IQ-mixing effects and the complexity requirements for equalization algorithms at the optical coherent receiver was yet absent in the literature. For example, none of the mentioned references provides design rules specifying the required number of taps for the adaptive equalization algorithm. Mainly, the joint impact of ZF equalization of CD and IQ-mixing on the performance of the adaptive equalizer was not addressed.

In this chapter, it is demonstrated how WL complex-valued transformations can be used to derive analytical models to explain the interaction of ZF equalization of CD with the coherent receiver front-end imperfections. Based on such models, the complexity requirements for minimum mean square error (MMSE) equalization in the presence of IQ-mixing are extracted. Given the assumptions for the derivation of the models, it is shown that the general solution to the equalization problem corresponds to a WL complex-valued adaptive equalizer structure, which is proposed and validated with extensive numerical simulations.

The rest of this chapter is organized as follows. In Section 7.2, a formal description of the connection between linear real-valued and widely linear complex-valued transformations is presented. In Section 7.3, it is shown how IQ-mixing effects can be seen as complex-valued WL transformations. Next, it is shown that this approach leads to closed-form expressions that describe the resultant effect of IQ-mixing when the receiver performs ZF equalization of CD. Based on the obtained expressions, the complexity requirements are discussed for the adaptive equalizer to be able to recover the signals with no penalties coming from skew or imbalance at the receiver front-end.

In Section 7.4, the general structure of a WL complex-valued adaptive equalizer for a polarization multiplexed receiver is derived. In Section 7.5, extensive simulation results and discussions are presented, comparing the performance of the proposed equalizer with a standard linear complex-valued equalizer, which leads to the conclusions.

7.2   Augmented complex-valued signal processing

In order to start the analysis, some definitions will be necessary to formally establish equivalence relations between linear transformations in real vector spaces and complex vector spaces. Here we use the approach of [145]. Consider the vectors $\mathbf{u}_r \in \mathbb{R}^N$ and $\mathbf{u}_i \in \mathbb{R}^N$. With $\mathbf{u}_r$ and $\mathbf{u}_i$, three related column vectors can be constructed:

   I. The real composite vector: $\mathbf{u}_{\mathbb{R}} = \left[\mathbf{u}_r^T, \mathbf{u}_i^T\right]^T = \begin{bmatrix} \mathbf{u}_r \\ \mathbf{u}_i \end{bmatrix}$,

   II. The complex vector: $\mathbf{u} = \mathbf{u}_r + j\mathbf{u}_i$,

   III. The augmented complex vector: $\underline{\mathbf{u}} = \left[\mathbf{u}^T, \mathbf{u}^H\right]^T = \begin{bmatrix} \mathbf{u} \\ \mathbf{u}^* \end{bmatrix}$,

where $\mathbf{u}_{\mathbb{R}} \in \mathbb{R}^{2N}$, $\mathbf{u} \in \mathbb{C}^N$ and $\underline{\mathbf{u}} \in \mathbb{C}_*^{2N}$. The conjugate operation is denoted by $(\cdot)^*$, the transpose operation is denoted by $(\cdot)^T$, and the conjugate transpose (hermitian) is denoted by $(\cdot)^H$. The notation $\mathbb{C}_*^{2N}$ refers to the augmented version of the set $\mathbb{C}^{2N}$.

   The mapping between the complex augmented vector $\underline{\mathbf{u}}$ and the real composite vector $\mathbf{u}_{\mathbb{R}}$ is given by the linear real-to-complex transformation

$$\mathbf{T}_N = \begin{bmatrix} \mathbf{I} & j\mathbf{I} \\ \mathbf{I} & -j\mathbf{I} \end{bmatrix} \in \mathbb{C}^{2N \times 2N} \implies \underline{\mathbf{u}} = \mathbf{T}_N \mathbf{u}_{\mathbb{R}}, \tag{7.1}$$

where $\mathbf{T}_N$ has the property $\mathbf{T}_N \mathbf{T}_N^H = \mathbf{T}_N^H \mathbf{T}_N = 2\mathbf{I}$, i.e. $\frac{1}{\sqrt{2}}\mathbf{T}_N$ is a unitary matrix.

   Now suppose we apply an arbitrary linear transformation $\mathbf{M} : \mathbb{R}^{2N} \to \mathbb{R}^{2N}$ to the vector $\mathbf{u}_{\mathbb{R}}$

$$\mathbf{v}_{\mathbb{R}} = \mathbf{M}\mathbf{u}_{\mathbb{R}} \to \begin{bmatrix} \mathbf{v}_r \\ \mathbf{v}_i \end{bmatrix} = \begin{bmatrix} \mathbf{m}_{11} & \mathbf{m}_{12} \\ \mathbf{m}_{21} & \mathbf{m}_{22} \end{bmatrix} \begin{bmatrix} \mathbf{u}_r \\ \mathbf{u}_i \end{bmatrix}, \tag{7.2}$$

where $\mathbf{m}_{ij} \in \mathbb{R}^{N \times N}$. The transformation $\mathbf{M}$ is equivalent to a complex augmented transformation $\underline{\mathbf{H}} : \mathbb{C}_*^{2N} \to \mathbb{C}_*^{2N}$ which can be derived as follows

$$\begin{aligned} \mathbf{v}_{\mathbb{R}} &= \mathbf{M}\mathbf{u}_{\mathbb{R}} \Rightarrow \mathbf{T}_N \mathbf{v}_{\mathbb{R}} = \mathbf{T}_N \mathbf{M} \frac{1}{2} \mathbf{T}_N^H \mathbf{T}_N \mathbf{u}_{\mathbb{R}}, \\ \underline{\mathbf{v}} &= \frac{1}{2} \mathbf{T}_N \mathbf{M} \mathbf{T}_N^H \underline{\mathbf{u}} \Rightarrow \underline{\mathbf{v}} = \underline{\mathbf{H}}\,\underline{\mathbf{u}}, \end{aligned} \tag{7.3}$$

$$\underline{\mathbf{H}} = \frac{1}{2} \mathbf{T}_N \mathbf{M} \mathbf{T}_N^H, \tag{7.4}$$

where the matrix $\underline{\mathbf{H}} \in \mathbb{C}^{2N \times 2N}$ has the particular block pattern

$$\underline{\mathbf{H}} = \begin{bmatrix} \mathbf{H_1} & \mathbf{H_2} \\ \mathbf{H_2^*} & \mathbf{H_1^*}, \end{bmatrix} \tag{7.5}$$

with

$$\mathbf{H_1} = \frac{1}{2}[\mathbf{m}_{11} + \mathbf{m}_{22} + j(\mathbf{m}_{21} - \mathbf{m}_{12})], \tag{7.6}$$

$$\mathbf{H_2} = \frac{1}{2}[\mathbf{m}_{11} - \mathbf{m}_{22} + j(\mathbf{m}_{21} + \mathbf{m}_{12})]. \tag{7.7}$$

From $\underline{\mathbf{H}}$ and the definition of the augmented complex vectors $\underline{\mathbf{v}}$ and $\underline{\mathbf{u}}$, we can derive the general form of a *widely linear* transformation in $\mathbb{C}^N$

$$\mathbf{v} = \mathbf{H_1}\mathbf{u} + \mathbf{H_2}\mathbf{u}^*. \tag{7.8}$$

We denote by *strictly linear* transformation in $\mathbb{C}^N$ the particular case of Eq. (7.8) when $\mathbf{H_2} = 0$. Therefore, one can directly conclude that a linear transformation in $\mathbb{R}^{2N}$ can only be completely described by a strictly linear transformation in $\mathbb{C}^N$ if the condition $\mathbf{H_2} = 0$ is satisfied. From Eq. (7.7), this condition implies that $\mathbf{M}$ in Eq. (7.2) has to have the form

$$\mathbf{M} = \begin{bmatrix} \mathbf{m}_{11} & \mathbf{m}_{12} \\ -\mathbf{m}_{12} & \mathbf{m}_{11} \end{bmatrix}, \tag{7.9}$$

i.e., $\mathbf{M}$ has to be a skew-symmetric matrix: $\mathbf{M}^T = -\mathbf{M}$.

Most of the typical complex-valued DSP implementations of equalizers (static and adaptive) for coherent optical receivers adopt strictly linear structures since passive linear propagation effects happening into the fiber are completely described by strictly linear complex-valued models [143]. However, as it is shown in the next sections, Eq. (7.8) has implications on the equalization performance if additional effects that violate Eq. (7.9) are present between transmitter and receiver. In particular, the focus will be directed to equalization problem when the receiver front-end is subject to IQ imbalance or IQ skew.

7.3 Imbalanced receiver models

In this section, complex-valued analytical models of IQ imbalance and IQ skew effects at the receiver are derived. The models obtained apply to a single polarization receiver. Nevertheless, considering that CD and PMD are

strictly linear in the complex domain (i.e. when described in the complex domain, they satisfy the condition $\mathbf{H_2} = 0$), such models can be directly extended for a polarization multiplexed receiver. Although this fact will not be proved here, it can be verified following the analysis presented in [143].

No imbalance or skew is considered at the transmitter side. Frequency offset between transmitter and receiver is not included in the model derivations, although it is included in the simulation and results. Here the notations $\mathcal{F}\{.\}$ and $\mathcal{F}^{-1}\{.\}$ are used to denote the direct, and the inverse Fourier transforms operations, respectively. The notation of matrix multiplication, for the sake of clarity, is also extended to denote the convolution operation, as it is commonly used in the modeling of multiple-input multiple-output (MIMO) systems. The meaning should be clear from the context.

7.3.1 Receiver IQ imbalance model

Assuming the case where IQ imbalance is present only at the receiver side. We can model the IQ imbalance by re-writing the equivalent complex baseband of an ideal local oscillator (LO) laser as

$$
\begin{aligned}
m_{lo}^{\mathrm{rx}}(t) &= (1 - \epsilon_{\mathrm{rx}}) \cos(\omega_c t - \phi_{\mathrm{rx}}/2) \\
&\quad - j(1 + \epsilon_{\mathrm{rx}}) \sin(\omega_c t + \phi_{\mathrm{rx}}/2) \\
&= k_1 e^{-j\omega_c t} + k_2 e^{j\omega_c t},
\end{aligned}
\tag{7.10}
$$

with

$$
\begin{aligned}
k_1 &= [(1 - \epsilon_{\mathrm{rx}})e^{j\frac{\phi_{\mathrm{rx}}}{2}} + (1 + \epsilon_{\mathrm{rx}})e^{-j\frac{\phi_{\mathrm{rx}}}{2}}]/2 \\
&= \mathrm{k}_{1,r} + j\mathrm{k}_{1,i},
\end{aligned}
\tag{7.11}
$$

$$
\begin{aligned}
k_2 &= [(1 - \epsilon_{\mathrm{rx}})e^{-j\frac{\phi_{\mathrm{rx}}}{2}} - (1 + \epsilon_{\mathrm{rx}})e^{j\frac{\phi_{\mathrm{rx}}}{2}}]/2 \\
&= \mathrm{k}_{2,r} + j\mathrm{k}_{2,i},
\end{aligned}
\tag{7.12}
$$

where $\omega_c = 2\pi f_c$, and f_c is the carrier frequency. The parameters $\{\epsilon_{rx}, \phi_{rx}\}$ represent the effective amplitude and phase imbalance of the receiver, respectively [144]. Let $s(t) = s_I(t) + js_Q(t)$ be the equivalent complex baseband of the received signal at the instant t, then

$$
\hat{s}(t) = k_1 s(t) + k_2 s^*(t),
\tag{7.13}
$$

where $\hat{s}(t)$ is the resultant signal obtained after imbalanced detection of $s(t)$. Equation (7.13) can be rewritten in the real-valued matrix form

$$\begin{bmatrix} \hat{s}_I(t) \\ \hat{s}_Q(t) \end{bmatrix} = \begin{bmatrix} \mathrm{k}_{1,r} + \mathrm{k}_{2,r} & -(\mathrm{k}_{1,i} - \mathrm{k}_{2,i}) \\ \mathrm{k}_{1,i} + \mathrm{k}_{2,i} & \mathrm{k}_{1,r} - \mathrm{k}_{2,r} \end{bmatrix} \begin{bmatrix} s_I(t) \\ s_Q(t) \end{bmatrix} \Rightarrow$$

$$\begin{bmatrix} \hat{s}_I(t) \\ \hat{s}_Q(t) \end{bmatrix} = \begin{bmatrix} k_{11} & k_{12} \\ k_{21} & k_{22} \end{bmatrix} \begin{bmatrix} s_I(t) \\ s_Q(t) \end{bmatrix}. \tag{7.14}$$

Equation (7.14) is a linear transformation included in the set defined in Eq. (7.2). However, in the general case, it does not comply with the form of Eq. (7.9). Hence, IQ imbalance can only be completely described in the complex domain by a widely linear transformation.

7.3.2   Receiver IQ time skew model

Assuming that the IQ components of the received signal $s(t)$ are relatively skewed by a delay τ, the resultant signal $\hat{s}(t)$ can be described by

$$\hat{s}(t) \;=\; s_I(t) * \delta(t - \tau/2) + js_Q(t) * \delta(t + \tau/2), \tag{7.15}$$

which can be rewritten in the real-valued matrix form

$$\begin{bmatrix} \hat{s}_I(t) \\ \hat{s}_Q(t) \end{bmatrix} = \begin{bmatrix} \delta(t - \tau/2) & 0 \\ 0 & \delta(t + \tau/2) \end{bmatrix} \begin{bmatrix} s_I(t) \\ s_Q(t) \end{bmatrix}. \tag{7.16}$$

Also Eq. (7.16) belongs to the set of linear transformations defined in Eq. (7.2) but it is not strictly linear, as it does not comply with Eq. (7.9). Therefore, IQ skew is also a widely linear transformation in the complex domain, which can be represented by

$$\hat{s}(t) = d_1(t) * s(t) + d_2(t) * s^*(t), \tag{7.17}$$

where

$$\begin{aligned} d_1(t) &= [\delta(t - \tau/2) + \delta(t + \tau/2)]/2, \\ d_2(t) &= [\delta(t - \tau/2) - \delta(t + \tau/2)]/2. \end{aligned}$$

95

7.3.3 Chromatic dispersion compensation with IQ imbalance at the receiver

Consider that the signal $s(t)$ has propagated over a distance L in a single mode fiber, and that the receiver attempts to equalize the CD immediately after the coherent detection. The frequency response of the CD is given by

$$H_{cd}(\omega) = e^{-j\frac{\beta_2(\omega_c)}{2}\omega^2 L}. \tag{7.18}$$

Let $h_{cd}(t) = \mathcal{F}^{-1}\{H_{cd}(\omega)\}$ be the complex-valued impulse response of the chromatic dispersion, we can write

$$h_{cd}(t) = h_{cd,I}(t) + jh_{cd,Q}(t), \tag{7.19}$$

and $\hat{s}(t) = h_{cd}(t) * s(t)$, which corresponds to

$$\begin{bmatrix} \hat{s}_I(t) \\ \hat{s}_Q(t) \end{bmatrix} = \begin{bmatrix} h_{cd,I}(t) & -h_{cd,Q}(t) \\ h_{cd,Q}(t) & h_{cd,I}(t) \end{bmatrix} \begin{bmatrix} s_I(t) \\ s_Q(t) \end{bmatrix}. \tag{7.20}$$

If IQ imbalance is present at the receiver, we can use Eq. (7.14) and Eq. (7.20) to obtain

$$\begin{bmatrix} \hat{s}_I(t) \\ \hat{s}_Q(t) \end{bmatrix} = \begin{bmatrix} k_{11}h_{cd,I}(t) + k_{12}h_{cd,Q}(t) \\ k_{21}h_{cd,I}(t) + k_{22}h_{cd,Q}(t) \end{bmatrix}$$
$$\begin{matrix} -k_{11}h_{cd,Q}(t) + k_{12}h_{cd,I}(t) \\ -k_{21}h_{cd,Q}(t) + k_{22}h_{cd,I}(t) \end{matrix} \begin{bmatrix} s_I(t) \\ s_Q(t) \end{bmatrix}. \tag{7.21}$$

From Eq. (7.21), the equivalent signal $\hat{s}(t)$ which will be forwarded to the CD equalizer is given by

$$\hat{s}(t) = m_1(t) * s(t) + m_2(t) * s^*(t), \tag{7.22}$$

where

$$m_1(t) = [k_{11} + k_{22} + j(k_{21} - k_{12})]h_{cd}(t)/2$$
$$= K_1 h_{cd}(t),$$
$$m_2(t) = [k_{11} - k_{22} + j(k_{21} + k_{12})]h_{cd}^*(t)/2$$
$$= K_2 h_{cd}^*(t).$$

Since CD compensation is usually done in the frequency domain, it is convenient to write the equivalent system of Eq. (7.22) as

$$\hat{S}(\omega) = M_1(\omega)S(\omega) + M_2(\omega)S^*(-\omega), \tag{7.23}$$

where $S(\omega) = \mathcal{F}\{s(t)\}$, $S^*(-\omega) = \mathcal{F}\{s^*(t)\}$, and

$$M_1(\omega) = K_1 H_{cd}(\omega),$$
$$M_2(\omega) = K_2 H_{cd}^*(-\omega).$$

Finally, assuming that the receiver applies the standard ZF equalizer $H_{cd}^{-1}(\omega) = H_{cd}^*(\omega) = H_{cd}^*(-\omega)$ to compensate the CD, it results in

$$
\begin{aligned}
\hat{S}_{\text{ZF}}(\omega) &= H_{cd}^{-1}(\omega)\hat{S}(\omega), \\
&= G_1(\omega)S(\omega) + G_2(\omega)S^*(-\omega),
\end{aligned}
\tag{7.24}
$$

where

$$
\begin{aligned}
G_1(\omega) &= K_1, \\
G_2(\omega) &= K_2[H_{cd}^*(\omega)]^2.
\end{aligned}
$$

7.3.4 Chromatic dispersion compensation with IQ skew at the receiver

Considering that the receiver adds IQ time skew to a dispersed signal, from Eq. (7.16) and Eq. (7.20), and following the same steps of subsection 7.3.3, we obtain

$$
\begin{bmatrix} \hat{s}_I(t) \\ \hat{s}_Q(t) \end{bmatrix} = \begin{bmatrix} h_{cd,I}(t - \tau/2) & -h_{cd,Q}(t - \tau/2) \\ h_{cd,Q}(t + \tau/2) & h_{cd,I}(t + \tau/2) \end{bmatrix} \begin{bmatrix} s_I(t) \\ s_Q(t) \end{bmatrix}
\tag{7.25}
$$

Therefore, $\hat{s}(t)$ can be expressed as

$$\hat{s}(t) = h_1(t) * s(t) + h_2(t) * s^*(t),\tag{7.26}$$

where

$$
\begin{aligned}
h_1(t) &= \{h_{cd,I}(t - \tau/2) + h_{cd,I}(t + \tau/2) \\
&\quad + j[h_{cd,Q}(t + \tau/2) + h_{cd,Q}(t - \tau/2)]\}/2, \\
h_2(t) &= \{h_{cd,I}(t - \tau/2) - h_{cd,I}(t + \tau/2) \\
&\quad + j[h_{cd,Q}(t + \tau/2) - h_{cd,Q}(t - \tau/2)]\}/2.
\end{aligned}
$$

The equivalent system of Eq. (7.26) in the frequency domain can be written as

$$\hat{S}(\omega) = H_1(\omega)S(\omega) + H_2(\omega)S^*(-\omega),\tag{7.27}$$

where

$$
\begin{aligned}
H_1(\omega) &= \{H_{cd,I}(\omega)e^{-j\omega\tau/2} + H_{cd,I}(\omega)e^{j\omega\tau/2} \\
&\quad + j[H_{cd,Q}(\omega)e^{j\omega\tau/2} + H_{cd,Q}(\omega)e^{-j\omega\tau/2}]\}/2 \\
&= H_{cd}(\omega)\cos(\omega\tau/2),
\end{aligned}
$$

$$
\begin{aligned}
H_2(\omega) &= \{H_{cd,I}(\omega)e^{-j\omega\tau/2} - H_{cd,I}(\omega)e^{j\omega\tau/2} \\
&\quad + j[H_{cd,Q}(\omega)e^{j\omega\tau/2} - H_{cd,Q}(\omega)e^{-j\omega\tau/2}]\}/2 \\
&= -jH_{cd}^*(-\omega)\sin(\omega\tau/2).
\end{aligned}
$$

Again, assuming ZF compensation of CD, the result is

$$
\begin{aligned}
\hat{S}_{\text{ZF}}(\omega) &= H_{cd}^{-1}(\omega)\hat{S}(\omega) \\
&= G_1(\omega)S(\omega) + G_2(\omega)S^*(-\omega),
\end{aligned} \tag{7.28}
$$

where

$$
\begin{aligned}
G_1(\omega) &= \cos(\omega\tau/2), \\
G_2(\omega) &= -j[H_{cd}^*(\omega)]^2 \sin(\omega\tau/2).
\end{aligned}
$$

7.3.5   Discussion on the implications of the models

Consider the usual situation where, after ZF equalization of CD, the signal is forwarded to an adaptive equalizer, as discussed in Section 7.1. Analyzing the expressions obtained in Eq. (7.24) and Eq. (7.28) the following important remarks can be discussed:

1. Since $G_1(\omega)$ and $G_2(\omega)$ are both strictly linear complex-valued transfer functions, the signal obtained after ZF compensation of CD is only completely described by a widely linear complex operation on $S(\omega)$. By observing this fact, we can infer that a standard strictly linear complex-valued equalizer will present a poor performance in recovering $S(\omega)$, since its structure can not completely represent the widely linear transformation operated on the signal. Therefore, optimal linear equalization performance should be achieved only by widely linear complex-valued equalizer structure, or by its correspondence in the real-valued two-dimensional space.

98

2. In fact, the impact of the conjugate term on the equalizer performance can even be quantified, if we consider that it should be proportional to the signal to interference power ratio. The power of the interference can be calculated from the term $G_2(\omega)S^*(-\omega)$ [144].

3. To optimally recover $S(\omega)$, in the MMSE sense, the adaptive equalizer must be able to jointly process $\hat{S}_{\text{ZF}}(\omega)$ and $\hat{S}^*_{\text{ZF}}(-\omega)$, in order to invert the transfer functions $G_1(\omega)$ and $G_2(\omega)$. However, the impulse response $g_2(t) = \mathcal{F}^{-1}\{G_2(\omega)\}$ is twice as long as the response of the chromatic dispersion. Therefore, the complexity required to equalize such signal will scale proportionally to twice the complexity of zero-forcing CD compensation, independently if the equalizer is implemented with all real-valued or all complex-valued filters. This interesting conclusion explains why in [141] and [142] four (instead of the usual two) independent CD compensation complex-valued filters are necessary to enable a low complexity adaptive equalizer to compensate the IQ skew at the receiver. It also explains why in [140] a large number of taps is required to recover the signal with the adaptive equalizer. The equalizer number of taps is also the limitation of [139], which fails when the signal has a significant amount of accumulated CD, as indicated in [142]. In fact, we can point out the equalizer structures proposed in [139–142] are equivalent in the sense that, giving the necessary number of equalizer taps to solve the equalization problem, they should provide similar performance.

7.3.6 Comments on the WL-ZF equalization of IQ-mixing and CD

The presence of the conjugate terms in Eq. (7.23) and (7.27) implies that a complex-valued stricty linear ZF equalizer will not be able to completely eliminate the effect of the CD, since it cannot simultaneously compensate for $H_{cd}(\omega)$ and $H^*_{cd}(\omega)$. Another approach for this problem would be to design a WL-ZF equalizer of CD which includes the effects of IQ-mixing. Such equalizer structure can be found by inverting the matrices in Eq. (7.21) and (7.25). In general, for a WL system described by

$$\hat{S}(\omega) = C_1(\omega)S(\omega) + C_2(\omega)S^*(-\omega), \tag{7.29}$$

assuming that $C_1(\omega)$ and $C_2(\omega)$ are invertible, the ZF widely linear equalizer will be given by

$$\hat{S}_{WL-ZF}(\omega) = \frac{C_1^*(-\omega)}{C_1(\omega)C_1^*(-\omega) - C_2(\omega)C_2^*(-\omega)}\hat{S}(\omega)$$
$$-\frac{C_2(\omega)}{C_1(\omega)C_1^*(-\omega) - C_2(\omega)C_2^*(-\omega)}\hat{S}^*(-\omega). \qquad (7.30)$$

Note that if $C_2(\omega) = 0$, then

$$\hat{S}_{WL-ZF}(\omega) = \frac{1}{C_1(\omega)}\hat{S}(\omega), \qquad (7.31)$$

which corresponds to the strictly linear ZF equalizer of $C_1(\omega)$. A necessary condition for the system in Eq. (7.29) to be invertible is $D(\omega) = C_1(\omega)C_1^*(-\omega) - C_2(\omega)C_2^*(-\omega) \neq 0$ for all ω. It is easy to check that for the systems in Eq. (7.27) and Eq. (7.28) $D(\omega) = 1$ always, which shows that any combination of IQ skew and CD can be fully compensated. Of course, since the design of the WL-ZF equalizer requires the receiver to know exactly the IQ imbalance of IQ skew at the front-end, the best procedure would be to compensate the IQ-mixing before the equalization blocks and save DSP complexity. Nevertheless, Eq. (7.30) outlines what a complex-valued WL adaptive equalizer should look like to recover a signal impaired by IQ-mixing and CD.

A hybrid approach to solve the equalization problem is also possible, as indirectly demonstrated in references [141] and [142]. There, the authors propose to modify the ZF equalization of CD and to take advantage of symmetries of the CD impulse response to reduce complexity, further using a 4×2 complex-valued adaptive equalizer to compensate for the IQ skew. Their approach can be seen as the result of a direct application of Eq. (7.30) to find the WL equalizer for the system in Eq. (7.27). However, this approach may impose challenges to the synchronization and timing recovery algorithms, since they have to be performed before compensation of CD.

7.4   Adaptive equalizer using augmented Jones vectors

Coherent optical receivers commonly employ finite impulse response (FIR) MIMO adaptive equalizers to perform polarization demultiplexing and to approximating the matched filtered detection. In the previous sections, it

was shown how the augmented complex-valued signal processing could be used to obtain models in the complex domain which adequately represent IQ-mixing related effects. The aim of this section is to derive a general complex-valued MIMO adaptive equalizer structure which should be able to compensate for reversible IQ-mixing effects.

From now on the signals are assumed to be discrete time versions of their respective continuous-time waveforms, sampled at least to the double of the baud rate. The elements in the matrix representation of the equalizers are FIR filters.

7.4.1   Equalizer general structure

The structure of the most general adaptive equalizer for a polarization multiplexed receiver is given by

$$
\begin{bmatrix} \hat{x}_I \\ \hat{x}_Q \\ \hat{y}_I \\ \hat{y}_Q \end{bmatrix} = \begin{bmatrix} \boldsymbol{h}_{x_I x_I}^T & \boldsymbol{h}_{x_I x_Q}^T & \boldsymbol{h}_{x_I y_I}^T & \boldsymbol{h}_{x_I y_Q}^T \\ \boldsymbol{h}_{x_Q x_I}^T & \boldsymbol{h}_{x_Q x_Q}^T & \boldsymbol{h}_{x_Q y_I}^T & \boldsymbol{h}_{x_Q y_Q}^T \\ \boldsymbol{h}_{y_I x_I}^T & \boldsymbol{h}_{y_I x_Q}^T & \boldsymbol{h}_{y_I y_I}^T & \boldsymbol{h}_{y_I y_Q}^T \\ \boldsymbol{h}_{y_Q x_I}^T & \boldsymbol{h}_{y_Q x_Q}^T & \boldsymbol{h}_{y_Q y_I}^T & \boldsymbol{h}_{y_Q y_Q}^T \end{bmatrix} \begin{bmatrix} \boldsymbol{x}_I \\ \boldsymbol{x}_Q \\ \boldsymbol{y}_I \\ \boldsymbol{y}_Q \end{bmatrix} . \tag{7.32}
$$

It corresponds to a 4×4 real-valued MIMO system where the inputs are the real and imaginary parts of the received complex-valued polarization signals $(\boldsymbol{x}, \boldsymbol{y})$: $\boldsymbol{x}_I = \operatorname{Re}(\boldsymbol{x})$, $\boldsymbol{x}_Q = \operatorname{Im}(\boldsymbol{x})$, $\boldsymbol{y}_I = \operatorname{Re}(\boldsymbol{y})$, $\boldsymbol{y}_Q = \operatorname{Im}(\boldsymbol{y})$. For convenience, define

$$
\mathbf{M}_4 = \begin{bmatrix} \boldsymbol{h}_{x_I x_I}^T & \boldsymbol{h}_{x_I x_Q}^T & \boldsymbol{h}_{x_I y_I}^T & \boldsymbol{h}_{x_I y_Q}^T \\ \boldsymbol{h}_{x_Q x_I}^T & \boldsymbol{h}_{x_Q x_Q}^T & \boldsymbol{h}_{x_Q y_I}^T & \boldsymbol{h}_{x_Q y_Q}^T \\ \boldsymbol{h}_{y_I x_I}^T & \boldsymbol{h}_{y_I x_Q}^T & \boldsymbol{h}_{y_I y_I}^T & \boldsymbol{h}_{y_I y_Q}^T \\ \boldsymbol{h}_{y_Q x_I}^T & \boldsymbol{h}_{y_Q x_Q}^T & \boldsymbol{h}_{y_Q y_I}^T & \boldsymbol{h}_{y_Q y_Q}^T \end{bmatrix} . \tag{7.33}
$$

The equalizer structure in Eq. (7.32) should be able to compensate a general reversible channel response that can be entirely represented as a linear transformation in $\mathbb{R}^4$. It is possible to show that, in absence of IQ-mixing, such equalizer can be reduced to the standard 2×2 complex-valued equalizer defined by

$$
\begin{bmatrix} \hat{x} \\ \hat{y} \end{bmatrix} = \begin{bmatrix} \boldsymbol{h}_{xx}^H & \boldsymbol{h}_{xy}^H \\ \boldsymbol{h}_{yx}^H & \boldsymbol{h}_{yy}^H \end{bmatrix} \begin{bmatrix} \boldsymbol{x} \\ \boldsymbol{y} \end{bmatrix} , \tag{7.34}
$$

where $\mathbf{s} = \begin{bmatrix} \boldsymbol{x} & \boldsymbol{y} \end{bmatrix}^T$ and $\hat{\mathbf{s}} = \begin{bmatrix} \hat{x} & \hat{y} \end{bmatrix}^T$ are the Jones vector representation of equalizer's input and output, respectively. Note that $\hat{\mathbf{s}} \in \mathbb{C}^{2\times 1}$, while

$\mathbf{s} \in \mathbb{C}^{2N \times 1}$ and the $\boldsymbol{h}$-elements of $\mathbf{M}_4 \in \mathbb{R}^{N \times 1}$, where N is the number of taps of the equalizer's FIR structure.

Equation (7.34) follows directly from the strict linearity of the CD and PMD in the complex domain. However, in the general case, the structures of Eq. (7.32) and Eq. (7.34) are not equivalent. In order to derive the equivalent version of Eq. (7.32) in the complex domain, we perform the linear transformation defined in Eq. (7.4). In this case, the $\mathbf{T}_N$ transformation defined in Eq. (7.1) resolves to

$$
\mathbf{T}_2 = \begin{bmatrix} 1 & j & 0 & 0 \\ 1 & -j & 0 & 0 \\ 0 & 0 & 1 & j \\ 0 & 0 & 1 & -j \end{bmatrix}. \tag{7.35}
$$

Note that, for convenience, the columns and rows of $\mathbf{T}_2$ were linearly rearranged in order to clarify the following steps, and that this linear transformation does not change its unitary properties. The matrix $\mathbf{T}_2$ can then be used to define the *augmented* Jones vector $\underline{\mathbf{s}}$, which is obtained by

$$
\underline{\mathbf{s}} = \begin{bmatrix} x \\ x^* \\ y \\ y^* \end{bmatrix} = \begin{bmatrix} 1 & j & 0 & 0 \\ 1 & -j & 0 & 0 \\ 0 & 0 & 1 & j \\ 0 & 0 & 1 & -j \end{bmatrix} \begin{bmatrix} x_I \\ x_Q \\ y_I \\ y_Q \end{bmatrix}. \tag{7.36}
$$

Directly applying Eq. (7.4) to $\mathbf{T}_2$ and $\mathbf{M}_4$, and after some algebric manipulation, we have that

$$
\hat{\mathbf{s}} = \mathbf{H}_{\mathbf{s_1}} \mathbf{s} + \mathbf{H}_{\mathbf{s_2}} \mathbf{s}^*, \tag{7.37}
$$

where

$$
\mathbf{H}_{\mathbf{s_1}} = \frac{1}{2} \begin{bmatrix} \boldsymbol{h}^T_{x_I x_I} + \boldsymbol{h}^T_{x_Q x_Q} + j(\boldsymbol{h}^T_{x_Q x_I} - \boldsymbol{h}^T_{x_I x_Q}) \\ \boldsymbol{h}^T_{y_I x_I} + \boldsymbol{h}^T_{y_Q x_Q} + j(\boldsymbol{h}^T_{y_Q x_I} - \boldsymbol{h}^T_{y_I x_Q}) \end{bmatrix}
$$
$$
\begin{bmatrix} \boldsymbol{h}^T_{x_I y_I} + \boldsymbol{h}^T_{x_Q y_Q} + j(\boldsymbol{h}^T_{x_Q y_I} - \boldsymbol{h}^T_{x_I y_Q}) \\ \boldsymbol{h}^T_{y_I y_I} + \boldsymbol{h}^T_{y_Q y_Q} + j(\boldsymbol{h}^T_{y_Q y_I} - \boldsymbol{h}^T_{x_I y_Q}) \end{bmatrix}, \tag{7.38}
$$

$$
\mathbf{H}_{\mathbf{s_2}} = \frac{1}{2} \begin{bmatrix} \boldsymbol{h}^T_{x_I x_I} - \boldsymbol{h}^T_{x_Q x_Q} + j(\boldsymbol{h}^T_{x_Q x_I} + \boldsymbol{h}^T_{x_I x_Q}) \\ \boldsymbol{h}^T_{y_I x_I} - \boldsymbol{h}^T_{y_Q x_Q} + j(\boldsymbol{h}^T_{y_Q x_I} + \boldsymbol{h}^T_{y_I x_Q}) \end{bmatrix}
$$
$$
\begin{bmatrix} \boldsymbol{h}^T_{x_I y_I} - \boldsymbol{h}^T_{x_Q y_Q} + j(\boldsymbol{h}^T_{x_Q y_I} + \boldsymbol{h}^T_{x_I y_Q}) \\ \boldsymbol{h}^T_{y_I y_I} - \boldsymbol{h}^T_{y_Q y_Q} + j(\boldsymbol{h}^T_{y_Q y_I} + \boldsymbol{h}^T_{x_I y_Q}) \end{bmatrix}, \tag{7.39}
$$

which leads to the widely linear MIMO complex-valued equalizer structure

$$\begin{bmatrix} \hat{x} \\ \hat{y} \end{bmatrix} = \begin{bmatrix} \boldsymbol{h}_{\text{xx}}^{H} & \boldsymbol{h}_{\text{xy}}^{H} \\ \boldsymbol{h}_{\text{yx}}^{H} & \boldsymbol{h}_{\text{yy}}^{H} \end{bmatrix} \begin{bmatrix} \boldsymbol{x} \\ \boldsymbol{y} \end{bmatrix} + \begin{bmatrix} \boldsymbol{h}_{\text{xx}^*}^{H} & \boldsymbol{h}_{\text{xy}^*}^{H} \\ \boldsymbol{h}_{\text{yx}^*}^{H} & \boldsymbol{h}_{\text{yy}^*}^{H} \end{bmatrix} \begin{bmatrix} \boldsymbol{x}^* \\ \boldsymbol{y}^* \end{bmatrix} . \tag{7.40}$$

The corresponding block diagram for the equalizer is depicted in Fig. 7.1.
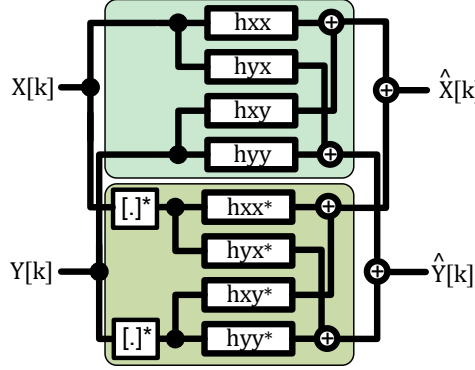
Figure 7.1 Block diagram of the 2×2 MIMO complex-valued WL adaptive equalizer.

Observe that Eq. (7.40) reduces to Eq. (7.34) (i.e. $\mathbf{H_{s_2}} = \mathbf{0}$) if there is no mixing between IQ components in the received signal. One advantage of the structure in Eq. (7.40) over the one in Eq. (7.32) is that, since blind equalization algorithms usually rely on the two-dimensional statistical properties of complex-valued signals, those algorithms are easier to derive for a complex-valued equalizer.

7.4.2 Filter coefficients update algorithm

Taking as the starting point the complex-valued least mean square (CLMS) algorithm, the widely linear CLMS (WL-CLMS) can be derived [150]. The adaptation rules used to train a the WL-CLMS are similar to the ones obtained for the CLMS, as shown in [151] and [150].

However, to make the dynamic update of the FIR coefficients independent of the carrier phase, the update rules for the widely linear MIMO equalizer used in this paper were implemented based on the algorithm described in [151], modified to use the decision directed least radius distance (DD-LRD) error criteria [152]. These error criteria can be easily changed to perform a radius directed equalizer (RDE) mode, in order to implement

unsupervised training of the equalizer's coefficients. The filters of $\mathbf{H_{s_1}}$ and $\mathbf{H_{s_2}}$ are updated according to Eq. (7.41) and (7.42), respectively, with

$$\boldsymbol{h}_{\mathrm{xx}}(k+1) = \boldsymbol{h}_{\mathrm{xx}}(k) + \mu e_{\mathrm{x}}(k)\boldsymbol{x}^*(k),$$
$$\boldsymbol{h}_{\mathrm{xy}}(k+1) = \boldsymbol{h}_{\mathrm{xy}}(k) + \mu e_{\mathrm{x}}(k)\boldsymbol{y}^*(k),$$
$$\boldsymbol{h}_{\mathrm{yx}}(k+1) = \boldsymbol{h}_{\mathrm{yx}}(k) + \mu e_{\mathrm{y}}(k)\boldsymbol{x}^*(k),$$
$$\boldsymbol{h}_{\mathrm{yy}}(k+1) = \boldsymbol{h}_{\mathrm{yy}}(k) + \mu e_{\mathrm{y}}(k)\boldsymbol{y}^*(k), \tag{7.41}$$

$$\boldsymbol{h}_{\mathrm{xx}^*}(k+1) = \boldsymbol{h}_{\mathrm{xx}^*}(k) + \mu e_{\mathrm{x}}(k)\boldsymbol{x}(k),$$
$$\boldsymbol{h}_{\mathrm{xy}^*}(k+1) = \boldsymbol{h}_{\mathrm{xy}^*}(k) + \mu e_{\mathrm{x}}(k)\boldsymbol{y}(k),$$
$$\boldsymbol{h}_{\mathrm{yx}^*}(k+1) = \boldsymbol{h}_{\mathrm{yx}^*}(k) + \mu e_{\mathrm{y}}(k)\boldsymbol{x}(k),$$
$$\boldsymbol{h}_{\mathrm{yy}^*}(k+1) = \boldsymbol{h}_{\mathrm{yy}^*}(k) + \mu e_{\mathrm{y}}(k)\boldsymbol{y}(k), \tag{7.42}$$

where $0 < \mu < 1$ is the adaptation step, and $\{e_{\mathrm{x}}(k), e_{\mathrm{y}}(k)\}$ correspond to the error criteria, defined by

$$e_{\mathrm{x}}(k) = \hat{x}(k)(|x_d(k)|^2 - |\hat{x}(k)|^2),$$
$$e_{\mathrm{y}}(k) = \hat{y}(k)(|y_d(k)|^2 - |\hat{y}(k)|^2), \tag{7.43}$$

where $x_d(k)$ and $y_d(k)$ are training symbols.

Another possibility is to define

$$e_{\mathrm{x}}(k) = \hat{x}(k)(|R_{\mathrm{x}}(k)|^2 - |\hat{x}(k)|^2),$$
$$e_{\mathrm{y}}(k) = \hat{y}(k)(|R_{\mathrm{y}}(k)|^2 - |\hat{y}(k)|^2), \tag{7.44}$$

where $R_{\mathrm{x}}(k)$ and $R_{\mathrm{y}}(k)$ are the decided radius of the RDE algorithm.

Both error criteria are independent of frequency offset.

7.5 Simulation setup and numerical results

In this section, the performance of the widely linear adaptive equalizer is numerically investigated for DP transmission using M-QAM modulation formats, with $M = 16$, 64 and 256. The numerical simulation model is illustrated in Fig. 7.2.

All simulated cases assumed single channel configuration at a symbol rate (R_s) of 32 GBd. In the constellation mapping block, the sequences of M-QAM symbols were generated with a fixed length of 250000 symbols per polarization, mapped from decorrelated pieces of a pseudo-random binary
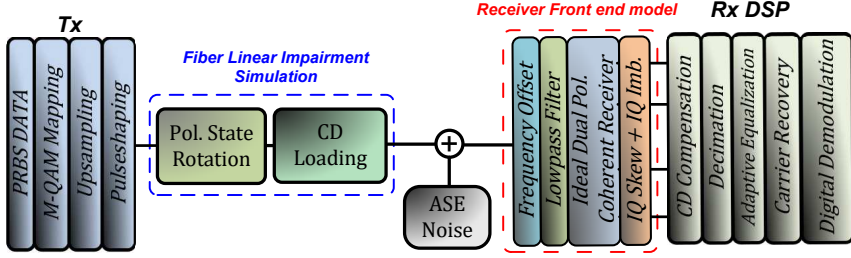
Figure 7.2 Numerical simulation setup of a simplified optical channel, with only fiber linear propagation effects and additive white Gaussian noise included.

sequence (PRBS) of length $2^{23} - 1$. The modulated data was upsampled to 16 samples per symbol, and pulse shaped using root raised cosine (RRC) filters with a roll-off factor of 0.01. For all tested cases, a fixed frequency offset of 100 MHz was imposed between the local oscillators at transmitter and receiver. No phase noise was considered.

The simplified linear optical channel model accounted for static linear polarization rotation, CD loading, and amplified spontaneous emission (ASE) from Erbium-doped fiber amplifier (EDFA), modeled as additive white Gaussian noise (AWGN). At the front-end model of the receiver, the frequency offset is added to the signal, which is filtered by an ideal rectangular low pass filter with a bandwidth of $1.1R_s$. This stage is followed by an ideal dual polarization coherent receiver, and a block to simulate IQ imbalance and IQ skew on the received polarizations. After the receiver front-end, a standard set of DSP algorithms for data demodulation is applied, consisting in frequency domain CD compensation, decimation, adaptive equalization, ideal carrier recovery (i.e., 100 MHz frequency offset compensation) and digital demodulation using hard symbol decisions with the minimum Euclidean distance metric.

The adaptive equalizers were implemented in the $T_s/2$-fractionally spaced mode, where $T_s = 1/R_s$, therefore requiring the signal to be sampled at $2R_s$.

For all results that follow, the label "complex" refers to the 2×2 complex-valued (strictly) linear equalizer structure defined in Eq. (7.34) and the label "WL complex" refers to the 2×2 complex-valued widely linear structure defined in Eq. (7.40). The chosen figure of merit for the receiver's performance comparisons is the Q^2-factor, in dB, which is calculated from the bit-error rate (BER) according to $Q_{dB}^2 = 20 \log_{10}[\sqrt{2}\text{erfcinv}(2BER)]$. Distinct optical signal-to-noise ratio (OSNR) values were chosen for each

tested modulation format in order to maintain the minimum BER values around 10^{-4} to 10^{-3} at the receiver. The OSNR is defined assuming a bandwidth of 12.5 GHz.

7.5.1 MSE convergence

Figure 7.3 shows the convergence of the equalizers in terms of mean square error (MSE) of the training iteration. Both equalizers were configured with 25 taps time response. For this particular example, each point corresponds to the mean square error calculated with a moving average window of 1000 iterations. These results refer to the polarization demultiplexing of a 32 GBd dual polarization 256QAM (DP-256QAM) signal in the "back-to-back" (AWGN) configuration with 37 dB of OSNR at the receiver's input.

Figure 7.3 (a) corresponds to the case where no IQ imbalance or IQ skew is present at the receiver front-end. The MSE of both equalizers converges to a minimum value of -35 dB. Figure 7.3 (b) corresponds to the case where the signals of both polarizations are subject to IQ imbalance and IQ skew. For this case, it can be noticed that the MSE of the 2×2 complex-valued linear equalizer shows an offset of more than 15 dB, compared with the curve in Fig. 7.3 (a). However, the same floor of MSE of -35 dB is reached with 2×2 complex-valued widely linear equalizer, regardless the presence or not of IQ-mixing.

The training period corresponds to a sequence of consecutive tap updates, with each iteration using one training symbol. In Fig. 7.3, it is shown the convergence of the equalizer for a training sequence (block) of 10×10^4 symbols. It can be noticed that the convergence is achieved in between 20×10^3 and 40×10^3 iterations, which provides an estimate of the required size of the training sequence. Additionally, it is also clear that both equalizers converge in the MSE with more or less the same number of iterations, which indicates that the complex-valued WL implementation did not increase the requirements of training length compared to the conventional strictly linear complex-valued structure.

7.5.2 Performance with IQ imbalance and skew in back-to-back

In Fig. 7.4 and Fig. 7.5, the performance surfaces of the receiver for the two complex-valued adaptive equalizers tested for different combinations of IQ amplitude (ϵ_{rx}) and phase imbalance (ϕ_{rx}), and IQ skew, respectively.

106
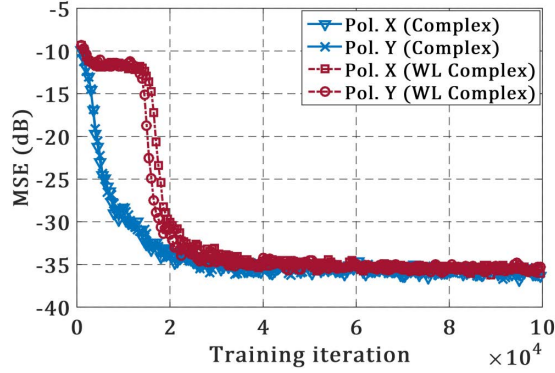
(a)
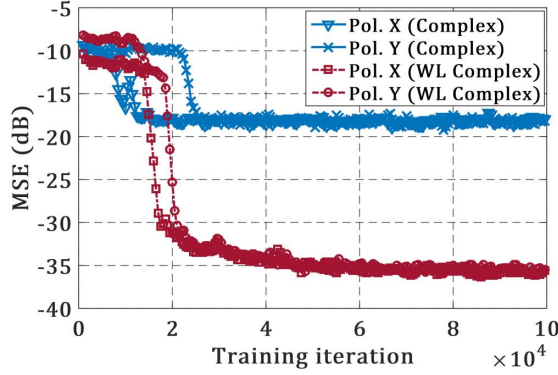
(b)

Figure 7.3 Example of MSE evolution during the equalizers' training iterations. (a) MSE evolution in absence of IQ-mixing effects; (b) MSE evolution for both polarizations subject to: $\epsilon_{rx} = 0.05$ (IQ amplitude imbalance), $\phi_{rx} = 4°$ (IQ phase imbalance), and $\tau = 0.25T_s$ (IQ skew).

The performance is evaluated in the stationary regime, i.e. after convergence in the MSE during the training period. Both equalizers were configured to use 25 taps. As it can be seen, in the presence of any of the impairments, the performance of the 2×2 complex-valued equalizer is degraded. The penalty in Q^2-factor, as one would expect, also increases with the order of the modulation format. On the other hand, for all tested cases, the optimal performance is maintained using 2×2 complex-valued WL equalizer. Optimal refers to the receiver performance after 2×2 complex-valued linear equalization in the absence of any IQ-mixing at the receiver front-end.

107

(a)

(b)

(c)
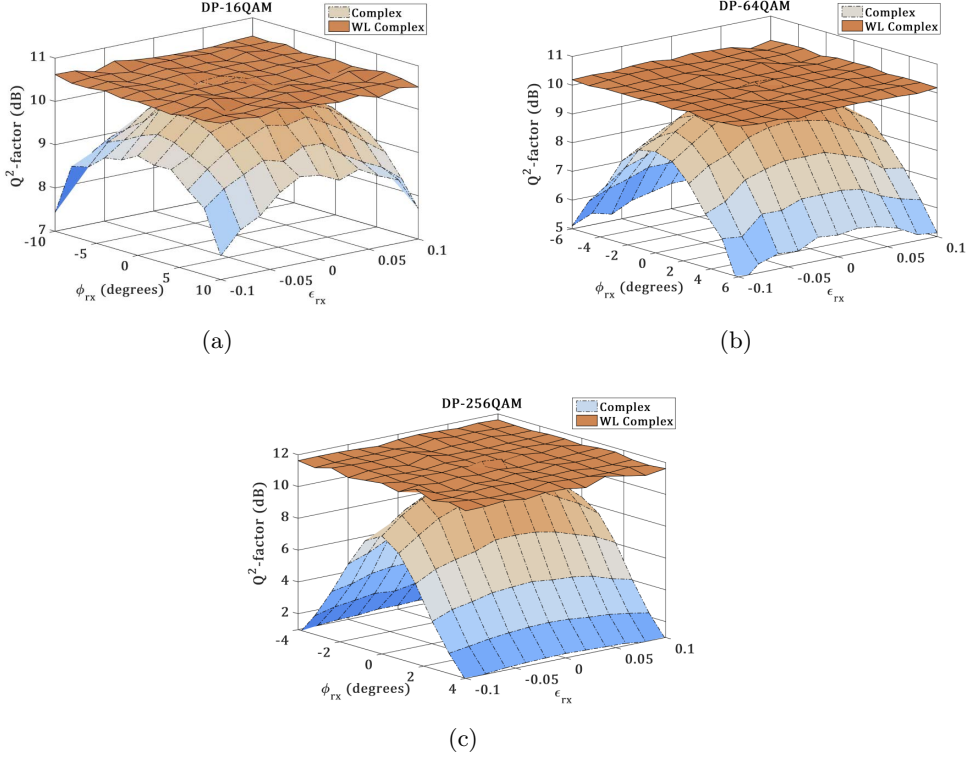
Figure 7.4 Back-to-back performance after 2×2 complex-valued equalization and after 2×2 widely linear complex-valued equalization for a dual polarization coherent receiver. The plots show Q^2-factor vs normalized IQ amplitude imbalance (ϵ_{rx}) and IQ phase imbalance (ϕ_{rx}). Same values applied simultaneously to both polarizations at the receiver front-end. (a) 32 GBd DP-16QAM with OSNR$_{RX}$= 22 dB; (b) 32 GBd DP-64QAM with OSNR$_{RX}$= 28 dB; (c) 32 GBd DP-256QAM with OSNR$_{RX}$= 37 dB.

The spikes appearing in the performance surfaces of the 2×2 complex-valued linear equalizer are attributed to convergence to the same polarization. Since this structure cannot handle IQ-mixing, those extreme cases where one polarization is correctly received while the other is severely impaired by IQ skew may have an increased probability of convergence to the same polarization. However, an additional study would be necessary to characterize the cause and frequency of such events precisely.

(a)

(b)

(c)
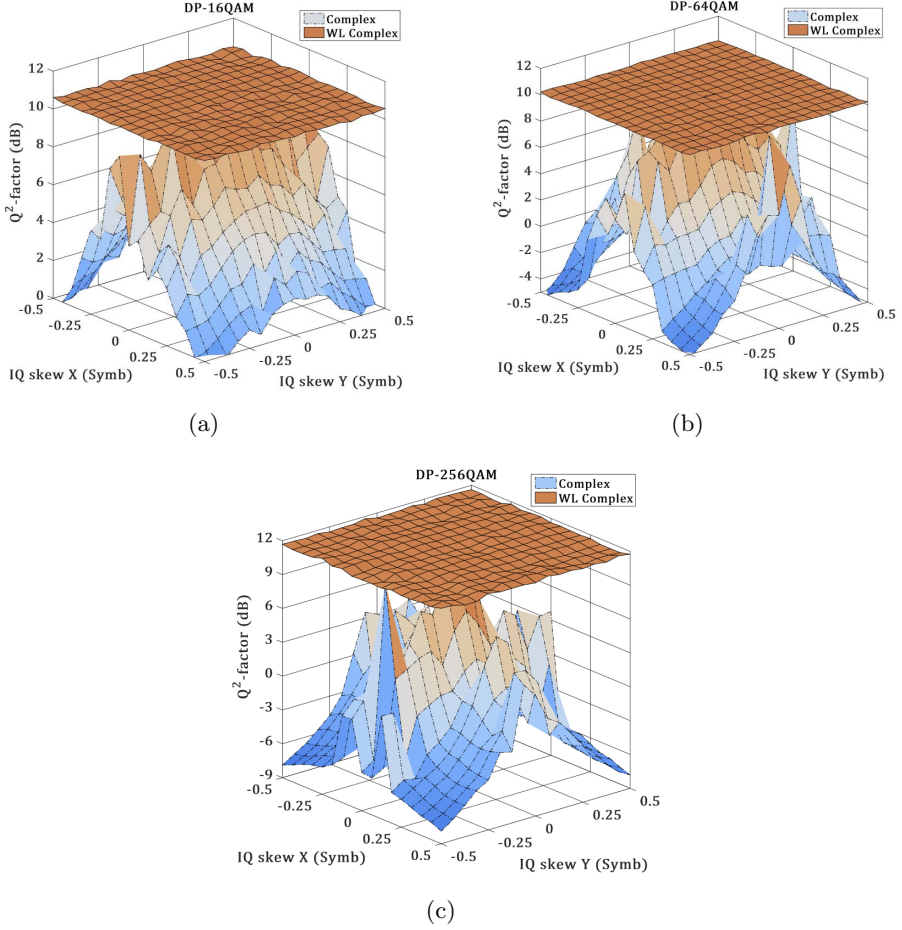
Figure 7.5 Back-to-back performance after 2×2 complex-valued equalization and after 2×2 widely linear complex-valued equalization for a dual polarization coherent receiver subject to IQ skew. The plots show Q^2-factor vs IQ skew as a fraction of the symbol period. (a) 32 GBd DP-16QAM with $\text{OSNR}_{RX}= 22$ dB; (b) 32 GBd DP-64QAM with $\text{OSNR}_{RX}= 28$ dB; (c) 32 GBd DP-256QAM with $\text{OSNR}_{RX}= 37$ dB.

7.5.3 Performance with IQ imbalance and skew after zero-forcing CD compensation

Here the receiver performance is compared when the signal is sent to the adaptive equalizer after zero-forcing equalization of a significant amount of CD. For all simulated cases, the assumption is that the receiver front-end adds $\epsilon_{rx} = 0.05$ of IQ amplitude imbalance, $\phi_{rx} = 4°$ of IQ phase imbalance,

and $\tau = 0.25T_s$ of IQ skew, for both received polarizations.

(a)

(b)

(c)
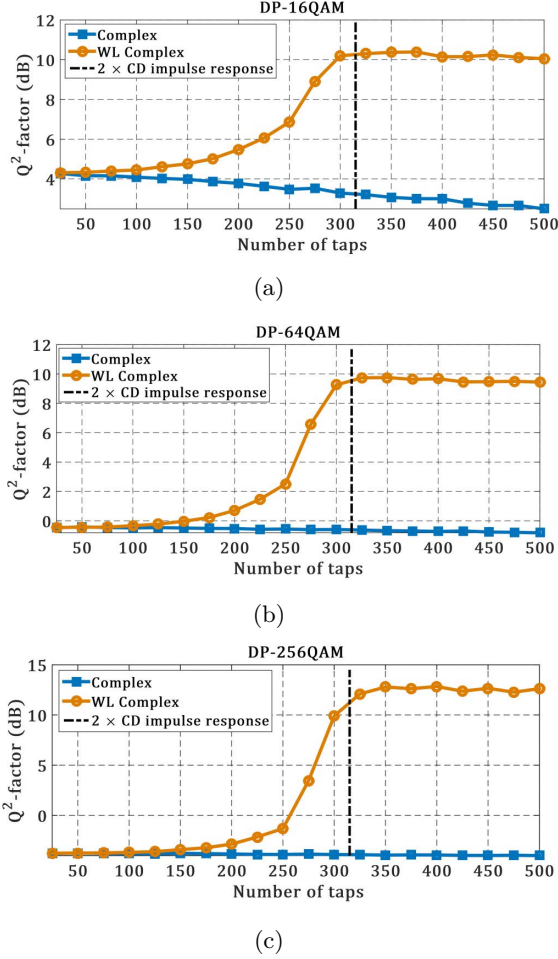
Figure 7.6 Performance comparison in Q^2-factor vs number of equalizer taps after zero-forcing CD compensation of 9600 ps/nm, equivalent to 600 km of transmission over a single mode fiber with dispersion parameter 16 ps/nm/km. (a) DP-16QAM, OSNR$_{RX}$= 22 dB; (b) DP-64QAM, OSNR$_{RX}$= 28 dB; (c) DP-256QAM, OSNR$_{RX}$= 37 dB.

The parameters of the CD loading stage were configured to provide a total of 9600 ps/nm of accumulated CD, which is equivalent to a transmission over 600 km of single mode fiber with a dispersion parameter of 16 ps/nm/km at 1550 nm.

Using the analytic expressions in [153], we can calculate that a 32 GBd signal, sampled at 64 GS/s, would require from a $T_s/2$ fractionally spaced

equalizer (FSE) a minimum of 158 taps to compensate for such amount of CD. The value corresponding to twice of this lower bound, 316 taps, is indicated by the vertical dashed lines in the subfigures of Fig. 7.6.

The results shown in Fig. 7.6 demonstrate that the complex-valued 2×2 equalizer is not able to recover the signal with any number of taps configuration. On the other hand, the performance of the 2×2 complex-valued WL equalizer clearly depends on its number of taps. In particular, when the number of taps exceeds 316 (i.e., twice the CD impulse response duration), the performance of the receiver is identical to the one obtained with no CD loading. Therefore, these results are in agreement with the conclusions drawn from the analysis presented in Section 7.3. Finally, Fig. 7.7 shows that the same behavior of the 2×2 complex-valued WL equalizer observed in Fig. 7.6 is reproduced for different transmission distances.
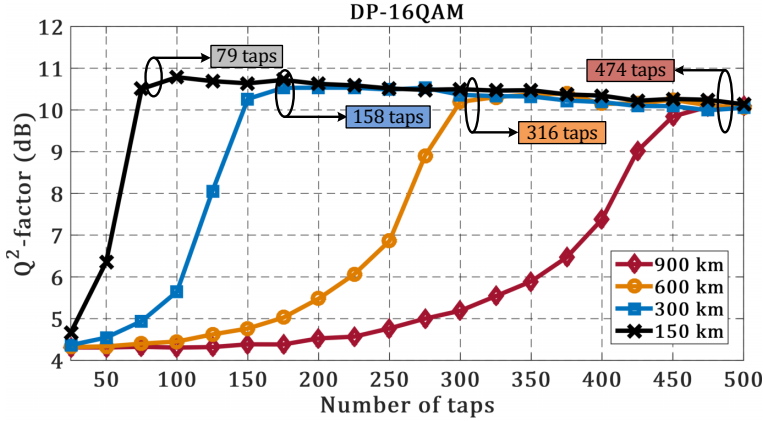
Figure 7.7 Receiver performance of DP-16QAM, $\text{OSNR}_{RX}= 22$ dB, using the adaptive WL equalizer after zero-forcing CD compensation. Each curve refer to a fixed transmission distance (dispersion parameter 16 ps/nm/km) and indicate the Q^2-factor as a function of the equalizer number of taps. The values pointed by the arrows indicate the corresponding number of taps to cover twice of CD response duration for each respective distance.

7.5.4 Additional comments

As the results have shown, a widely linear equalization structure can be used to compensate practically all reversible combinations of IQ imbalance and IQ skew present at the receiver. However, such capability doubles the complexity of the standard channel equalization. Therefore, considering how the requirements increase with the amount accumulated CD in the

transmission link, we can point out that, for long haul systems, the overhead of complexity may be too large for practical implementation.

Nevertheless, the models derived in Section 7.3 can be used to investigate the impact of receiver front-end imperfections on the performance of long-haul transceivers, which is useful information for equipment calibration and the development of algorithms to estimate and compensate IQ-mixing effects before the DSP equalization blocks.

On the other hand, for metro networks and short-range transceivers, where the amount of accumulated CD can be reasonably small, such equalizer structure tend to increase its cost-effectiveness, since the use of widely linear equalization may, for example, relax the requirements on the subsystems components employed in coherent receivers. For the last, the study of the symmetries of the complex-valued WL models may provide insights to optimize its DSP implementations.

7.6   Summary

In this chapter, it was shown that using augmented complex analysis, useful complex-valued models for IQ imbalance and IQ skew in coherent optical receivers can be derived. It was demonstrated how such models naturally connect the compensation of such impairments and the general equalization problem of the linear channel response.

It was shown that the attempting to use a conventional zero-forcing CD equalizer under the presence of IQ-mixing receiver front-end imperfections results in a two-fold increase in the complexity required by the adaptive equalization algorithm, with respect to the static CD equalizer, independently of the implementation domain (real-valued space or complex-valued space).

Based on the augmented complex analysis, it was proposed and extensively validated by numerical simulations, for different M-QAM modulation formats, a widely linear complex-valued adaptive equalizer structure for a polarization multiplexed receiver. The proposed structure is able to maintain optimal performance, in the MMSE sense, under the presence of IQ imbalance and IQ skew at the receiver front-end. Results from extensive numerical simulations have shown that the performance of the proposed equalizer agrees with the analytical models first derived.

Chapter 8

Widely linear equalization for transmitter IQ-mixing compensation in multicarrier systems

In Chapter 7, widely linear models were introduced to analyze the impact of in-phase/quadrature (IQ)-mixing in coherent optical receivers. In this chapter, this analysis is extended to investigate the effect of IQ-mixing at the transmitter side of multicarrier systems.

Multicarrier systems have been extensively investigated in coherent optical communication systems. The most popular techniques for subcarrier multiplexing comprise orthogonal frequency-division multiplexing (OFDM) [54,154], Nyquist-wavelength-division multiplexing (WDM) [155] and super-Nyquist-WDM [156]. Some variants of OFDM, such as offset-QAM [157] have also been investigated. Nyquist-WDM and OFDM are the main digital signal processing (DSP)-enabled techniques for superchannel transmission at terabit rates [158] with high spectral efficiency. From the network perspective, those techniques are proposed to enable functionalities such as flexible spectrum allocation and rate adaptive transceivers [159].

These systems also play a role in the mitigation of nonlinear distortions. Numerical results obtained with the enhanced Gaussian noise (EGN) model [160,161] predict the existence of optimum symbol rates that minimize the accumulation of nonlinear interference (NLI) for a given fiber link. Based on these estimations, symbol rate optimized multicarrier systems

have been investigated as an alternative to mitigate Kerr nonlinearities in WDM systems [162, 163].

Therefore, multicarrier systems have an important place in the state-of-the-art of coherent optical communication, and that is the main motivation for the work presented in this chapter. The content of this chapter directly relates to the work published by the author in [C4].

8.1   Introduction

In similar lines of the discussion presented in Chapter 7, the performance of multicarrier systems can be degraded by imperfections or incorrect calibration that can lead to IQ imbalance and IQ skew, i.e., IQ-mixing effects at the transmitters or receivers. Assuming that the receiver DSP should take the task of compensating for such effects, it is necessary to analyze how the presence of IQ-mixing affects the transmitted subcarriers in a multicarrier signal.

One possible strategy to tackle this problem would be to attempt to eliminate IQ-mixing before the channel equalization, using algorithms based on e.g. Gram–Schmidt orthogonalization procedures (GSOP) [164, 165] and independent component analysis (ICA) [166]. However, the effectiveness of these algorithms depends on specific scenarios of application. Moreover, in case these methods exhibit poor or suboptimal performance, they will unavoidably impact the performance of the channel equalization [165]. Therefore, as in Chapter 7, here it is assumed that the IQ-mixing is to be compensated by the adaptive equalizer stage.

In [167], the presence of IQ skew is shown to cause linear self-interference between symmetric subcarriers in a multicarrier signal. The authors propose a least mean square (LMS) 8×8 multiple-input multiple-output (MIMO) real-valued adaptive equalizer to compensate for IQ skew present at the transmitter. However, the LMS algorithm requires knowledge of the phase of all subcarriers at the receiver simultaneously which, in practice, can be a complicated task to be performed before the separation of the polarization components and equalization. Alternatively, a blind equalization strategy can be employed [139, 142]. Blind equalization algorithms rely on the statistical properties of the complex-valued signals.

However, as discussed in Chapter 7, IQ-mixing interference can not be completely captured by standard (strictly linear) complex-valued models [J3], commonly used for adaptive equalization in polarization multiplexed systems. Therefore, to make the equalization robust to IQ-mixing, the

strictly linear complex-valued equalizer models have to be extended to widely linear (WL) models. In [168], the performance degradation due to IQ imbalance is investigated for a RF-based direct-detection OFDM system. The authors also conclude that IQ imbalance imposes self-interference between symmetric OFDM subcarriers and propose a MIMO multimodulus algorithm (MMA) equalizer to compensate for it. The final structure of the proposed blind equalizer is similar to a WL structure.

The rest of the chapter is organized as follows. In Section 8.2, the analytical WL complex-valued models shown in Chapter 7 are applied to investigate IQ-mixing in multicarrier transmitters. Based on this analysis, in Section 8.3, a WL 4×4 MIMO complex-valued adaptive equalizer is proposed to compensate the IQ-mixing in dual polarization (DP) multicarrier systems. Section 8.4 and 8.5 show the experimental setup and the performance results of the proposed algorithm, respectively. The equalizer is experimentally validated for a multicarrier system with four 8 GBd Nyquist dual polarization quadrature phase-shift keying (DP-QPSK) subcarriers. Section 8.6 summarizes the main conclusions.

8.2 IQ-mixing in multicarrier transmitters

Assume that all subcarriers of the multicarrier signal share the same IQ modulator at the transmitter, such that the presence of IQ-mixing will affect the full baseband signal. Consider a system with an even number N_{sc} of subcarriers, for simplicity, uniformly separated in frequency by f_{sc} Hz. The complex baseband envelope of the entire set of subcarriers is given by

$$s(t) = \sum_{k=1}^{N_{sc}} s_k(t) \exp\left[\frac{j\alpha(k)\omega_{sc}t}{2}\right] \tag{8.1}$$

where $s_k(t)$ is the equivalent complex baseband signal corresponding to the individual subcarrier of index k, $\omega_{sc} = 2\pi f_{sc}$ and $\alpha(k) = 2k - 1 - N_{sc}$. The index $k = 1$ refers to the subcarrier in the *left* most position in the spectrum. The conjugate version of $s(t)$ is given by

$$s^*(t) = \sum_{n=1}^{N_{sc}} s_n^*(t) \exp\left[\frac{j\beta(n)\omega_{sc}t}{2}\right] \tag{8.2}$$

where $\beta(n) = -2n + 1 + N_{sc}$. Observe that $n = 1$ corresponds to the conjugate subcarrier in the *right* most position of the spectrum. In the Fourier domain, equations (8.1) and (8.2) can be written as

$$S(\omega) = \sum_{k=1}^{N_{sc}} S_k(\omega) * \delta\left(\omega - \frac{\alpha(k)\omega_{sc}}{2}\right) \tag{8.3}$$

$$S^*(-\omega) = \sum_{n=1}^{N_{sc}} S_n^*(-\omega) * \delta\left(\omega - \frac{\beta(n)\omega_{sc}}{2}\right) \tag{8.4}$$
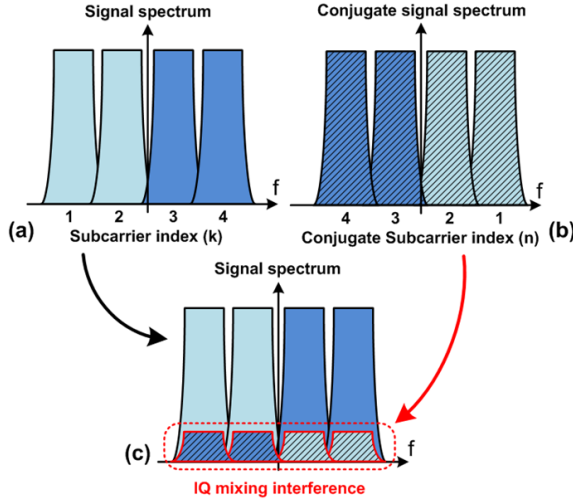
Figure 8.1 Illustration of IQ-mixing interference effect in a multicarrier signal with four subcarriers.

The effect of IQ imbalance can be described by the WL transformation in the complex domain

$$\hat{s}(t) = k_1 s(t) + k_2 s^*(t) \Rightarrow \hat{S}(\omega) = k_1 S(\omega) + k_2 S^*(-\omega) \tag{8.5}$$

where k_1 and k_2 are complex numbers [144], and $S(\omega)$ is the Fourier transform of $s(t)$. Moreover, IQ skew can also be modeled by a WL transformation of $s(t)$, represented in the frequency domain by

$$\hat{S}(\omega) = G_1(\omega)S(\omega) + G_2(\omega)S^*(-\omega) \tag{8.6}$$

where $G_1(\omega) = \cos(\omega\tau/2)$ and $G_2(\omega) = j\sin(\omega\tau/2)$, with τ corresponding to the skew value in seconds.

Therefore, if the multicarrier transmitter suffers from IQ-mixing, the equivalent complex baseband signal $\hat{s}(t)$ will be the result of linear self-interference between $s(t)$ and its conjugate. This implies that each subcarrier $\hat{k}$ will receive linear crosstalk from the *conjugate version* of a subcarrier

$\hat{n}$. The pairs of interfering subcarriers can be determined using Eq. (8.1) and Eq. (8.2), under the condition $\alpha(\hat{k}) = \beta(\hat{n})$. Therefore, interfering subcarriers obey the relation $\hat{k} + \hat{n} = N_{sc} + 1$. For example, for a system with four subcarriers, the interfering pairs are (1, 4) and (2, 3), as illustrated in Fig. 8.1. Another implication of the frequency dependence in Eq. (8.6) is that outer subcarriers will be more affected by the presence of IQ skew than inner subcarriers since the power of the interference is increasing with the frequency, whereas the opposite is happening with the signal power. This difference in performance among subcarriers was observed in [167, 169].

The models shown are valid to describe the IQ-mixing originated *only* at the transmitter or *only* at the receiver front-end in a back-to-back configuration. Here it is assumed that IQ-mixing is present *only* at the transmitter. In this case, the model also holds if the signal is detected after propagation over the fiber channel, because IQ-mixing will not affect the zero-forcing (ZF) equalization of chromatic dispersion (CD) (see Chapter 7). However, if IQ-mixing is induced at the receiver front-end after fiber propagation, the analysis has to include the linear fiber effects, the CD in particular and this case is not investigated here.

8.3 Widely linear 4×4 MIMO complex-valued adaptive equalizer

Based on the analysis presented in Section 8.3, a MIMO WL complex-valued adaptive equalizer structure to compensate the inter-subcarrier IQ-mixing interference induced at DP multicarrier transmitters is proposed. The main idea is to jointly equalize pairs of interfering subcarriers, taking into consideration the conjugate characteristic of the interference by using a WL structure.

The finite impulse response (FIR) structure of the equalizer is given by

$$
\begin{bmatrix} \hat{x}_A \\ \hat{y}_A \end{bmatrix} = \begin{bmatrix} \boldsymbol{h}_{\mathrm{x_A x_A}}^H & \boldsymbol{h}_{\mathrm{x_A y_A}}^H \\ \boldsymbol{h}_{\mathrm{y_A x_A}}^H & \boldsymbol{h}_{\mathrm{y_A y_A}}^H \end{bmatrix} \begin{bmatrix} \boldsymbol{x}_A \\ \boldsymbol{y}_A \end{bmatrix} + \begin{bmatrix} \boldsymbol{h}_{\mathrm{x_A x_B^*}}^H & \boldsymbol{h}_{\mathrm{x_A y_B^*}}^H \\ \boldsymbol{h}_{\mathrm{y_A x_B^*}}^H & \boldsymbol{h}_{\mathrm{y_A y_B^*}}^H \end{bmatrix} \begin{bmatrix} \boldsymbol{x}_B^* \\ \boldsymbol{y}_B^* \end{bmatrix} \tag{8.7}
$$

$$
\begin{bmatrix} \hat{x}_B \\ \hat{y}_B \end{bmatrix} = \begin{bmatrix} \boldsymbol{h}_{\mathrm{x_B x_B}}^H & \boldsymbol{h}_{\mathrm{x_B y_B}}^H \\ \boldsymbol{h}_{\mathrm{y_B x_B}}^H & \boldsymbol{h}_{\mathrm{y_B y_B}}^H \end{bmatrix} \begin{bmatrix} \boldsymbol{x}_B \\ \boldsymbol{y}_B \end{bmatrix} + \begin{bmatrix} \boldsymbol{h}_{\mathrm{x_B x_A^*}}^H & \boldsymbol{h}_{\mathrm{x_B y_A^*}}^H \\ \boldsymbol{h}_{\mathrm{y_B x_A^*}}^H & \boldsymbol{h}_{\mathrm{y_B y_A^*}}^H \end{bmatrix} \begin{bmatrix} \boldsymbol{x}_A^* \\ \boldsymbol{y}_A^* \end{bmatrix}, \tag{8.8}
$$

where $(\boldsymbol{x}, \boldsymbol{y})$ correspond to the signals from distinct polarizations, and the indexes (A, B) indicate any pair of interfering subcarriers defined in Section 8.2. All vectors $\boldsymbol{h}, \boldsymbol{x}_A, \boldsymbol{y}_A, \boldsymbol{x}_B, \boldsymbol{y}_B \in \mathbb{C}^{N \times 1}$, where N is the number of FIR coefficients.

The update algorithm for the filter coefficients is given by Eq. (8.9) and Eq. (8.10), where $(\xi, \psi) = (A, B)$ or $(\xi, \psi) = (B, A)$, $e_{\mathrm{x}_\xi}(k), e_{\mathrm{y}_\xi}(k)$ are the error criteria to be minimized, and μ is the adaptation step.

$$\boldsymbol{h}_{\mathrm{x}_\xi \mathrm{x}_\xi}(k + 1) = \boldsymbol{h}_{\mathrm{x}_\xi \mathrm{x}_\xi}(k) + \mu e_{\mathrm{x}_\xi}(k) \boldsymbol{x}_\xi^*(k)$$
$$\boldsymbol{h}_{\mathrm{x}_\xi \mathrm{y}_\xi}(k + 1) = \boldsymbol{h}_{\mathrm{x}_\xi \mathrm{y}_\xi}(k) + \mu e_{\mathrm{x}_\xi}(k) \boldsymbol{y}_\xi^*(k)$$
$$\boldsymbol{h}_{\mathrm{y}_\xi \mathrm{x}_\xi}(k + 1) = \boldsymbol{h}_{\mathrm{y}_\xi \mathrm{x}_\xi}(k) + \mu e_{\mathrm{y}_\xi}(k) \boldsymbol{x}_\xi^*(k)$$
$$\boldsymbol{h}_{\mathrm{y}_\xi \mathrm{y}_\xi}(k + 1) = \boldsymbol{h}_{\mathrm{y}_\xi \mathrm{y}_\xi}(k) + \mu e_{\mathrm{y}_\xi}(k) \boldsymbol{y}_\xi^*(k) \tag{8.9}$$

$$\boldsymbol{h}_{\mathrm{x}_\xi \mathrm{x}_\psi^*}(k + 1) = \boldsymbol{h}_{\mathrm{x}_\xi \mathrm{x}_\psi^*}(k) + \mu e_{\mathrm{x}_\xi}(k) \boldsymbol{x}_\psi(k)$$
$$\boldsymbol{h}_{\mathrm{x}_\xi \mathrm{y}_\psi^*}(k + 1) = \boldsymbol{h}_{\mathrm{x}_\xi \mathrm{y}_\psi^*}(k) + \mu e_{\mathrm{x}_\xi}(k) \boldsymbol{y}_\psi(k)$$
$$\boldsymbol{h}_{\mathrm{y}_\xi \mathrm{x}_\psi^*}(k + 1) = \boldsymbol{h}_{\mathrm{y}_\xi \mathrm{x}_\psi^*}(k) + \mu e_{\mathrm{y}_\xi}(k) \boldsymbol{x}_\psi(k)$$
$$\boldsymbol{h}_{\mathrm{y}_\xi \mathrm{y}_\psi^*}(k + 1) = \boldsymbol{h}_{\mathrm{y}_\xi \mathrm{y}_\psi^*}(k) + \mu e_{\mathrm{y}_\xi}(k) \boldsymbol{y}_\psi(k). \tag{8.10}$$

The error criteria can be selected according to the type of training intended, as explained in Chapter 7 (7.4.2). For proof of concept with quadrature phase-shift keying (QPSK) subcarriers, blind training is assumed using the constant modulus algorithm (CMA) and a $T/2$-fractionally spaced structure (2 samples/symbol). The experimental validation of the proposed complex-valued equalizer is then reported in the next sections.

8.4   Experimental setup for proof of concept

The experimental setup used to generate and detect the multicarrier signal is depicted in Fig. 8.2 (a). At the transmitter side, an IQ modulator is used to modulate an external cavity laser (ECL). The specified laser linewidth is less than 100 kHz. The baseband signals used to drive the optical IQ modulator are generated by an arbitrary waveform generator (AWG), with a sampling rate of 64 GSa/s and an analog bandwidth of 20 GHz. The baseband signal is composed of four decorrelated QPSK carriers, each modulated at 8 GBd, with root raised cosine (RRC) pulse shape with a roll-off factor of 1%, and separated by 500 MHz guard bands. The binary data of the QPSK subcarriers is generated by decorrelated subsequences of a pseudo-random binary sequence (PRBS) of length $2^{23} - 1$.

The optical signal is amplified and sent to a polarization multiplexing emulation stage, where the final DP-QPSK desired multicarrier signal is obtained. After amplified spontaneous emission (ASE) noise loading, the signal is pre-amplified, filtered, and coherently detected with a single optical
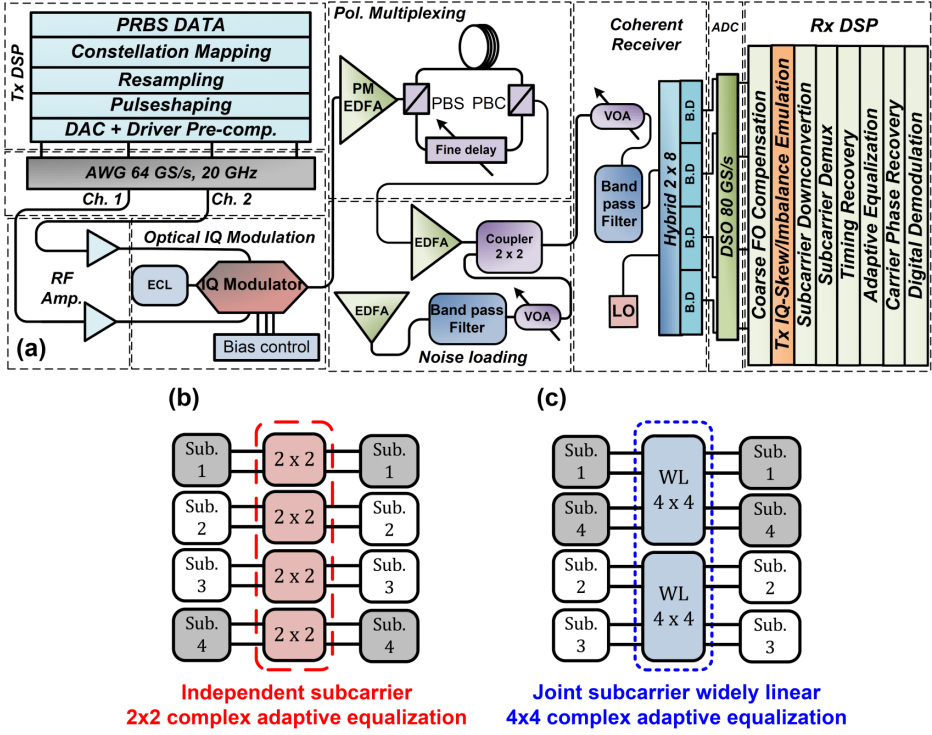
Figure 8.2 (a) Experimental setup to generate and coherently detect a 4×8 Gbaud DP-QPSK Nyquist multicarrier signal and offline DSP applied to the traces. (b) The individual subcarrier equalization scheme using 2×2 MIMO complex-valued adaptive equalizer. (c) The proposed equalization scheme using 4×4 MIMO WL complex-valued adaptive equalizer.

coherent receiver. The detected signal is acquired with a real time digital sampling oscilloscope (DSO) at 80 GSa/s and 33 GHz of analog bandwidth. Offline DSP is used to process the acquired data. The flow of algorithms is composed of coarse frequency offset (FO) compensation, subcarrier demultiplexing (downconversion and matched filtering), timing recovery, adaptive equalization, carrier phase recovery, digital demodulation, and bit error counting.

Due to experimental limitations to configure a broad and precise range of IQ skew and IQ imbalance values at the transmitter side, those effects were emulated offline to the detected data instead. Nevertheless, as the experimental analysis is restricted to the back-to-back case, the proposed model holds. The procedure to add a particular skew value was to shift in

time the IQ components of the acquired polarizations by the corresponding
number of samples. Phase and amplitude IQ imbalance were added to
the signals based on models provided in [144]. In total, the performance
is investigated for of 121 distinct combinations of IQ skew and 441 of IQ
imbalance.

8.5 Results and discussions

In the following experimental results, a performance comparison is carried
out between two equalization strategies for the multicarrier system. The
proposed dual-subcarrier 4×4 MIMO WL complex-valued adaptive equaliza-
tion (Fig. 8.2(c)) is compared against independent subcarrier equalization
with a 2×2 MIMO complex-valued adaptive equalizer (Fig. 8.2(b)).

Both equalizers apply CMA as adaptation rule, and both have FIR
complex-valued filters with 41 coefficients. The Q^2-factor is defined from
the average bit-error rate (BER) of the multicarrier set after complete con-
vergence of the equalizers in the mean square error (MSE). The optical
signal-to-noise ratio (OSNR) (0.1 nm bandwidth) at the receiver input was
fixed in 21 dB, corresponding to an average BER of 2×10^{-4} (Q^2-factor of
≈ 11 dB) for the multicarrier signal in the absence of any IQ-mixing effects.
The BER is calculated over more than 1.2×10^6 bits.

Figures 8.3 and 8.4 show the Q^2-factor surfaces as a function of IQ
amplitude imbalance and IQ phase imbalance, respectively.

For all tested combinations of IQ imbalance, the same performance is
observed after the 4×4 WL complex-valued equalization. On the other
hand, a performance penalty appears for the case where each subcarrier
is individually processed with 2×2 complex-valued equalization. These re-
sults confirm that the interference from the symmetric subcarriers can not
be eliminated by a standard strictly linear equalizer. As expected, the
performance of both equalizers is virtually the same in the absence of IQ
imbalance.

Figure 8.5 shows the Q^2-factor surfaces obtained as a function of the
IQ skew applied to each polarization. In comparison with the IQ imbalance
results, larger performance penalties are induced by IQ skew after 2×2
equalization. These results indicate that the proper calibration of IQ skew
is more critical than IQ imbalance for the performance of the multicarrier
system.

Nevertheless, even for a half-symbol IQ skew, the WL equalizer can
recover the original signals successfully. Again, the performance of both
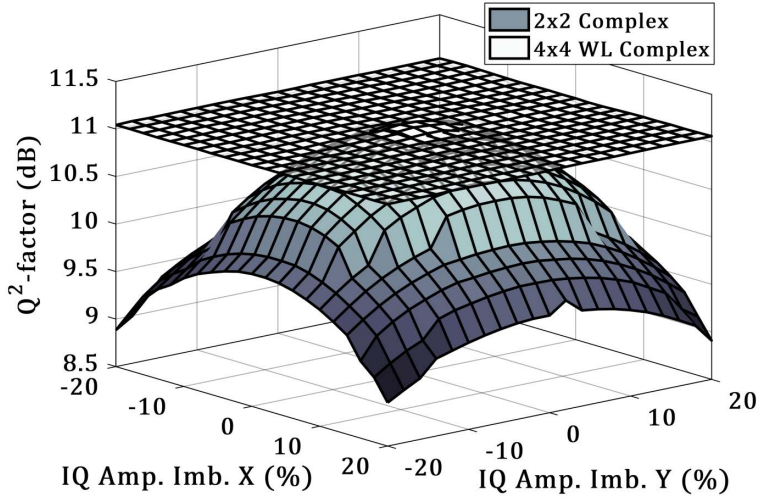
Figure 8.3 Average Q^2-factor of all subcarriers versus the percentage of IQ amplitude imbalance of each polarization.
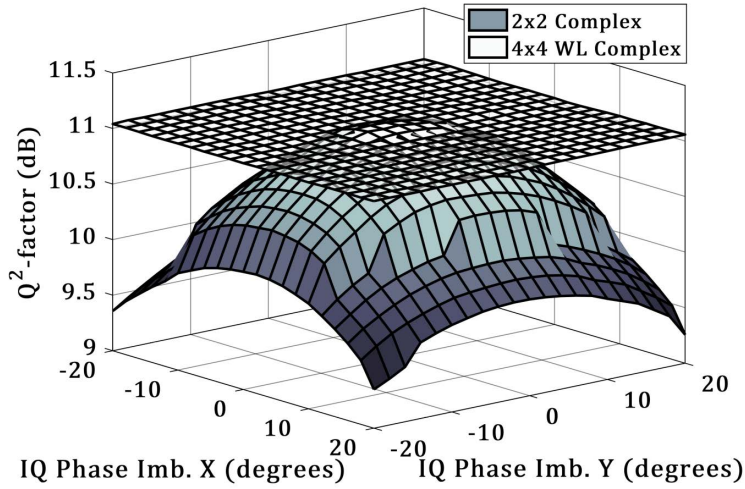
Figure 8.4 Average Q^2-factor of all subcarriers versus IQ phase imbalance in each polarization.

equalizers is virtually the same in the absence of IQ skew.

121
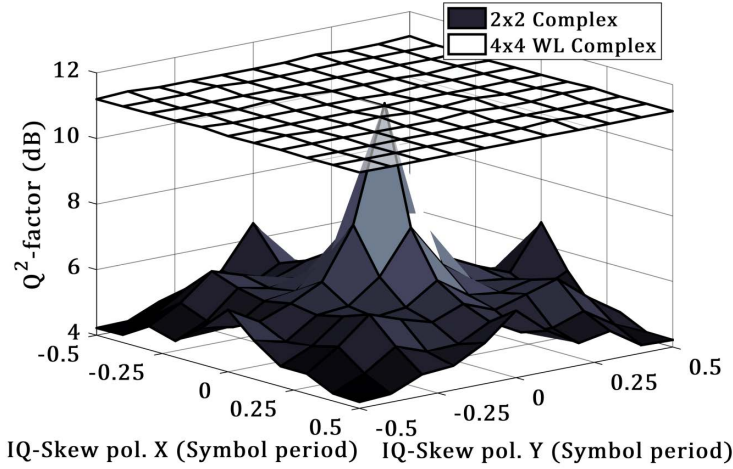
Figure 8.5 Average Q^2-factor of all subcarriers versus IQ skew as a fraction of the symbol period in each polarization.

8.6   Summary

In this chapter, WL complex-valued models were applied to model the IQ imbalance and IQ skew in multicarrier transmitters. It was shown that the presence of these effects translates into inter-subcarrier interference in the multicarrier signal. Such interference will generate performance degradation of the transmission, if not properly managed at the receiver.

To compensate for inter-subcarrier interference, a MIMO 4×4 WL complex-valued adaptive equalizer was proposed based on the analytical models first discussed. The proposed solution was implemented and experimentally validated in 4×8 Gbaud DP-QPSK Nyquist multicarrier system.

The results have shown that IQ-mixing will not be compensated by strictly linear 2×2 independent subcarrier equalization, causing loss of performance. In particular, it was verified that the presence of IQ skew has a significant impact on the BER. However, the proposed WL equalizer was able to compensate the inter-subcarrier interference due to IQ-mixing over a broad range of transmitter IQ imbalance and IQ skew. Finally, the results also validate the usefulness of WL complex-valued models for modeling IQ-mixing effects in multicarrier transmitters.

Chapter 9

Conclusions and outlook

The recent advances in optical communication over single-mode fibers (SMFs) have been driven by the fast development of the coherent transmission systems. In parallel, digital signal processing (DSP) has become one of the most important building blocks in the architecture of coherent optical transceivers.

As the throughput and reliability of optical networks get boosted by the use of advanced modulation and coding schemes, more sophisticated signal processing techniques are required at transmitters and receivers.

This thesis presents novel contributions to the state-of-the-art of DSP techniques for transmission impairment mitigation and compensation in coherent optical systems. In the following, a summary of conclusions and prospects for future work is presented.

Kerr nonlinearity compensation

Chapters 3, 4 and 5 presented studies related to Kerr nonlinearity compensation (NLC), focusing on numerical and experimental performance assessments.

The performance gains from single-carrier digital backpropagation (SC-DBP) and maximum likelihood sequence detection (MLSD) were numerically assessed in Chapter 3, assuming a number of configurations for superchannel transmission in dispersion uncompensated links. Particularly, the analysis was focused on superchannel transmissions subjected to different levels of linear inter-carrier crosstalk.

The results have shown that the combination of both algorithms was able to provide up to 1.0 dB of improvement in Q^2-factor. In the investi-

gated scenarios, it was observed that MLSD was only effective in mitigating linear crosstalk impairments, providing no advantage with respect to NLC.

In Chapter 4, the performance of receiver-side full-field multicarrier digital backpropagation (MC-DBP) was experimentally studied for dual polarization (DP) multicarrier systems with and without frequency locked carriers. Transmission distances up to 4000 km were investigated. It has been verified that the gains obtained with full-field MC-DBP were slightly higher when the backpropagated carriers were locked in frequency. The performance after full-field MC-DBP differed particularly in the nonlinear regime of transmission. Further investigation is required to precisely characterize the sources of such penalties, as well as possible mitigation strategies.

In Chapter 5, the gains from digital backpropagation (DBP) and probabilistic constellation shaping were experimentally investigated for the first time in wavelength-division multiplexing (WDM) systems employing dual polarization 256QAM (DP-256QAM) and dual polarization 1024QAM (DP-1024QAM). Transmission distances up to 1700 km have been studied. The results obtained for a WDM system with five channels have shown that the gains in achievable information rates (AIRs) obtained by each technique add up to the overall performance improvement.

Remarkably, the AIR gains achieved with probabilistic shaping are comparable with the gains from DBP. Since the first technique is likely to have a lower computational complexity than the second, it is a potential candidate for practical implementation in coherent optical transceivers.

The research community is still actively investigating DSP algorithms for NLC. Recently, it has been shown that split the NLC between transmitter and receiver can provide gains in AIR of WDM systems [98]. Therefore, an interesting topic for future investigation consist in analyzing optimal ways to split the NLC complexity between transmitters and receivers, given practical constraints.

Although these methods were not considered in the studies addressed in this thesis, perturbation-based approximated solutions for the nonlinear Schrödinger equation (NLSE) can provide finite memory models for the nonlinear fiber-optic channel in the time domain [170, 171] which can be used for NLC [17]. However, so far, no investigation has been reported evaluating if further performance improvements can be achieved by including such models in probabilistic optimization frameworks, such as constellation shaping methods. Therefore, this is an appealing subject for future work.

Spectral shaping

Due to its importance for the spectral efficiency of WDM systems, spectral shaping methods have been incorporated in coherent optical transceivers. In Chapter 6, the combination of optical and electrical (digital) pulse shaping is proposed to improve the power spectrum density (PSD) confinement of high baud rate optical time-division multiplexing (OTDM) signals based on periodic trains of optical sinc pulses. The impact of optical end electrical pulse shaping on the spectrum of the OTDM signals is investigated analytically. It is shown that the roll-off of the OTDM spectrum is independent of the number of time-division multiplexing (TDM) slots and depends only on the electrical pulse shape of the modulating signals. These results demonstrate that the Nyquist limit of the PSD bandwidth can be approached for an OTDM with an arbitrary number of parallel tributaries.

An experimental study was carried out to verify the feasibility of this strategy to generate high baud rate (> 100 GBd) Nyquist-OTDM signals. In this experiment, the first WDM Nyquist-OTDM signal generation based on the periodic train of sinc pulses was demonstrated. Straight line transmission of five 112.5 GBd Nyquist-OTDM dual polarization quadrature phase-shift keying (DP-QPSK) channels was demonstrated over a dispersion uncompensated link up to 640 km, with full-field coherent detection at the receiver. The results have shown that electrical (digital) pulse shaping improves the spectral confinement of the modulated OTDM signal, enabling a minimum inter-channel crosstalk penalty of 1.5 dB in baud-rate-spaced Nyquist-WDM systems.

Possibilities for future investigation include a study on the limitations imposed by the finite resolution of the digital-to-analog converters (DACs) to the effectiveness of the proposed solution. Another subject of interest is to conduct a performance comparison between Nyquist-OTDM and optical spectrally-sliced transmitters [172,173] in generating high baud rate signals.

Adaptive equalization

In the chapters 7 and 8, augmented complex-valued models were proposed and investigated for the first time, to the best of our knowledge, to design DSP algorithms for coherent optical communications. This approach has been shown to be very effective to model specific in-phase/quadrature (IQ) imbalances in coherent receivers and multicarrier transmitters.

The study presented in these two chapters was separated into two parts. Firstly, widely linear (WL) models were used to explain the limitations of the standard equalization structures in coherent receivers when the detected signals are impaired by IQ-mixing, especially for the zero-forcing (ZF) equalization of chromatic dispersion (CD). Secondly, a similar analysis was applied to project new complex-valued WL equalizers capable of compensating for such impairments. The application of such equalization schemes improve the robustness of the DSP in coherent receivers and has the potential to relax hardware and calibration requirements of the coherent optical transceivers.

In the analysis presented in Chapters 7 and 8, only linear IQ-mixing with flat frequency responses were considered. Future work in this line may include the investigation of the performance of these equalizers in compensating frequency selective IQ-mixing. Moreover, augmented complex-valued nonlinear filtering models for pre-distortion and equalization could be explored to mitigate or compensate nonlinear distortions caused by hardware components, such as radio frequency (RF) amplifiers and DACs.

Augmented complex-valued models and WL signal processing are relatively recent research topics emerged in the DSP community. It is likely that they can be applied in tackling different problems in optical communications. Particularly, WL models are useful for minimum mean square error (MMSE) estimation problems where the noise is not circularly symmetric. It is well known that non-circular Gaussian noise statistics appear in the detected constellation symbols when the transmitted signals are impaired by nonlinear phase noise. Moreover, a number of nonlinear optical signal processing (OSP) techniques are based on operations involving optical signals and their idlers (conjugates). The outcome of such techniques may generate signals with some degree of impropriety or non-circular noise statistics. Therefore, augmented complex-valued DSP may have a potential to model and improve the performance of systems employing nonlinear OSP. Some of these points should be considered for future investigation.

List of acronyms

ADC	analog-to-digital converter
AIR	achievable information rate
ASE	amplified spontaneous emission
AWG	arbitrary waveform generator
AWGN	additive white Gaussian noise
BER	bit-error rate
CD	chromatic dispersion
CLMS	complex-valued least mean square
CMA	constant modulus algorithm
CUT	channel under test
CW	continuous wave
DAC	digital-to-analog converter
DBP	digital backpropagation
DCF	dispersion compensating fiber
DD-LRD	decision directed least radius distance
DGD	differential group delay
DP	dual polarization
DP-QPSK	dual polarization quadrature phase-shift keying

DP-16QAM	dual polarization 16QAM
DP-32QAM	dual polarization 32QAM
DP-64QAM	dual polarization 64QAM
DP-256QAM	dual polarization 256QAM
DP-1024QAM	dual polarization 1024QAM
DSO	digital sampling oscilloscope
DSP	digital signal processing
ECL	external cavity laser
EDC	electronic compensation of chromatic dispersion
EDFA	Erbium-doped fiber amplifier
EGN	enhanced Gaussian noise
ETDM	electrical time-division multiplexing
EVM	error vector magnitude
FEC	forward error correction
FFT	Fast Fourier Transform
FIR	finite impulse response
FO	frequency offset
FSE	fractionally spaced equalizer
FWHM	full-width at half-maximum
FWM	four-wave mixing
GSOP	Gram–Schmidt orthogonalization procedures
GVD	group-velocity dispersion
HD-FEC	hard-decision forward error correction
ICA	independent component analysis

IM/DD	intensity modulated direct detection
IQ	in-phase/quadrature
ISI	intersymbol interference
LMS	least mean square
LO	local oscillator
MC-DBP	multicarrier digital backpropagation
MI	mutual information
MIMO	multiple-input multiple-output
MLSD	maximum likelihood sequence detection
MMA	multimodulus algorithm
MMSE	minimum mean square error
MSE	mean square error
MZM	Mach-Zehnder modulator
NF	noise figure
NFDM	nonlinear frequency-division multiplexing
NFT	nonlinear Fourier transform
NLC	nonlinearity compensation
NLI	nonlinear interference
NLSE	nonlinear Schrödinger equation
NRZ	non-return-to-zero
OFDM	orthogonal frequency-division multiplexing
OPC	optical phase conjugation
OSP	optical signal processing
OSNR	optical signal-to-noise ratio

OTDM	optical time-division multiplexing
PAPR	peak-to-average power ratio
PLL	phase-locked loop
PM	polarization maintaining
PMD	polarization mode dispersion
PRBS	pseudo-random binary sequence
PSD	power spectrum density
QAM	quadrature amplitude modulation
QPSK	quadrature phase-shift keying
RDE	radius directed equalizer
RF	radio frequency
ROADM	reconfigurable optical add-drop multiplexer
RRC	root raised cosine
RC	raised cosine
RZ	return-to-zero
SbS	symbol-by-symbol
SC-DBP	single-carrier digital backpropagation
SDM	spatial-division multiplexing
SE	spectral efficiency
SNR	signal-to-noise ratio
SOP	state of polarization
SMF	single-mode fiber
SPM	self-phase modulation
SSFM	split-step Fourier method

SSMF	standard single-mode fiber
TDM	time-division multiplexing
WDM	wavelength-division multiplexing
WL	widely linear
WL-CLMS	widely linear CLMS
WSS	wavelength selective switch
XPM	cross-phase modulation
ZF	zero-forcing

Bibliography

[1] G. P. Agrawal, *Fiber-optic communication systems,* 4th ed. Wiley, 2010.

[2] A. Ghazisaeidi, I. F. de J. Ruiz, R. Rios-Müller, L. Schmalen, P. Tran, P. Brindel, A. C. Meseguer, Q. Hu, F. Buchali, G. Charlet, J. Renaudier, "65Tb/s transoceanic transmission using probabilistically-shaped PDM-64QAM," *Proc. of the European Conference on Optical Communication (ECOC)*, postdeadline paper, 2016.

[3] A. D. Ellis, N. Mac Suibhne, D. Saad, D. N. Payne, "Communication networks beyond the capacity crunch," *Phil. Trans. R. Soc. A*, vol. 374, no. 2062, paper 20150191, 2016.

[4] R. S. Tucker, "Green optical communications—part I: energy limitations in transport," *IEEE J. Sel. Topics Quantum Electron.*, vol. 17, no. 2, pp. 245-260, 2011.

[5] R. S. Tucker, "Green optical communications—Part II: energy limitations in networks," *IEEE J. Sel. Topics Quantum Electron.*, vol. 17, no. 2, pp. 261-274, 2011.

[6] R. S. Tucker, K. Hinton, "Energy consumption and energy density in optical and electronic signal processing," *IEEE Photon. J.*, vol. 3, no. 5, pp. 821-833, 2011.

[7] P. J. Winzer, R.-J. Essiambre, "Advanced modulation formats for high-capacity optical transport networks," *J. Light. Technol.*, vol. 24, no. 12, pp. 4711–4728, 2006.

[8] G. P. Agrawal, *Nonlinear fiber optics,* Academic press, 2007.

[9] R.-J. Essiambre, G. Kramer, P. J. Winzer, G. J. Foschini, B. Goebel, "Capacity limits of optical fiber networks," *J. Light. Technol.*, vol. 28, no. 4, pp. 662–701, 2010.

[10] G. Bosco, P.Poggiolini, A. Carena, "Analytical results on channel capacity in uncompensated optical links with coherent detection," *Opt. Express*, vol. 19, no. 26, pp. 438–449, 2011.

[11] R. Dar, M. Shtaif, M. Feder, "New bounds on the capacity of the nonlinear fiber-optic channel," *Opt. Lett.*, vol. 39, no. 2, pp. 398–401, 2014.

[12] G. Kramer, M. I. Yousefi, F. R. Kschischang, E. S. Rogers Sr, "Upper bound on the capacity of a cascade of nonlinear and noisy Channels," arXiv:1503.07652v3, 2015.

[13] A. Mecozzi, R. J. Essiambre, "Nonlinear Shannon limit in pseudolinear coherent systems," *J. Light. Technol.*, vol. 30, no. 12, pp. 2011-2024, 2012.

[14] M. Secondini, E. Forestieri, "Scope and limitations of the nonlinear Shannon limit," *J. Light. Technol.*, vol.PP, no.99, pp.1-1, 2016.

[15] T. Hoshida, "Mitigation of nonlinear propagation impairments by digital signal processing," *Proc. of the European Conference on Optical Communication (ECOC)*, 2016.

[16] E. Ip, J. M. Kahn, "Compensation of dispersion and nonlinear impairments using digital backpropagation," *J. Light. Technol.*, vol. 26, no. 20, pp. 3416-3425, 2008.

[17] Z. Tao, L. Dou, W. Yan, L. Li, T. Hoshida, J. C. Rasmussen, "Multiplier-free intrachannel nonlinearity compensating algorithm operating at symbol rate," *J. Light. Technol.*, vol. 29, no. 17, pp. 2570-2576, 2011.

[18] F. P. Guiomar, J. D. Reis, A. L. Teixeira, A. N. Pinto, "Mitigation of intra-channel nonlinearities using a frequency-domain Volterra series equalizer," *Opt. Express*, vol. 20, no. 2, pp. 1360-1369, 2012.

[19] S. Watanabe, M. Shirasaki, "Exact compensation for both chromatic dispersion and Kerr effect in a transmission fiber using optical phase conjugation," *J. Light. Technol.*, vol. 14, no. 3, pp. 243-248, 1996.

[20] I. Sackey, F. Da Ros, J. K. Fischer, T. Richter M. Jazayerifar, C. Peucheret, K. Petermann, C. Schubert, "Kerr nonlinearity mitigation: mid-link spectral inversion versus digital backpropagation in 5×28-GBd PDM 16-QAM signal transmission," *J. Light. Technol.*, vol 33, no. 9, pp. 1821-1827, 2015.

[21] A. D. Ellis, M. Tan, M. A. Iqbal, M. A. Z. Al-Khateeb, V. Gordienko, G. S. Mondaca, S. Fabbri, M. F. C. Stephens, M. E. McCarthy, A. Perentos, I. D. Phillips, D.Lavery, G. Liga, R. Maher, P. Harper, N. Doran, S. K. Turitsyn, S. Sygletos, P. Bayvel, "4 Tb/s transmission reach enhancement using 10×400 Gb/s super-channels and polarization insensitive dual band optical phase conjugation," *J. Light. Technol.*, vol. 34, no. 8, pp. 1717-1723, 2016.

[22] T. Umeki, T. Kazama, A. Sano, K. Shibahara, K. Suzuki, M. Abe, H. Takenouchi, Y. Miyamoto, "Simultaneous nonlinearity mitigation in 92×180-Gbit/s PDM-16QAM transmission over 3840 km using PPLN-based guard-band-less optical phase conjugation," *Opt. Express*, vol. 24, no. 15, pp. 16945-16951, 2016.

[23] X. Liu, A. R. Chraplyvy, P. J. Winzer, R. W. Tkach, S. Chandrasekhar, "Phase-conjugated twin waves for communication beyond the Kerr nonlinearity limit," *Nat. Photonics*, vol. 7, pp. 560-568, 2013.

[24] X. Liu, "Twin-wave-based optical transmission with enhanced linear and nonlinear performances," *J. Light. Technol.*, vol. 33, no. 5, pp. 1037-1043, 2015.

[25] S. L. I. Olsson, B. Corcoran, C. Lundström, T. A. Eriksson, M. Karlsson, P. A. Andrekson, "Phase–sensitive amplified transmission links for improved sensitivity and nonlinearity tolerance," *J. Light. Technol.*, vol. 33, no. 3, pp. 710-721, 2015.

[26] M. I. Yousefi, "Information transmission using the nonlinear Fourier transform," Ph.D. thesis, University of Toronto, 2013.

[27] J. E. Prilepsky, S. A. Derevyanko, K. J. Blow, I. Gabitov, S. K. Turitsyn, "Nonlinear inverse synthesis and eigenvalue division multiplexing in optical fiber channels," *Phys. Rev. Lett.* , vol. 113, no. 1, paper 013901, 2014.

[28] S. Hari, M. I. Yousefi, F. R. Kschischang, "Multieigenvalue communication," *J. Light. Technol.*, vol. 34, no. 13, pp. 3110-3117, 2016.

[29] P. J. Winzer, "Energy-efficient optical transport capacity scaling through spatial multiplexing," *IEEE Photon. Technol. Lett.*, vol. 23, no. 13, pp. 851-853, 2011.

[30] D. J. Richardson, J. M. Fini, L. E. Nelson, "Space-division multiplexing in optical fibres," *Nat. Photonics*, vol. 7, no. 5, pp. 354-362, 2013.

[31] K. Igarashi, T. Tsuritani, I. Morita, M. Suzuki, "Ultra-long-haul high-capacity super-Nyquist-WDM transmission experiment using multi-core fibers," *J. Light. Technol.*, vol. 33, no. 5, pp. 1027-1036, 2015.

[32] T. Mizuno, H. Takara, A. Sano, Y. Miyamoto, "Dense space-division multiplexed transmission systems using multi-core and multi-mode fiber," *J. Light. Technol.*, vol. 34, no. 2, pp. 582-592, 2016.

[33] T. Mizuno, H. Takara, K. Shibahara, A. Sano, Y. Miyamoto, "Dense space division multiplexed transmission over multicore and multi-mode fiber for long-haul transport systems," *J. Light. Technol.*, vol. 34, no. 6, pp. 1484-1493, 2016.

[34] B. J. Puttnam, R. S. Luís, W. Klaus, J. Sakaguchi, J.-M. D. Mendinueta, Y. Awaji, N. Wada, Y. Tamura, T. Hayashi, M. Hirano, J. Marciante, "2.15 Pb/s transmission using a 22 core homogeneous single-mode multi-core fiber and wideband optical comb," *Proc. of the European Conference on Optical Communication (ECOC)*, post-deadline paper no. 12, 2015.

[35] J. G. Proakis, *Digital communications,* 4th ed., McGraw-Hill, 2000.

[36] M. Seimetz, *High-order modulation for optical fiber transmission,* Springer, 2009.

[37] C. Headley, G. P. Agrawal, *Raman amplification in fiber optical communication systems,* Academic press, 2005.

[38] S. V. Manakov, "On the theory of two-dimensional stationary self-focusing of electromagnetic waves," *Zhurnal Eksperimentalnoi i Teoreticheskoi Fiziki*, vol. 65, pp. 505-516, 1973.

[39] P. K. A. Wai, C. R. Menyuk, H. H. Chen, "Stability of solitons in randomly varying birefringent fibers," *Opt. Lett.*, vol. 16, no. 16, pp. 1231-1233, 1991.

[40] D. Marcuse, C. R. Menyuk, P. K. A. Wai, "Application of the Manakov-PMD equation to studies of signal propagation in optical fibers with randomly varying birefringence," *J. Light. Technol.*, vol. 15, no. 9, pp. 1735-1746, 1997.

[41] J. Kerr, "A new relation between electricity and light: dielectrified media birefringent," *Phil. Mag.*, vol. 50, no. 19, p. 3337, 1875.

[42] P. Poggiolini, G. Bosco, A. Carena, "The GN-model of fiber non-Linear propagation and its applications," *J. Light. Technol.*, vol. 32, no. 4, pp. 694-721, 2014.

[43] R. Dar, M. Feder, A. Mecozzi, M. Shtaif, "Properties of nonlinear noise in long, dispersion-uncompensated fiber links," *Opt. Express*, vol. 21, no. 22, pp. 25685-25699, 2013.

[44] F. Derr, "Coherent optical QPSK intradyne system: concept and digital receiver realization," *J. Light. Technol.*, vol. 10, no. 9, pp. 1290-1296, 1992.

[45] F. M. Gardner, "A BPSK/QPSK timing error detector for sampled receiver," *IEEE Trans. Commun.*, vol. 34, pp.423-429, 1986.

[46] T. Pfau, S. Hoffmann, R. Noé, "Hardware-efficient coherent digital receiver concept with feedforward carrier recovery for M-QAM constellations," *J. Light. Technol.*, vol. 27, no. 8, pp. 989–999, 2009.

[47] O. V. Sinkin, R. Holzlohner, J. Zweck, C. R. Menyuk, "Optimization of the split-step fourier method in modeling optical-fiber communications systems," *J. Light. Technol.*, vol. 21, no. 1, pp. 61–68, 2003.

[48] Q. Zhang, M. I. Hayee, "Symmetrized split-step Fourier scheme to control global simulation accuracy in fiber-optic communication systems," *J. Light. Technol.*, vol. 26, no. 2, pp. 302–316, 2008.

[49] M. G. Taylor, "Phase estimation methods for optical coherent detection using digital signal processing," *J. Light. Technol.*, vol. 27, no. 7, pp. 901-914, 2009.

[50] D. Zibar, L. Carvalho, M. Piels, A. Doberstein, J. Diniz, B. Nebendahl, C. Franciscangelis, J. M. Estaran, H. Haisch, N. G. Gonzalez, J. R. F. de Oliveira, I. T. Monroy, "Bayesian filtering for phase noise characterization and carrier synchronization of up to 192 Gb/s PDM

64-QAM," *Proc. of the European Conference on Optical Communication (ECOC)*, paper Tu.1.3.1, 2014.

[51] M. P. Yankov, T. Fehenberger, L. Barletta, N. Hanik, "Low-complexity tracking of laser and nonlinear phase noise in WDM optical fiber systems," *J. Light. Technol.*, vol. 33, no. 23, pp. 4975-4984, 2015.

[52] S. Chandrasekhar, X. Liu, "Terabit superchannels for high spectral efficiency transmission," *Proc. of the European Conference on Optical Communication (ECOC)*, paper Tu.3.C.5, 2010.

[53] G. Bosco, V. Curri, A. Carena, P. Poggiolini, F. Forghieri, "On the performance of Nyquist-WDM terabit superchannels based on PM-BPSK, PM-QPSK, PM-8QAM or PM-16QAM subcarriers," *J. Light. Technol.*, vol 29, no. 1, pp. 53-61, 2011.

[54] S. Chandrasekhar, X. Liu, "OFDM based superchannel transmission technology," *J. Light. Technol.*, vol. 30, no. 24, pp. 3816-3823, 2012.

[55] O. Gerstel, M. Jinno, A. Lord, S. J. B. Yoo, "Elastic optical networking: a new dawn for the optical layer?," *IEEE Commun. Mag.*, vol. 50, no. 2, pp. s12-s20, 2012.

[56] Y. Huang, E. Ip, P. N. Ji, Y. Shao, T. Wang, Y. Aono, Y. Yano, T. Tajima, "Terabit/s optical superchannel with flexible modulation format for dynamic distance/route transmission," *Proc. of the Optical Fiber Communication Conference (OFC)*, paper OM3H.4, 2012.

[57] E. Riccardi, A. Pagano, M. Bohn, A. Napoli, D. Rafique, N. Sambo, P. Castoldi, M. S. Moreolo, J. M. Fabrega, E. Hugues-Salas, G. Zervas, D. Simeonidou, A. D'Errico, T. Rahman, M. Gunkel, "Sliceable bandwidth variable transponders for elastic optical networks: the idealist vision." *Proc. of the Fotonica AEIT Italian Conference on Photonics Technologies*, 2015.

[58] G. Liga, T. Xu, A. Alvarado, R. I. Killey, P. Bayvel, "On the performance of multichannel digital backpropagation in high-capacity long-haul optical transmission," *Opt. Express*, vol. 22, no. 24, pp. 30053-30062, 2014.

[59] R. Maher, T. Xu, L. Galdino, M. Sato, A. Alvarado, K. Shi, S. J. Savory, B. C. Thomsen, R. I. Killey, P. Bayvel, "Spectrally shaped DP-16QAM super-channel transmission with multi-channel digital back-propagation," *Nat. Sci. Rep.*, vol. 5, p. 8214, 2015.

[60] N. K. Fontaine, X. Liu, S. Chandrasekhar, R. Ryf, S.Randel, P. J. Winzer, R. Delbue, P. Pupalaikis, A. Sureka, "Fiber nonlinearity compensation by digital backpropagation of an entire 1.2-Tb/s superchannel using a full-field spectrally-sliced receiver," *Proc. of the European Conference on Optical Communication (ECOC)*, paper Mo.3.D.5, 2013.

[61] N. Alic, E. Myslivets, E. Temprana, B. P.-P. Kuo, S. Radic, "Nonlinearity cancellation in fiber optic links based on frequency-referenced carriers," *J. Light. Technol. *, vol. 32, no. 15, pp. 2690–2698, 2014.

[62] P. J. Winzer, "High-spectral-efficiency optical modulation formats," *J. Light. Technol.*, vol. 30, no. 24, pp. 3824-3835, 2012.

[63] R. Nagarajan, M. Kato, D. Lambert, P. Evans, S. Corzine, V. Lal, J. Rahn, A. Nilsson, M. Fisher, M. Kuntz, J. Pleumeekers, A. Dentai, H.-S. Tsai, D. Krause, H. Sun, K.-T. Wu, M. Ziari, T. Butrie, M. Reffle, M. Mitchell, F. Kish, D. Welch, "Terabit/s class InP photonic integrated circuits,"*Semicond. Sci. Technol.*, vol. 27, no. 9, p. 94003, 2012.

[64] J. Rahn, S. Kumar, M. Mitchell, H. Sun, K.-T. Wu, G. Goldfarb, M. Kato, D. Krause, R. Nagarajan, F. Kish, D. Welch, "Super-channels: DWDM transmission beyond 100 Gb/s," *Proc. of the IEEE Photonics Conference (IPC)*, pp. 854-855, 2012.

[65] J. Wang, C. Xie, Z. Pan, "Generation of spectrally efficient Nyquist-WDM QPSK signals using digital FIR or FDE filters at transmitters," *J. Light. Technol.*, vol. 30, no. 23, pp. 3679-3686, 2012.

[66] E. P. da Silva, L. Carvalho, C. Franciscangelis, J. Diniz, J. Oliveira, A. Bordonalli, "Spectrally-Efficient 448-Gb/s dual-carrier PDM-16QAM channel in a 75-GHz grid," *Proc. of the Optical Fiber Communication Conference (OFC)*, paper JTh2A.39, 2013.

[67] L. H. H. Carvalho, C. Franciscangelis, G. E. R. Paiva, V. E. Parahyba, A. C. Bordonalli, J. R. F. Oliveira, E. P. da Silva, J. C. R. F.

Oliveira, S. H. Linakis, N. G. Gonzalez, "Transmission of a DAC-Free 1.12-Tb/s superchannel with 6-b/s/Hz over 1000 km with hybrid Raman-EDFA amplification and 10 cascaded 175-GHz flexible ROADMs," *Proc. of the European Conference on Optical Communication (ECOC)*, paper P.4.4, 2013.

[68] L. H. H. Carvalho, C. Floridia, C. Franciscangelis, V. Parahyba, E. P. da Silva, N. G. Gonzalez, J. Oliveira, "WDM transmission of 3x1.12-Tb/s PDM-16QAM superchannels with 6.5-b/s/Hz in a 162.5-GHz flexible-grid using only optical spectral shaping," *Proc. of the Optical Fiber Communication Conference (OFC)*, paper M3C.3, 2014.

[69] D. Marsella, M. Secondini, E. Forestieri, "Maximum likelihood sequence detection for mitigating nonlinear effects," *J. Light. Technol.*, vol. 32, no. 5, pp. 908-916, 2014.

[70] T. Oyama, T. Hoshida, H. Nakashima, C. Ohshima, Z. Tao, J. C. Rasmussen, "Impact of pulse shaping and transceiver electrical bandwidths on nonlinear compensated transmission," *Proc. of the Optical Fiber Communication Conference (OFC)*, paper OTh3C.2, 2013.

[71] E. Ip, J. M. Kahn, "Power spectra of return-to-zero optical signals," *J. Light. Technol.*, vol. 24, no. 3, pp. 1610-1618, 2006.

[72] *Filter bandwidth definition of the WaveShaper S-series programmable optical processor*, white paper, 2012.

[73] R. Borkowski, D. Zibar, I. T. Monroy, "Anatomy of a digital coherent receiver," *IEICE Transactions on Communications*, vol. 97, no. 8, pp. 1528-1536, 2014.

[74] A. Modenini. "Advanced transceivers for spectrally-efficient communications," Ph.D. thesis, University of Parma, 2014.

[75] G. Ungerboeck, "Adaptive maximum likelihood receiver for carrier modulated data-transmission systems," *IEEE Trans. Commun.*, vol. 22, pp. 624–636, 1974.

[76] G. D. Forney, "Lower bounds on error probability in the presence of large intersymbol interference," *IEEE Trans. Commun.*, vol. 20, pp. 76–77, 1972.

[77] M. Shtaif, R. Dar, A. Mecozzi, M. Feder, "Nonlinear interference noise in WDM systems and approaches for its cancellation," *Proc. of the European Conference on Optical Communication (ECOC)*, paper We.1.3.1, 2014.

[78] R. Dar, M. Feder, A. Mecozzi, M. Shtaif, "Inter-channel nonlinear interference noise in WDM systems: modeling and mitigation," *J. Light. Technol.*, vol. 33, no. 5, pp. 1044-1053, 2015.

[79] C. Lin, S. Chandrasekhar, P. J. Winzer, "Experimental study of the limits of digital nonlinearity compensation in DWDM Systems," *Proc. of the Optical Fiber Communication Conference (OFC)*, paper Th4D.4, 2015.

[80] J.-X. Cai, C. R. Davidson, A. Lucero, H. Zhang, D. G. Foursa, O. V. Sinkin, W. W. Patterson, A. N. Pilipetskii, G. Mohs, N. S. Bergano, "20 Tbit/s transmission over 6860 km with sub-Nyquist channel spacing," *J. Light. Technol.*, vol. 30, no. 4, pp. 651-657, 2012.

[81] M. Secondini, T. Foggi, F. Fresi, G. Meloni, F. Cavaliere, G. Colavolpe, E. Forestieri, L. Potí, R. Sabella, G. Prati, "Optical time–frequency packing: principles, design, implementation, and experimental demonstration," *J. Light. Technol.*, vol. 33, no. 17, 3558-3570, 2015.

[82] K. Roberts, Chuandong Li, L. Strawczynski, M. O'Sullivan, I. Hardcastle, "Electronic precompensation of optical nonlinearity," *IEEE Photon. Technol. Lett.*, vol. 18, no. 2, pp. 403-405, 2006.

[83] E. Yamazaki, F. Inuzuka, K. Yonenaga, A. Takada, M. Koga, "Compensation of interchannel crosstalk induced by optical fiber nonlinearity in carrier phase-locked WDM system," *IEEE Photon. Technol. Lett.*, vol. 19, no. 1, pp. 9-11, 2007.

[84] X. Li, X. Chen, G. Goldfarb, E. Mateo, I. Kim, F. Yaman, G. Li, "Electronic post-compensation of WDM transmission impairments using coherent detection and digital signal processing," *Opt. Express*, vol. 16, no. 2, pp. 880-888, 2008.

[85] E. Mateo, L. Zhu, G. Li, "Impact of XPM and FWM on the digital implementation of impairment compensation for WDM transmission using backward propagation," *Opt. Express* 16, 16124-16137, 2008.

[86] E. Yamazaki, F. Inuzuka, K. Yonenaga, A. Takada, Y. Miyamoto, "Digital compensation of intercarrier nonlinear distortion with carrier phase locking," *J. Light. Technol.*, vol. 28, no. 5, pp. 828-836, 2010.

[87] E. Mateo, F. Yaman, G. Li, "Efficient compensation of inter-channel nonlinear effects via digital backward propagation in WDM optical transmission," *Opt. Express*, vol. 18, no. 14, pp. 15144-15154, 2010.

[88] E. Mateo, X. Zhou, G.Li, "Improved digital backward propagation for the compensation of inter-channel nonlinear effects in polarization-multiplexed WDM systems," *Opt. Express*, vol. 19, no. 2, pp. 570-583, 2011.

[89] R. Maher, D. Lavery, D. Millar, A. Alvarado, K. Parsons, R. Killey, P. Bayvel, "Reach enhancement of 100% for a DP-64QAM super-channel using MC-DBP," *Proc. of the Optical Fiber Communication Conference (OFC)*, paper Th4D.5., 2015.

[90] L. Galdino, M. Tan, D. Lavery, P. Rosa, R. Maher, I. D. Phillips, J. D. A. Casta ñón, P. Harper, R. I. Killey, B. C. Thomsen, S. Makovejs, P. Bayvel, "Unrepeatered Nyquist PDM-16QAM transmission over 364 km using Raman amplification and multi-channel digital back-propagation," *Opt. Lett.*, vol. 40, no. 13, pp. 3025-3028, 2015.

[91] L. Galdino, M. Tan, A. Alvarado, D. Lavery, P. Rosa, R. Maher, J. D. A. Casta ñón, P. Harper, S. Makovejs, B. C. Thomsen, P. Bayvel, "Amplification schemes and multi-channel DBP for unre-peatered transmission," *J. Light. Technol.*, vol. 34, no. 9, pp. 2221-2227, 2016.

[92] F. P. Guiomar, S. B. Amado, R. M. Ferreira, J. D. Reis, S. M. Rossi, A. Chiuchiarelli, J. R. F. de Oliveira, A. L. Teixeira, A. N. Pinto, "Multicarrier digital backpropagation for 400G optical superchan-nels," *J. Light. Technol.*, vol. 34, no. 8, pp. 1896-1907, 2016.

[93] V. Vgenopoulou, M. S. Erkilinc, R. I. Killey, Y. Jaouen, I. Roudas, I. Tomkos, "Comparison of Multi-channel nonlinear equalization using inverse Volterra series versus digital backpropagation in 400 Gb/s coherent superchannel," *Proc. of the European Conference on Optical Communication (ECOC)*, paper Th.2.P2.SC3.31, 2016.

[94] E. Temprana, E. Myslivets, B. P.-P. Kuo, L. Liu, V. Ataie, N. Alic, S. Radic, "Overcoming Kerr-induced capacity limit in optical fiber transmission," *Science*, vol. 348, no. 6242, pp. 1445–1448, 2015.

[95] E. Temprana, E. Myslivets, L. Liu, V. Ataie, A. Wiberg, B. P. P. Kuo, N. Alic, S. Radic, "Two-fold transmission reach enhancement enabled by transmitter-side digital backpropagation and optical frequency comb-derived information carriers.," *Opt. Express*, vol. 23, no. 16, pp. 20774–83, 2015.

[96] E. Temprana, E. Myslivets, L. Liu, A. Pejkic, V. Ataie, B. P.-P. Kuo, D. Esman, A. Wiberg, N. Alic, S. Radic, "Transmission reach doubling enabled by transmitter-side digital back propagation and frequency referenced carriers," *Proc. of the European Conference on Optical Communication (ECOC)*, paper Th.2.6.5, 2015.

[97] E. Temprana, E. Myslivets, V. Ataie, B.P.-P. Kuo, N. Alic, V. Vusirikala, V. Dangui, S. Radic, "Demonstration of coherent transmission reach tripling by frequency-referenced nonlinearity precompensation in EDFA-only SMF link," *Proc. of the European Conference on Optical Communication (ECOC)*, paper Tu.3.B.4, 2016.

[98] D. Lavery, D. Ives, G. Liga, A. Alvarado, S. J. Savory, P. Bayvel, "The benefit of split nonlinearity compensation for single channel optical fiber communications," *IEEE Photon. Technol. Lett.*, vol. 28, no. 17, pp. 1803-1806, 2016.

[99] L. B. Du, A. J. Lowery, "The validity of 'Odd and Even' channels for testing all-optical OFDM and Nyquist WDM long-haul fiber systems," *Opt. Express*, vol. 20, no. 26, pp. 445–51, 2012.

[100] S. H. Han, J. H. Lee, "An overview of peak-to-average power ratio reduction techniques for multicarrier transmission," *IEEE Wireless Commun.*, vol. 12, no. 2, pp. 56-65, 2005.

[101] T. M. Cover, J. A. Thomas, *Elements of information theory*, 2nd edition, John Wiley and Sons, 2006.

[102] H. G. Batshon, I. B. Djordjevic, "Iterative polar quantization-based modulation to achieve channel capacity in ultrahigh-speed optical communication systems," *IEEE Photon. J.*, vol. 2, no. 4, pp. 593–599, 2010.

[103] I. B. Djordjevic, T. Liu, L. Xu, T. Wang, "Optimum signal constellation design for high-speed optical transmission," *Proc. of the Optical Fiber Communication Conference (OFC)*, paper OW3H.2., 2012.

[104] J. Estaran, D. Zibar, I. T. Monroy, "Capacity-approaching superposition coding for optical fiber links," *J. Light. Technol.*, vol. 32, no. 17, pp. 2960–2972, 2014.

[105] M. P. Yankov, D. Zibar, K. J. Larsen, L. P. B. Christensen, S. Forchhammer, "Constellation shaping for fiber-optic channels with QAM and high spectral efficiency," *IEEE Photon. Technol. Lett.*, vol. 26, no. 23, pp. 2407, 2014.

[106] F. Buchali, G. Bocherer, W. Idler, L. Schmalen, P. Schulte, F. Steiner, "Experimental demonstration of capacity increase and rate-adaptation by probabilistically shaped 64-QAM," *Proc. of the European Conference on Optical Communication (ECOC)*, paper PDP.3.4., 2015.

[107] F. Buchali, F. Steiner, G. Böcherer, L. Schmalen, P. Schulte, W. Idler, "Rate adaptation and reach increase by probabilistically shaped 64-QAM: an experimental demonstration," *J. Light. Technol.*, vol. 34, no. 7, pp. 1599-1609, 2016.

[108] M. P. Yankov, F. Da Ros, E. P. da Silva, S. Forchhammer, K. J. Larsen, L. K. Oxenløwe, M. Galili, D. Zibar, "Constellation shaping for WDM systems using 256QAM/1024QAM with probabilistic optimization," *J. Light. Technol.*, vol. 34, no. 15, pp. 5146-5156, 2016.

[109] T. Fehenberger, G. Böcherer, A. Alvarado, N. Hanik, "LDPC coded modulation with probabilistic shaping for optical fiber systems," *Proc. of the Optical Fiber Communication Conference (OFC)*, Th2A.23., 2015.

[110] T. Fehenberger, A. Alvarado, G. Böcherer, N. Hanik, "On probabilistic shaping of quadrature amplitude modulation for the nonlinear fiber channel," *J. Light. Technol.*, vol. 34, no. 21, pp. 5063-5073, 2016.

[111] R. Dar, M. Feder, A. Mecozzi, M. Shtaif, "On shaping gain in the nonlinear fiber-optic channel," *Proc. of the IEEE International Symposium on Information Theory (ISIT)*, pp. 2794-2798, 2014.

[112] M. P. Yankov, S. Forchhammer, "Temporal probabilistic constellation shaping for WDM optical communication systems," *Proc. of the European Conference on Optical Communication (ECOC)*, paper W.1.C.5, 2016.

[113] A. Leven, F. Vacondio, L. Schmalen, S. Brink, W. Idler, "Estimation of soft FEC performance in optical transmission experiments," *IEEE Photon. Technol. Lett.*, vol. 23, no. 20, pp. 1547-1549, 2011.

[114] A. Alvarado, E. Agrell, D. Lavery, R. Maher, P. Bayvel, "Replacing the soft-decision FEC limit paradigm in the design of optical communication systems," *J. Light. Technol.*, vol. 33, no. 20, pp. 4338-4352, 2015.

[115] T. Eriksson, T. Fehenberger, W. Idler, "Characterization of nonlinear fiber interactions using multidimensional mutual information over time and polarization," *J. Light. Technol.*, vol.PP, no.99, pp.1-1, 2016.

[116] M. P. Yankov, "Capacity estimation and near-capacity achieving techniques for digitally modulated communication systems", *Ph.D thesis, DTU Fotonik*, 2015.

[117] R. Dar, P. J. Winzer, "On the limits of digital back-propagation in fully loaded WDM systems," *IEEE Photon. Technol. Lett.*, vol. 28, no. 11, pp. 1253-1256, 2016.

[118] E. Ip, "Nonlinear compensation using backpropagation for polarization-multiplexed transmission," *J. Light. Technol.*, vol. 28, no. 6, pp. 939-951, 2010.

[119] D. M. Arnold, H. A. Loeliger, P. O. Vontobel, A. Kavcic, W. Zeng, "Simulation-based computation of information rates for channels with memory," *IEEE Trans. Inf. Theory*, vol. 52, no. 8, pp. 3498-3508, 2006.

[120] P. J. Winzer, "Spatial multiplexing in fiber optics: the $10\times$ caling of metro/core capacities," *Bell Syst. Tech. J.*, vol. 19, pp. 22-30, 2014.

[121] G. Raybon, S. Randel, A. Adamiecki, P. J. Winzer, "High symbol rate transmission systems for data rates above 400 Gb/s using ETDM transmitters and receivers," *Proc. of the European Conference on Optical Communication (ECOC)*, paper Tu.3.3.5, 2014.

[122] G. Raybon, J. Cho, A. Adamiecki, P. J. Winzer, A. Konczykowska, F. Jorge, J. Dupuy, M. Riet, B. Duval, K. Kim, S. Randel, D. Pilori, B. Guan, N. K. Fontaine, E. Burrows, "Single Carrier High Symbol Rate Transmitterfor Data Rates up to 1.0 Tb/s," *Proc. of the Optical Fiber Communication Conference (OFC)*, paper Th3A.2, 2016.

[123] X. Chen, S. Chandrasekhar, P. J. Winzer, P. Pupalaikis, I. Ashiq, A. Khanna, A. Steffan, A. Umbach, "180-GBaud Nyquist Shaped Optical QPSK Generation Based on a 240-GSa/s 100-GHz Analog Bandwidth DAC," *Proc. of the Asia Communications and Photonics Conference (ACP)*, paper AS4A.1, 2016.

[124] X. Chen, S. Chandrasekhar, S. Randel, G. Raybon, A. Adamiecki, P. Pupalaikis, P. J. Winzer, "All-electronic Generation of Ultra-high Symbol Rate Signals," *Proc. of the Asia Communications and Photonics Conference (ACP)*, paper AS1C.4, 2016.

[125] T. Richter, M. Nolle, F. Frey, C. Schubert, "Generation and coherent reception of 107-GBd optical Nyquist BPSK, QPSK, and 16QAM," *IEEE Photon. Technol. Lett.*, vol. 26, no. 9, 2014.

[126] D. O. Otuya, K. Kasai, M. Yoshida, T. Hirooka, M. Nakazawa, "Single-channel 1.92 Tbit/s, Pol-Mux-64 QAM coherent Nyquist pulse transmission over 150 km with a spectral efficiency of 7.5 bit/s/Hz," *Opt. Express*, 22(20), 2014.

[127] M. A. Soto, M. Alem, M. A. Shoaie, A. Vedadi, C.-S. Brès, L. Thévenaz, T. Schneider, "Optical sinc-shaped Nyquist pulses of exceptional quality," *Nat. Commun.*, vol. 4, article number: 2898, 2013.

[128] A. J. Lowery, C. Zhu, E. Viterbo, B. Corcoran, "All-optical generation of DFT-S-OFDM superchannels using periodic sinc pulses," *Opt. Express*, vol. 22, no. 22, 2014.

[129] J. Zhang, J. Yu, Y. Fang, N. Chi, "High speed all optical Nyquist signal generation and full-band coherent detection," *Nat. Sci. Rep.*, 4, article number: 6156, 2014.

[130] H.Yamazaki, A. Sano, M. Nagatani, Y. Miyamoto, "Single-carrier 1-Tb/s PDM-16QAM transmission using high-speed InP MUX-DACs and an integrated OTDM modulator," *Opt. Express*, vol. 23, no. 10, pp. 12866-12873, 2015.

[131] R. Rios-Müller, J. Renaudier, P. Brindel, H. Mardoyan, P. Jennevé, L. Schmalen, G. Charlet, "1-Terabit/s net data-rate transceiver based on single-carrier Nyquist-shaped 124 Gbaud PDM-32QAM," *Proc. of the Optical Fiber Communication Conference (OFC)*, paper Th5B.1, 2015.

[132] H. Mardoyan, R. Rios-Müller, M. A. Mestre, P. Jennevé, L. Schmalen, A. Ghazisaeidi, J. Renaudier, "Transmission of single-carrier Nyquist-shaped 1-Tb/s line-rate signal over 3,000 km," *Proc. of the Optical Fiber Communication Conference (OFC)*, paper W3G.2, 2015.

[133] D. Zibar, L. H. H. de Carvalho, M. Piels, A. Doberstein, J. Diniz, B. Nebendahl, C. Franciscangelis, J. Estaran, H. Haisch, N. G. Gonzalez, J.C.R.F. de Oliveira, I. T. Monroy, "Application of machine learning techniques for amplitude and phase noise characterization," *J. Light. Technol.*, vol. 33, no. 7, pp. 1333-1343, 2015.

[134] R. Maher, M. Sato, T. Xu, L. Galdino, S. Kilmurray, S. Savory, B. Thomsen, R. Killey, P. Bayvel, "Digital pulse shaping to mitigate linear crosstalk in Nyquist-spaced 16QAM WDM transmission systems," *Proc. of the The OptoElectronics and Communication Conference and the Australian Conference (OECC/ACOFT)*, 2014.

[135] R. Schmogrow, M. Winter, M. Meyer, D. Hillerkuss, S. Wolf, B. Baeuerle, A. Ludwig, B. Nebendahl, S. Ben-Ezra, J. Meyer, M. Dreschmann, M. Huebner, J. Becker, C. Koos, W. Freude, J. Leuthold, "Real-time Nyquist pulse generation beyond 100 Gbit/s and its relation to OFDM," *Opt. Express*, vol. 20, no. 1, pp. 317-337, 2012.

[136] Recommendation ITU-T G.694.1, *Spectral grids for WDM applications: DWDM frequency grid,* February, 2012.

[137] S. J. Savory, "Digital coherent optical receivers: algorithms and subsystems," *IEEE J. Sel. Topics Quantum Electron.*, vol. 16, no. 5, pp. 1164-1179, 2010.

[138] R. W. Lucky, "Automatic equalization for digital communication," *Bell Syst. Tech. J.*, vol. 44, no. 4, pp. 547-588, 1965.

[139] M. Paskov, D. Lavery, S. J. Savory, "Blind equalization of receiver in-phase/quadrature skew in the presence of Nyquist filtering," *IEEE Photon. Technol. Lett.*, vol. 25, no. 24, pp. 2446-2449, 2013.

[140] M. S. Faruk, K. Kikuchi, "Compensation for in-phase/quadrature imbalance in coherent-receiver front-end for optical quadrature amplitude modulation," *IEEE Photon. J.*, vol. 5, no. 2, pp. 7800110-7800110, 2013.

[141] R. Rios-Müller, J. Renaudier, G. Charlet, "Blind receiver skew compensation for long-haul non-dispersion managed systems," *Proc. of the European Conference on Optical Communication (ECOC)*, paper Th.2.3.1, 2014.

[142] R. Rios-Müller, J. Renaudier, G. Charlet, "Blind receiver skew compensation and estimation for long-haul non-dispersion managed systems using adaptive equalizer," *J. Light. Technol.*, vol. 33, no. 7, pp. 1315–1318, 2015.

[143] M. Karlsson, "Four-dimensional rotations in coherent optical communications," *J. Light. Technol.*, vol. 32, no. 6, pp. 1246-1257, 2014.

[144] P. Rykaczewski, M. Valkama, M. Renfors, "On the connection of I/Q imbalance and channel equalization in direct-conversion transceivers," *IEEE Trans. Veh. Technol.*, vol. 57, no. 3, pp. 1630-1636, 2008.

[145] T. Adali, P. J. Schreier, L. L. Scharf, "Complex-valued signal processing: the proper way to deal with impropriety," *IEEE Trans. Signal Process.*, vol. 59, no. 11, pp. 5101-5125, 2011.

[146] D. Mattera, L. Paura, F. Sterle, "Widely linear MMSE equalizer for MIMO linear time-dispersive channel," *Proc. of the 3rd International Symposium on Image and Signal Processing and Analysis*, 2003 .

[147] D. Darsena, G. Gelli, L. Paura, F. Verde, "Widely linear equalization and blind channel identification for interference-contaminated multicarrier systems," *IEEE Trans. Signal Process.*, vol. 53, no. 3, pp. 1163-1177, 2005.

[148] D. Mattera, L. Paura, F. Sterle, "Widely linear decision-feedback equalizer for time-dispersive linear MIMO channels," *IEEE Trans. Signal Process.*, vol. 53, no. 7, pp. 2525-2536, 2005.

[149] B. S. Chang, C. Rocha, D. Ruyet, D. Roviras, "Widely linear MMSE precoding and equalization techniques for SC-FDE systems,"*EURASIP Journal on Advances in Signal Processing*, 2014.

[150] D. P. Mandic, V. S. L. Goh, "Complex valued nonlinear adaptive filters: noncircularity, widely linear and neural models," Wiley Publishing, 2009.

[151] S. Javidi, M. Pedzisz, V. S. L. Goh, D. P. Mandic, "The augmented complex least mean square algorithm with application to adaptive prediction problems," *Proc. 1st IARP Workshop on Cognitive Information Processing,* 2008.

[152] X. Xu, B. Châtelain, D. V. Plant, "Decision directed least radius distance algorithm for blind equalization in a dual-polarization 16-QAM system," *Proc. of the Optical Fiber Communication Conference (OFC)*, paper OM2H.5, 2012.

[153] E. Ip, J. M. Kahn, "Digital equalization of chromatic dispersion and polarization mode dispersion," *J. Light. Technol.*, vol. 25, no. 8, pp. 2033-2043, 2007.

[154] J. Armstrong, "OFDM for optical communications," *J. Light. Technol.*, vol. 27, no. 3, pp. 189-204, 2009.

[155] G. Bosco, A. Carena, V. Curri, P. Poggiolini, F. Forghieri, "Performance limits of Nyquist-WDM and CO-OFDM in high-speed PM-QPSK systems," *IEEE Photon. Technol. Lett.*, vol. 22, no. 15, pp. 1129-1131, 2010.

[156] K. Igarashi, T. Tsuritani, I. Morita, Y. Tsuchida, K. Maeda, M. Tadakuma, T. Saito, K. Watanabe, K. Imamura, R. Sugizaki, M. Suzuki, "Super-Nyquist-WDM transmission over 7,326-km seven-core fiber with capacity-distance product of 1.03 Exabit/s.km," *Opt. Express*, vol. 22, no. 2, pp. pp. 1220-1228, 2014.

[157] J. Fickers, A. Ghazisaeidi, M. Salsi, G. Charlet, P. Emplit, F. Horlin, "Multicarrier offset-QAM for long-haul coherent optical communications," *J. Light. Technol.*, vol. 32, no. 24, pp. 4671-4678, 2014.

[158] X. Liu, S. Chandrasekhar, P. J. Winzer, "Digital signal processing techniques enabling multi-Tb/s superchannel transmission: an overview of recent advances in DSP-enabled superchannels," *IEEE Signal Process. Mag.*, vol. 31, no. 2, pp. 16-24, 2014.

[159] M. S. Moreolo, J. M. Fabrega, L. Nadal, F. J. Vilchez, A. Mayoral, R. Vilalta, R. Munoz, R. Casellas, R. Martinez, M. Nishihara, T.

Tanaka, T. Takahara, J. C. Rasmussen, C. Kottke, M. Schlosser, R. Freund, F. Meng, S. Yan, G. Zervas, D. Simeonidou, Y. Yoshida, K.-I. Kitayama, "SDN-enabled sliceable BVT based on multicarrier technology for multiflow rate/distance and grid adaptation," *J. Light. Technol.*, vol. 34, no. 6, pp. 1516-1522, 2016.

[160] A. Carena, G. Bosco, V. Curri, Y. Jiang, P. Poggiolini, F. Forghieri, "EGN model of non-linear fiber propagation," *Opt. Express*, 22, 16335-16362, 2014.

[161] P. Poggiolini, A. Nespola, Y. Jiang, G. Bosco, A. Carena, L. Bertignono, S. M. Bilal, S. Abrate, F. Forghieri, "Analytical and experimental results on system maximum reach increase through symbol rate optimization," *J. Light. Technol.*, vol. 34, no. 8, pp. 1872-1885, 2016.

[162] M.Qiu, Q. Zhuge, M. Chagnon, Y. Gao, X. Xu, M. Morsy-Osman, D. V. Plant, "Digital subcarrier multiplexing for fiber nonlinearity mitigation in coherent optical communication systems," *Opt. Express*, vol. 22, no. 15, pp. 18770-18777, 2014.

[163] A. Nespola *et al.*, "Experimental demonstration of fiber nonlinearity mitigation in a WDM multi-subcarrier coherent optical system," *Proc. of the European Conference on Optical Communication (ECOC)*, paper Mo.3.6.3, 2015.

[164] I. Fatadin, S. J. Savory, D. Ives, "Compensation of quadrature imbalance in an optical QPSK coherent receiver," *IEEE Photon. Technol. Lett.* , vol. 20, no. 20, pp. 1733-1735, 2008.

[165] H. S. Chung, S. H. Chang, K. Kim, "Effect of IQ mismatch compensation in an optical coherent OFDM receiver," *IEEE Photon. Technol. Lett.*, vol. 22, no. 5, pp. 308-310, 2010.

[166] S. Jiang, G. Hu, Z. Li, L. Mu, J. Zhang, "ICA-based compensation for IQ imbalance in OFDM optical fiber communication," *Opt. Commun.*, vol. 310, pp. 80-84, 2014.

[167] G. Bosco, S. M. Bilal, A. Nespola, P. Poggiolini, F. Forghieri, "Impact of the transmitter IQ-skew in multi-subcarrier coherent optical systems," *Proc. of the Optical Fiber Communication Conference (OFC)*, paper W4A.5, 2016.

[168] L. Zhaoxi, H. Guijun, J. Shan, L. Jinghe, W. Yanping, "Multimodulus blind equalization algorithm based compensation for I/Q imbalance in OFDM optical fiber communication," *Optical and Quantum Electronics*, vol. 47, no. 7, pp. 2221-2229, 2015.

[169] B. Baeuerle, A. Josten, R. Bonjour, D. Hillerkuss, J. Leuthold, "Effect of Transmitter Impairments on Nyquist-FDM Signals with Increasing Sub-band Granularity," *Proc. of the Signal Processing in Photonic Communications (SPPCom)*, paper SpW3F.4, 2016.

[170] A. Mecozzi, C.B. Clausen, M. Shtaif, "Analysis of intrachannel nonlinear effects in highly dispersed optical pulse transmission," *IEEE Photon. Technol. Lett.*, vol. 12, no. 4, pp. 392-394, 2000.

[171] Z. Tao, Y. Zhao, Y. Fan, L. Dou, T. Hoshida, J. C. Rasmussen, "Analytical intrachannel nonlinear models to predict the nonlinear noise waveform," *J. Light. Technol.*, vol. 33, no. 10, pp. 2111-2119, 2015.

[172] B. Guan, N. K. Fontaine, R. Ryf, S. Chen, H. Chen, G. Raybon, C. Xie, R. P. Scott, S. J. B. Yoo, "Spectrally-sliced transmitter for long-haul fiber transmission," *Proc. of the Signal Processing in Photonic Communications (SPPCom)*, paper SpTu2F.6, 2016.

[173] B. Guan, N. K. Fontaine, R. Ryf, S. Chen, H. Chen, G. Raybon, C. Xie, R. P. Scott, S. J. B. Yoo, "Optical spectrally sliced transmitter for high fidelity and bandwidth scalable waveform generation," *J. Light. Technol.*, vol. 34, no. 2, pp. 737-744,2016.